IMPACT OF NANO-STRUCTURING ON METAL CARBONATES AND TITANATES

by

MATTHEW THOMAS DAVIDSON

(Under the Direction of Tina T. Salguero)

ABSTRACT

The nanostructuring of reagents can have profound effects on the way chemical reactions proceed and the resulting products. Chapter I focuses on a new synthesis of group II metal carbonates nanoparticles, and describes how these nanoparticles can be used to modify the reaction conditions for subsequent solid state reactions. Additionally chapter I shows how a modification of the synthesis can lead to a never before seen polymorph of $SrCO_3$, accompanied by all relevant characterization to prove its composition and structure. Chapter II looks at how the use of nanosheets, a 2D nanomaterial, can influence reaction conditions and morphologies of the products. Nanosheets of TiO_2 used in hydrothermal, solvothermal and melt-flux reactions to produce $BaTiO_3$ and $PbTiO_3$ nanostructures are described.

INDEX WORDS: nanosheets, nanoparticles, metal carbonates, perovskites, metal oxides,

IMPACT OF NANO-STRUCTURING ON METAL CARBONATES AND TITANATES

by

MATTHEW THOMAS DAVIDSON

B.S., Gettysburg College, 2010

A Dissertation Submitted to the Graduate Faculty of the University of Georgia in Partial Fulfillment of the Requirements for the Degree

DOCTOR OF PHILOSOPHY

ATHENS, GEORGIA

2015

© 2015

Matthew Thomas Davidson

All Rights Reserved

IMPACT OF NANO-STRUCTURING ON METAL CARBONATES AND TITANATES

by

MATTHEW THOMAS DAVIDSON

Major Professor: Tina T. Salguero

Committee: Jason Locklin

John Stickney

Electronic Version Approved:

Suzanne Barbour

Dean of the Graduate School

The University of Georgia

December 2015

DEDICATION

For my loving and supporting family.

ACKNOWLEDGEMENTS

I really need to acknowledge the graduate students at UGA chemistry, both inside and outside the Salguero group. Everyone was always friendly and supportive through the years. Dr. Chris Barrett taught me about how different characterization methods were used for inorganic nanomaterials. Dr. Schroeder and Dr. Shields were very helpful and taught me a lot about the very important characterization techniques. I'd like to thank Dan, Tim, Darrah, Greg, Roshini, Matt, Monika, Mayra, Nick, and Harshani as well as all the undergraduate researchers I worked with over my years in the Salguero lab.

Finally I want to thank Dr. Tina Salguero. Without her lab to work in graduate school would have turned out very differently for me. Her mentorship shaped the kind of scientist I am today.

TABLE OF CONTENTS

CHAPTER 1

GROUP II METAL CARBONATES INTRODUCTION AND LITERATURE REVIEW:

Occurrence:

Alkaline earth metal carbonates (Mg, Ca, Sr and Ba) are found commonly both in biological and geological settings. For example many sea organisms use $MgCO_3$ and $CaCO_3$ to form their shells.[1] This is due to the abundance of both Mg^{+2} and Ca^{+2} in ocean water.[2] Over time the buildup of carbonates from dead sea life leads to the formation of awe-inspiring geologic features like the white cliffs of Dover.[3] With respect to the global "carbon cycle" carbonates play an important role in the capture of CO_2 from the atmosphere and are the byproduct of natural carbon sequestration.[4] The majority of carbon found geologically is locked within carbonates, and within the earth's crust Mg, Ca, Sr and Ba are the 8^{th}, 5^{th}, 14^{th}, and 16^{th} most abundant elements, respectively.[5] The common ores for these metals are carbonates and sulfates.[6] Due to the similarities between the various members of the group II family many of the geologic formations are heterogeneous with alkaline earth metal substitution found in each. For instance calcium has been known to substitute up to 27% into formations of $SrCO_3$.[7]

Synthetically, carbonates usually are made through a precipitation method where a metal salt is reacted with a carbonate salt or simply $CO_{2(g)}$.[8] Group II metal carbonates are very insoluble in water(13 mg/L for $CaCO_3$, 11 mg/L for $SrCO_3$, and 24.2 mg/L for $BaCO_3$) and drop out of solution readily.[9] This is in contrast to other carbonates like Na_2CO_3 or $(NH_4)_2CO_3$, which are very soluble in water.[9]

Significance:

Group II metal carbonates have a wide variety of uses in industrial and biological fields. Industrial applications utilize the physical properties of carbonates in products like paint, rubbers, plastics and more. $CaCO_3$ particles added to high-density polyethylene blends lead to a marked increase in the toughness of samples.[10] Additionally $CaCO_3$ is used to improve the whiteness of bleached paper, as well as increase its water resistance.[11]

As stated earlier $CaCO_3$ is a very important bio-mineral. It comprises many animal shells, bones and teeth. An extensive amount of work has been done to better understand the crystallization of $CaCO_3$ in biological systems. [12] $CaCO_3$ is both biologically compatible and inert, and so it is being examined as a next generation drug delivery material.[13]

Compared to $CaCO_3$, $SrCO_3$ and $BaCO_3$ have generated less research interest. They are not found in large abundance as bio-minerals and Ba^{2+} in particular can be quite toxic to animals.[14] $SrCO_3$'s major industrial use is in the production of fireworks because Sr^{2+} has a strong red emission.[15] $SrCO_3$ is typically found in the earth as the mineral strontianite, with some of the most abundant mines occurring in the USA, Canada and Russia. $BaCO_3$ is typically used as an additive in specialty optical glasses.

Group II metal carbonates are one of the primary components in the synthesis of many complex metal oxide ceramics. $BaCO_3$ is a key material in the production of several important ceramics, such as barium titanate ($BaTiO_3$) and yittrium barium copper oxide ($YBa_2Cu_3O_{7-x}$).[16] It is found in the Earth as the mineral witherite. When heated, carbonates undergo a decomposition that generates CO_2, leaving a highly reactive metal oxide. A common example of this is the solid-state synthesis of $BaTiO_3$.[16c] $BaCO_3$ and TiO_2 are annealed at high temperatures to form $BaTiO_3$ and CO_2 gas. This kind of reaction can be applied to most complex metal oxides that contain Ca,

Sr or Ba.[17] Although this dissertation focuses on group II metal carbonates, it is worth noting that other metal carbonates exhibit similar reactivity such as copper carbonate basic ($Cu_2(OH)_2CO_3$) or lead carbonate ($PbCO_3$).

Crystal structure*:*

Different crystal structures with the same chemical formula are known as polymorphs. Alkaline earth carbonates have three main crystal structures: trigonal ($R\bar{3}c$), orthorhombic (Pmnb) and hexagonal (P6mmc). $CaCO_3$ is the only carbonate found naturally in all three forms; that is, $CaCO_3$ has three polymorphs: trigonal calcite, orthorhombic aragonite, and hexagonal vaterite (Figure 1.1).[8b] There is an additional structure known as amorphous calcium carbonate (ACC), which is defined by lack of crystallinity, and it plays an important role in biogenic $CaCO_3$ chemistry as an intermediate phase.[12] The crystal structures for trigonal and orthorhombic $CaCO_3$ are shown in figure 1.2. Work is still being done to understand the vaterite structure in similar detail.[18] The trigonal structure has planes of Ca^{2+} ions alternating with planes of CO_3^{2-}, with the Ca^{2-} ions directly over the carbons. The spacing between the layers leads to a rather large unit cell in the z direction. In contrast the orthorhombic structure does not have the calcium above the CO_3^{2-}

Figure 1.1: Mineral forms of all three $CaCO_3$ polymorphs

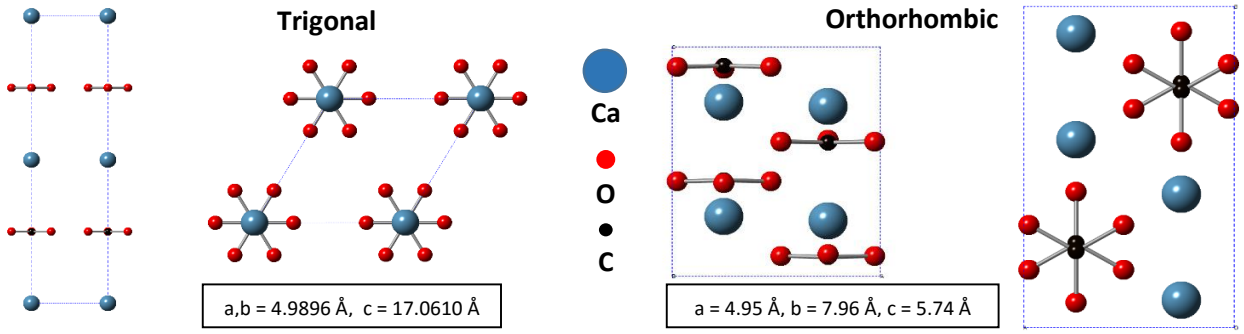

Figure 1.2: Crystal structures of trigonal (calcite) and orthorhombic (aragonite) $CaCO_3$

's and is a more compact unit cell. The smaller alkaline earth metals Mg^{2+} and Ca^{2+} are found most commonly in the trigonal carbonate structure, whereas the larger Sr^{2+} and Ba^{2+} ions are found exclusively in the orthorhombic structure. Figure 1.3 shows a pressure vs crystal phase diagram for $CaCO_3$, $SrCO_3$ and $BaCO_3$.[19] As pressure increases, $CaCO_3$ is forced out of the trigonal and hexagonal structures to an orthorhombic one. This transition at a happens at 2 GPa which is very low pressure from the geologic perspective.[20] The orthorhombic structure is distorted further to another orthorhombic form at 40 GPa.[20] $SrCO_3$ and $BaCO_3$ both start with orthorhombic phases (Pmcn) and transition to post-aragonite (Pmmn) at 7 GPa and 10 GPa respectively where they remain, even with increasing pressure.[21]

Morphology:

Crystal structure has macroscopic implications in the shape of the particles formed. With $CaCO_3$, each of the polymorphs has unique morphologies. Calcite is known for large rhomboids that have the interesting optical birefringence properties shown in figure 1.4. Aragonite usually grows into longer rod shapes. Vaterite is seen typically as either hexagons or spheres

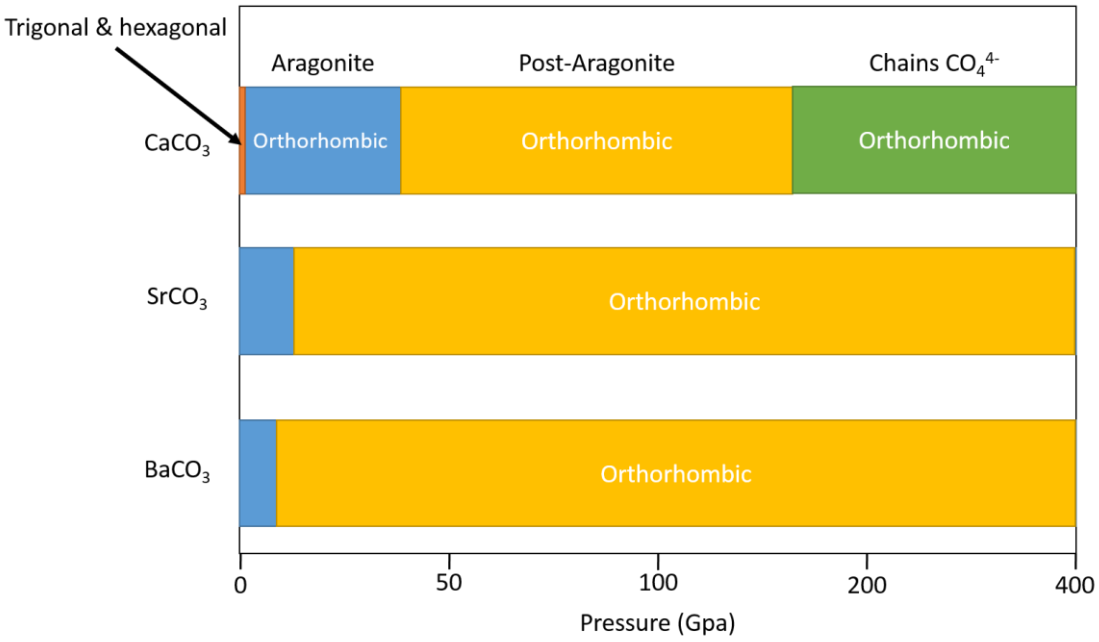

Figure 1.3: A pressure phase diagram showing the different phases of $CaCO_3$, $SrCO_3$ and $BaCO_3$ with respect to pressure.

Nano-structuring:

Recent work on group II carbonates has focused on synthesizing nanomorphologies, specifically nanoparticles. Nanoparticles are particles whose dimensions lie somewhere between 1 and 100 nanometers. Even this definition is not absolute as there are many reports of nanoparticles that have dimensions in the hundreds of nanometers. Nanoparticles have higher surface area to volume than their bulk or microparticle counterparts. This is a useful property when a reaction is surface limited. Many varieties of nanoparticles have been made; metal carbonates, metal oxides, and metallic, to name just a few. Being able to control the size, morphology and polymorphism of nanoparticles is important for tailoring for their end use.

Figure 1.4: Optical birefringence shown in a calcite crystal

With $CaCO_3$, much of the work being done focuses on controlling both the crystal structure and morphology of the nanoparticles. One approach is to use the reaction of $CaCl_2$ and Na_2CO_3 in water/alcohol co-solutions. By using various alcohols in different ratios, one research group was able to produce any of the three polymorphs of $CaCO_3$ in a selective manner.[22] With 10% alcohol the predominant phases were calcite and vaterite. The calcite formed large rhombohedral crystals (>20 μm) while the vaterite formed polycrystalline clusters (>5 μm). If the concentration was increased to 50% the calcite phase is replaced with an aragonite phase. The vaterite polycrystalline clusters start to flatten out into disk like morphologies and the aragonite form polycrystalline needles.[22] Mixtures of water/ethanol with surfactants show similar results in terms of controlling $CaCO_3$ polymorphism. Yan et al. demonstrate that surfactants like sodium dodecyl sulfate form dendritic vaterite morphologies or needles of aragonite. Many groups have used polymers, glycols, surfactants and various other additives to control growth of $CaCO_3$.[8a, 23] For example using a PEG derivative Bastakoti et al was able to create a core micelle structure that $CaCO_3$ crystallized on, forming a core/shell structure and leading to hollow spheres of $CaCO_3$.[23b] This kind of work was extended to the $SrCO_3$ and $BaCO_3$ systems. CTAB/water/cyclohexane/1-pentanol microemulsions were used to produce nanowhiskers, nanorods, polycrystalline spheres and polycrystalline ellipsoids of orthorhombic $SrCO_3$ by varying the concentrations of solvent and surfactant .[24]

The increased surface area of the carbonate nanoparticles is advantageous in the diffusion limited solid state reaction.[16b] Additionally nanoparticles of carbonates are less stable than their bulk counter parts, which leads to a lower decomposition temperature. Combining this with the improved diffusion causes reactions to require less energy input yet still yield homogenous products. Furthermore the reduction in reaction conditions is an important step for the synthesis of ultra-fine or nanopowders of these complex metal oxides via a solid state route.[16b] The high

temperatures and long times tend to lead to a sintering of the particles together into large structures which may not be advantageous for end use.[25]

Research Goals:

A scalable, industrially friendly method for the production of nanoparticles or group II metal carbonates is needed. The work of this dissertation introduces a new synthetic method using methanol as the sole solvent in the production of carbonate nanoparticles. This is done without the need for any surfactants. The nanoparticles made via this method can be used in a myriad of reactions, specifically the production of complex metal oxide ceramics. The new synthetic method is tunable to produce a new polymorph of $SrCO_3$.

1. Milliman, J.; Müller, G.; Förstner, F., *Recent Sedimentary Carbonates: Part 1 Marine Carbonates*. Springer Science & Business Media: 2012.

2. Dickson, A. G.; Goyet, C. *Handbook of methods for the analysis of the various parameters of the carbon dioxide system in sea water. Version 2*; Oak Ridge National Lab., TN (United States): 1994.

3. Leary, P.; Carson, G.; Cooper, M.; Hart, M.; Horne, D.; Jarvis, I.; Rosenfeld, A.; Tocher, B., The biotic response to the late Cenomanian oceanic anoxic event; integrated evidence from Dover, SE England. *Journal of the Geological Society* **1989,** *146* (2), 311-317.

4. Lal, R., Carbon sequestration. *Philosophical Transactions of the Royal Society of London B: Biological Sciences* **2008,** *363* (1492), 815-830.

5. (a) Taylor, S., Abundance of chemical elements in the continental crust: a new table. *Geochimica et cosmochimica acta* **1964,** *28* (8), 1273-1285; (b) McDonough, W. F.; Sun, S.-S., The composition of the Earth. *Chemical geology* **1995,** *120* (3), 223-253.

6. Dana, J. D.; Ford, W. E., *Dana's manual of mineralogy for the student of elementary mineralogy, the mining engineer, the geologist, the prospector, the collector, etc*. J. Wiley & Sons: 1912.

7. Klein, C.; Hurlbut, C. S.; Dana, J. D.; Mineraloge, G., *Manual of mineralogy*. Wiley New York: 1993; Vol. 527.

8. (a) Cölfen, H.; Antonietti, M., Crystal Design of Calcium Carbonate Microparticles Using Double-Hydrophilic Block Copolymers. *Langmuir* **1998,** *14* (3), 582-589; (b) Boyjoo, Y.; Pareek, V. K.; Liu, J., Synthesis of micro and nano-sized calcium carbonate particles and their applications. *Journal of Materials Chemistry A* **2014,** *2* (35), 14270-14288.

9. Lide, D. R., *CRC handbook of chemistry and physics*. CRC press: 2004.

10. Bartczak, Z.; Argon, A.; Cohen, R.; Weinberg, M., Toughness mechanism in semi-crystalline polymer blends: II. High-density polyethylene toughened with calcium carbonate filler particles. *Polymer* **1999,** *40* (9), 2347-2365.

11. Hu, Z.; Zen, X.; Gong, J.; Deng, Y., Water resistance improvement of paper by superhydrophobic modification with microsized $CaCO_3$ and fatty acid coating. *Colloids and Surfaces A: Physicochemical and Engineering Aspects* **2009,** *351* (1–3), 65-70.

12. Faatz, M.; Gröhn, F.; Wegner, G., Amorphous Calcium Carbonate: Synthesis and Potential Intermediate in Biomineralization. *Advanced Materials* **2004,** *16* (12), 996-1000.

13. (a) Wei, J.; Cheang, T.; Tang, B.; Xia, H.; Xing, Z.; Chen, Z.; Fang, Y.; Chen, W.; Xu, A.; Wang, S.; Luo, J., The inhibition of human bladder cancer growth by calcium carbonate/$CaIP_6$ nanocomposite particles delivering AIB1 siRNA. *Biomaterials* **2013,** *34* (4), 1246-1254; (b) Wei, W.; Ma, G.-H.; Hu, G.; Yu, D.; McLeish, T.; Su, Z.-G.; Shen, Z.-Y.,

Preparation of Hierarchical Hollow $CaCO_3$ Particles and the Application as Anticancer Drug Carrier. *Journal of the American Chemical Society* **2008,** *130* (47), 15808-15810.

14. Johnson, C. H.; VanTassell, V. J., Acute barium poisoning with respiratory failure and rhabdomyolysis. *Annals of emergency medicine* **1991,** *20* (10), 1138-1142.

15. Attri, A. K.; Kumar, U.; Jain, V., Microclimate: Formation of ozone by fireworks. *Nature* **2001,** *411* (6841), 1015-1015.

16. (a) Nakamura, M.; Yamada, Y.; Shiohara, Y., Crystal growth of $YBa_2Cu_3O_7$ by the SRL-CP method under low oxygen partial pressure atmosphere. *Journal of materials research* **1994,** *9* (08), 1946-1951; (b) Buscaglia, M. T.; Bassoli, M.; Buscaglia, V.; Alessio, R., Solid-State Synthesis of Ultrafine $BaTiO_3$ Powders from Nanocrystalline $BaCO_3$ and TiO_2. *Journal of the American Ceramic Society* **2005,** *88* (9), 2374-2379; (c) Templeton, L. K.; Pask, J. A., Formation of $BaTiO_3$ from $BaCO_3$ and TiO_2 in Air and in CO_2. *Journal of the American Ceramic Society* **1959,** *42* (5), 212-216.

17. (a) Sinclair, D. C.; Adams, T. B.; Morrison, F. D.; West, A. R., $CaCu_3Ti_4O_{12}$: One-step internal barrier layer capacitor. *Applied Physics Letters* **2002,** *80* (12), 2153-2155; (b) Johnson-McDaniel, D.; Barrett, C. A.; Sharafi, A.; Salguero, T. T., Nanoscience of an Ancient Pigment. *Journal of the American Chemical Society* **2013,** *135* (5), 1677-1679.

18. (a) Wang, J.; Becker, U., Structure and carbonate orientation of vaterite ($CaCO_3$). *American Mineralogist* **2009,** *94* (2-3), 380-386; (b) Pouget, E. M.; Bomans, P. H.; Dey, A.; Frederik, P. M.; de With, G.; Sommerdijk, N. A., The development of morphology and structure in hexagonal vaterite. *Journal of the American Chemical Society* **2010,** *132* (33), 11560-11565.

19. Shatskiy, A. F.; Litasov, K. D.; Palyanov, Y. N., Phase relations in carbonate systems at pressures and temperatures of lithospheric mantle: review of experimental data. *Russian Geology and Geophysics* **2015,** *56* (1–2), 113-142.

20. Ono, S.; Kikegawa, T.; Ohishi, Y.; Tsuchiya, J., Post-aragonite phase transformation in $CaCO_3$ at 40 GPa. *American Mineralogist* **2005,** *90* (4), 667-671.

21. Ono, S.; Shirasaka, M.; Kikegawa, T.; Ohishi, Y., A new high-pressure phase of strontium carbonate. *Phys Chem Minerals* **2005,** *32* (1), 8-12.

22. Sand, K. K.; Rodriguez-Blanco, J. D.; Makovicky, E.; Benning, L. G.; Stipp, S. L. S., Crystallization of $CaCO_3$ in Water–Alcohol Mixtures: Spherulitic Growth, Polymorph Stabilization, and Morphology Change. *Crystal Growth & Design* **2011,** *12* (2), 842-853.

23. (a) Ahmed, J.; Menaka; Ganguli, A. K., Controlled growth of nanocrystalline rods, hexagonal plates and spherical particles of the vaterite form of calcium carbonate. *CrystEngComm* **2009,** *11* (5), 927; (b) Bastakoti, B. P.; Guragain, S.; Yokoyama, Y.; Yusa, S.-i.; Nakashima, K., Synthesis of Hollow $CaCO_3$ Nanospheres Templated by Micelles of Poly(styrene-b-acrylic acid-b-ethylene glycol) in Aqueous Solutions. *Langmuir* **2010,** *27* (1), 379-384; (c) Yan, G.; Wang, L.; Huang, J., The crystallization behavior of calcium carbonate in ethanol/water solution containing mixed nonionic/anionic surfactants. *Powder Technology* **2009,** *192* (1), 58-64; (d) Wei, H.; Shen, Q.; Zhao, Y.; Zhou, Y.; Wang, D.; Xu, D., On the crystallization of calcium carbonate modulated by anionic surfactants. *Journal of Crystal Growth* **2005,** *279* (3–4), 439-446.

24. Cao, M.; Wu, X.; He, X.; Hu, C., Microemulsion-Mediated Solvothermal Synthesis of $SrCO_3$ Nanostructures. *Langmuir* **2005,** *21* (13), 6093-6096.

25. Schmidt, R.; Stennett, M. C.; Hyatt, N. C.; Pokorny, J.; Prado-Gonjal, J.; Li, M.; Sinclair, D. C., Effects of sintering temperature on the internal barrier layer capacitor (IBLC) structure in $CaCu_3Ti_4O_{12}$ (CCTO) ceramics. *Journal of the European Ceramic Society* **2012,** *32* (12), 3313-3323.

CHAPTER 2

SYNTHESIS OF GROUP II METAL CARBONATE NANOPARTICLES

Davidson, Matthew. To be submitted to CrystEngComm

Abstract:

ACO_3 (A = Ca, Sr, and Ba) nanoparticles, were synthesized from the reaction of $ACl_2 \cdot xH_2O$ with $NaHCO_3$. The composition and structure of the ACO_3 products were identified by powder XRD and SAED. Nanoparticle morphology was characterized by TEM. Polycrystalline spherical clusters of vaterite/calcite ($CaCO_3$) nanoparticles, and bowties bundles of polycrystalline strontanite ($SrCO_3$) and witherite ($BaCO_3$) nanoparticles, were synthesized with varying particle sizes from 100 nm to 300 nm. These carbonate nanoparticles were used to synthesize $CaTiO_3$, $SrTiO_3$, and $BaTiO_3$. The nanoparticles led to a marked decrease in the solid state reaction conditions.

Introduction

The group II metal carbonates have a wide variety of uses in biological, scientific, and industrial fields. The most studied carbonate is $CaCO_3$ due to its widespread abundance in nature and commercial applications.[1] Various industries use it as a pigment and filler material in paints, rubbers, and plastics, and it is an important coating material for paper products.[2] More recently, $CaCO_3$ has been used as an encapsulant for anti-cancer drugs because of its biologically-inert nature.[3,4]

Comparatively little work has been done with the other group II carbonates, $SrCO_3$ and $BaCO_3$. Although they are used in the commercial production of certain optical glasses and pyrotecnics, their industrial applications are relatively limited.[5]

All three group II carbonates are used as reagents in the solid-state synthesis of complex metal oxides on both laboratory and industrial scales. These reactions take advantage of the *in situ* decomposition of ACO_3 to the highly reactive metal oxides AO (A= Ca, Sr, Ba). For example, $CaCO_3$ is used to prepare $CaCu_3Ti_4O_{12}$, a material with a colossal dielectric constant.[6] $SrCO_3$ is used to prepare $SrTiO_3$, a possible cathode material for efficient electrolysis of water.[7] $BaCO_3$ is used to prepare $BaTiO_3$, a widely-used dielectric material common to multi-layered ceramic capacitors, and an important ferroelectric material.[8] The mixed oxides $Sr_xBa_{1-x}TiO_3$ also have useful electronic properties.[9] $BaCO_3$ also is used to synthesize $YBa_2Cu_3O_{7-x}$, a high temperature superconductor.[10]

In principle, solid-state reactions involving ACO_3 precursors can be improved by using suitably nanostructured ACO_3. It is well known that nanoparticles have greatly increased surface areas compared to their micro-sized and bulk counterparts, which can lead to improved solid-state

reaction kinetics and reduced reaction times.[11] Additionally, the use of nanostructured precursors can provide some control over product size under these more moderate conditions.[12]

Several synthetic approaches are available to synthesize group II carbonate materials. Solution based precipitation methods use the reaction of Na_2CO_3 and ACl_2 to precipitate ACO_3. Work on $CaCO_3$ has shown that mixed water-alcohol systems can impact size and polymorph distribution of the resulting product.[13] Micro-emulsion, polymer stabilization, and sonochemical reaction conditions are other techniques used to control particle size and morphology.[14] These different methods lead to an impressive array of morphologies and sizes. In particular, $CaCO_3$ nanoparticles <100 nm were synthesized using polymer capping agents.[15] Metal carbonate nanoparticles can be synthesized sonochemically and through flame spray pyrolysis. [16]

In this report, we describe the preparation of nanostructured group II carbonates using a refined synthesis method based on the reaction between group II chlorides and sodium bicarbonate in methanol:

$$ACl_2 \cdot XH_2O + 2NaHCO_3 \longrightarrow ACO_3 + 2NaCl + H_2O + CO_2$$

By using a single solvent for this transformation, several advantages are realized: (1) Mild conditions: the reaction can be carried out at temperatures as low as 60 °C, which could lower large-scale productions costs. (2) Simple preparative setup: the reaction only requires only a sealed vessel and a heat source. Purifying the product can be done with centrifugation alone. It can be scaled to larger quantities with ease. (3) Short reaction times: the reaction is complete in a brief time (<3 h). (4) Particle size control: using both temperature and time as variables, variously sized clusters and particles can be synthesized.

Results and discussion

In this study, reactions of group II metal chlorides with sodium bicarbonate provide the desired metal carbonates in good isolated yields (approximately 60-65%). This chemistry is related to a procedure in the literature that uses Na_2CO_3 instead of $NaHCO_3$.[17,18] Although both reactions provide metal carbonate products, the use of $NaHCO_3$ provides better results with respect to shorter reaction times and enhanced nanoparticle size control. A side-by-side comparison of the effects of Na_2CO_3 versus $NaHCO_3$ under identical conditions can be found in the SI; in brief, the use of Na_2CO_3 resulted in much larger particles, and these reactions required more time to reach completion (Figure S2).

In addition, there are several advantages of using methanol as the solvent. First, the carbonate particles are insoluble in methanol and precipitate readily, making the product easy to isolate. The other main advantage relates to the properties of methanol itself: it is inexpensive, easy to remove from the product by evaporation, and environmentally preferable to other organic solvent.[17] Third, the reaction is spontaneous in water but also yields a much larger product, whereas methanol appears to suppress the reaction until the temperature is raised sufficiently, and providing greater control over size and morphology.

$CaCO_3$ Nanoparticles

The reaction of $CaCl_2 \cdot 2H_2O$ and $NaHCO_3$ went to completion after only 15 min at 90 °C, as indicated by the absence of any remaining $NaHCO_3$. An analysis of the powder XRD pattern of the product (Figure 2.1) shows that it is a mixture of $CaCO_3$ polymorphs: both hexagonal vaterite (JCPDS 00-033-0268) and rhombohedral calcite (JCPDS 01-072-1651) are present in a 1:1 ratio.

Mixed polymorph products are common in the $CaCO_3$ system, and combinations of vaterite and calcite have been reported previously.[19]

The product formed after 4 h of reaction time was identical compared that formed after 15 min, as shown by power XRD (Figure 2.1). Specifically, the relative intensities of vaterite and calcite were unchanged, and the peak widths remained constant. This indicates that the crystallite size and structure are not affected by reaction time.

Scherrer analysis of peak widths in the XRD pattern of the product made at 4 h at 90 °C indicates a crystallite size of 12.5 nm and 24.2 nm for the vaterite and calcite phases respectively. (Table 1 SI). This value is significantly smaller than prior reports of 20-50 nm particle sizes by the H_2O/EtOH precipitation method.[13]

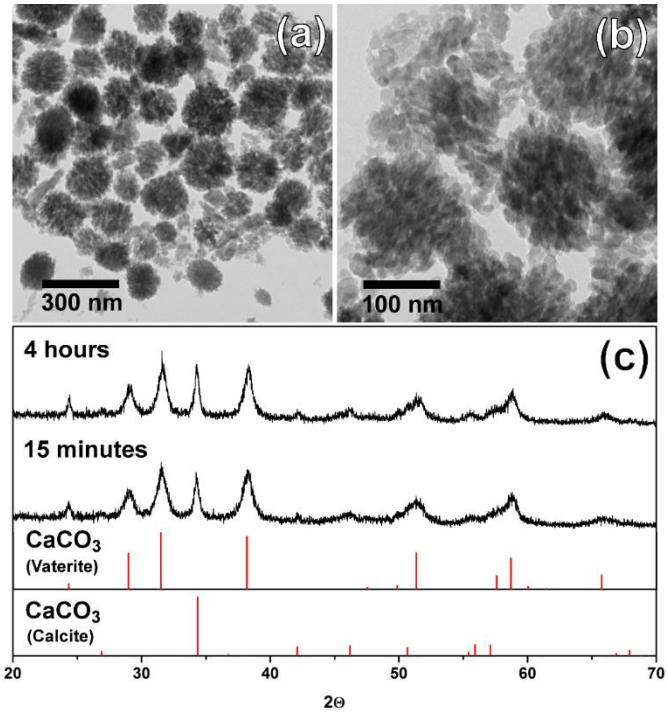

Figure 2.1: TEM images of $CaCO_3$ clusters (a,b) show the cluster size and polycrystalline nature made up of smaller particles of 8-20 nm particles. Powder XRD (c) of 15 min reaction compared to 4 h reaction at 90 °C show no major difference. The pattern matches a mixture of two knowns, calcite and vaterite shown by the drop lines below.

TEM images reveal clusters of nanoparticles (Figure 2.1). The clusters themselves vary in size from 40 to 200 nm in width, and some isolated particles can been seen next to and among them. Higher magnification images of the clusters clearly show that they are aggregates of 8-14 nm particles. The average particle size determined from TEM is 12 nm. These individual nanoparticles lack any recognizable morphology characteristic of the calcite or vaterite phase; rather they are rounded, irregular particles. In contrast, previously synthesized vaterite crystals which show a more pronounced hexagonal structure.[20] The indistinguishable mix of polymorphs is confirmed by SAED of the clusters, which shows rings from both the calcite and vaterite structures (SI).

Although varying the reaction time had no effect, varying temperature impacted on the size of the product $CaCO_3$ particles. The images in Figure 2.3 show how the clusters become a mixture of larger particles and clusters as the reaction temperature is increased from 90 to 120 °C. However, lowering the temperature to 60 °C did not significantly affect the size or morphology of the articles.

$SrCO_3$ Nanoparticles

The reaction of $SrCl_2 \cdot 2H_2O$ and $NaHCO_3$ proceeded to completion after only 15 min at 90 °C, as indicated by the absence of any remaining $NaHCO_3$. Analysis of the powder XRD pattern (Figure 2.2) again shows a mixture of patterns: both orthorhombic strontianite (JCPDS 01-084-1778) and a second set of unknown peaks are present. The unknown pattern does not match $SrCl_2$, $NaHCO_3$ or Na_2CO_3. It is out conclusion that these peaks belong to a second polymorph of $SrCO_3$. To that end we performed an annealing experiment after which the second set of peaks disappeared leaving only the strontianite peaks. Alternatively the unknown polymorph is replaced with strontianite over the course of 1 week at room temperature.

The product formed after 4 h of reaction time was identical compared that formed after 15 min, as shown by power XRD (Figure 2.2). There was a slight increase in the relative intensity of the $SrCO_3$ polymorph compared to strontianite, but the peak widths remained constant. This indicates that the crystallite size and structure are minimally affected by reaction time

Scherrer analysis of the XRD pattern indicates a final crystallite size of 6.7 nm for the 4 h reaction at 90 °C (SI Table 1).

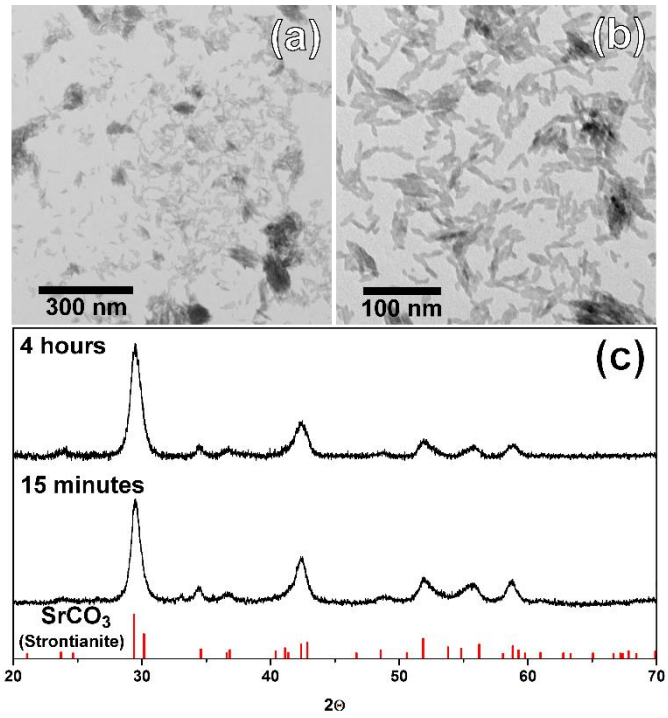

Figure 2.2: TEM images of $SrCO_3$ clusters (a,b) show polycrystalline nature of the sample. The particles are asymmetric 15-20 nm in length and 5 nm in width. Powder XRD (c) of 15 min reaction compared to 4 h reaction at 90 °C show no major difference. The pattern matches strontianite and a second crystal denoted by *. These peaks belong the new meta-stable polymorph of $SrCO_3$.

TEM images of crystal morphology show small clusters of particles that sometimes group into larger clusters. This assembly has been reported before with other orthorhombic structures like aragonite.[13] The individual particles are asymmetric in morphology. They are 10 nm in length and 5 nm in width. The clusters proved to be beam sensitive which could be due to the metastable polymorph. When focused on in TEM the particles within the clusters began to merge. SAED of the particles confirm the XRD with polycrystalline rings associated with strontianite.

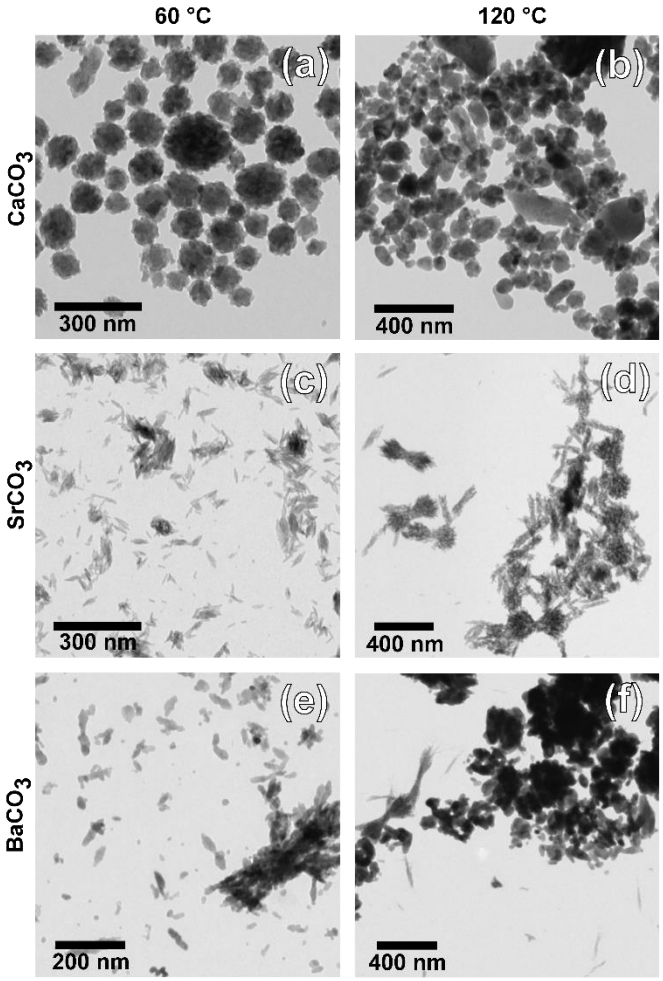

Figure 2.3: TEM images of $CaCO_3$ (a,b) show that higher temperatures sinter the clusters into larger crystals while lower tempatures have little effect. $SrCO_3$ (c,d) at higher temperatures grows into larger clusters and lower temperatures have no effect. $BaCO_3$ (e,f) sinters into large particles at 120 °C and at 60 °C the particles don't form clusters as big as those at 90 °C.

Temperature had a dramatic effect on the morphology of the particles heated at 120 °C. Under these conditions small ellipsoids group into bowtie bundles (Figure 2.3d). These groupings are still comprised of visible smaller particles.

$BaCO_3$ Nanoparticles

The reaction of $BaCl_2 \cdot 2H_2O$ and $NaHCO_3$ went to completion after 2 h at 90 °C, as indicated by the absence of any remaining $NaHCO_3$ (JCPDS 00-015-0700). Thus $BaCO_3$ formation requires a much longer time than either $CaCO_3$ or $SrCO_3$ to proceed to completion. An analysis of the powder XRD pattern of the product (Figure 2.4) shows the orthorhombic witherite (JCPDS 00-005-0378) polymorph of $BaCO_3$. Unlike the other two carbonates, $BaCO_3$ showed increased

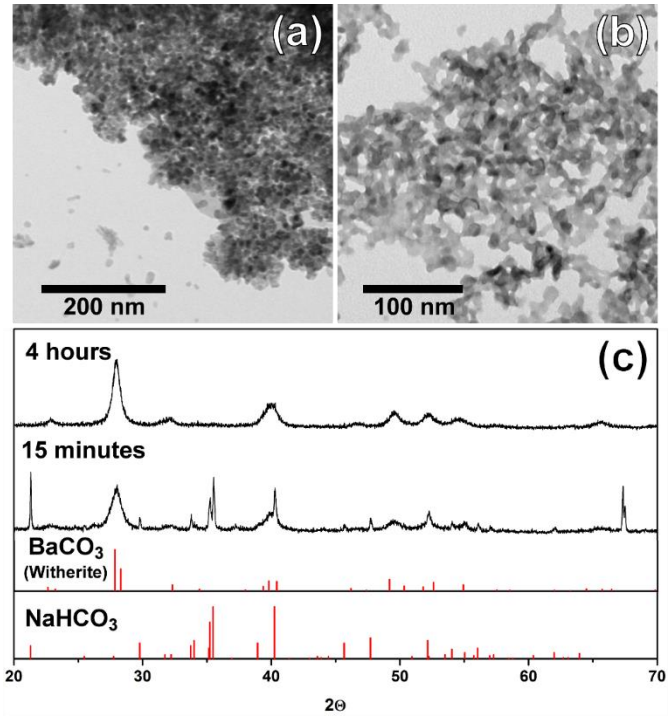

Figure 2.4: TEM images of $BaCO_3$ clusters (a,b) show polycrystalline nature of the sample. Powder XRD (c) of 15 min reaction compared to 4 h reaction at 90 °C show that longer reaction times are required to reach completion. The pattern matches witherite at 4 hours and shows a $NaHCO_3$ impurity at shorter reaction times.

powder XRD intensity with reaction time from 15 m to 4 h. This indicates an increase in crystallinity in the product.

Scherrer analysis of characteristic peak widths in the XRD pattern indicates a final crystallite size of 10.7 nm for 4 h reaction at 90 °C. (SI Table 1)

TEM images show larger clusters made of small particles with irregular morphology. Asymmetric shapes are seen and match those reported previously.[21] The clusters range from 20 nm to up to 1 μm in size but the isolated particles are an average of 10 nm in diameter. SAED of the particles is consistent with the XRD analysis, showing polycrystalline rings d-spacing matched to witherite. (SI)

Temperature impacted both the size and shape of the $BaCO_3$ particles formed during this process. 60 °C and 90 °C produce small rounded particles that aggregate into larger clusters, whereas 120 °C leads to larger particles as well as some ellipsoid bundles (Figure 2.3f)

Incorporation in Solid State Syntheses

To evaluate the effects of our nanoparticles in the synthesis of a wide array of complex metal oxides, the signature solid-state reactions of metal carbonates with titanium dioxide to form ABO_3 perovskites were used as test cases:

$$ACO_3 + TiO_2 \rightarrow ATiO_3 + CO_2$$

In these experiments, the ACO_3 nanoparticles were ground together with bulk anatase (TiO_2, 44 μm) at a 1:1 molar ratio in methanol to form a slurry. This ensures maximum surface area interaction between the carbonate and the anatase. Then thermo-gravimetric analysis (TGA)

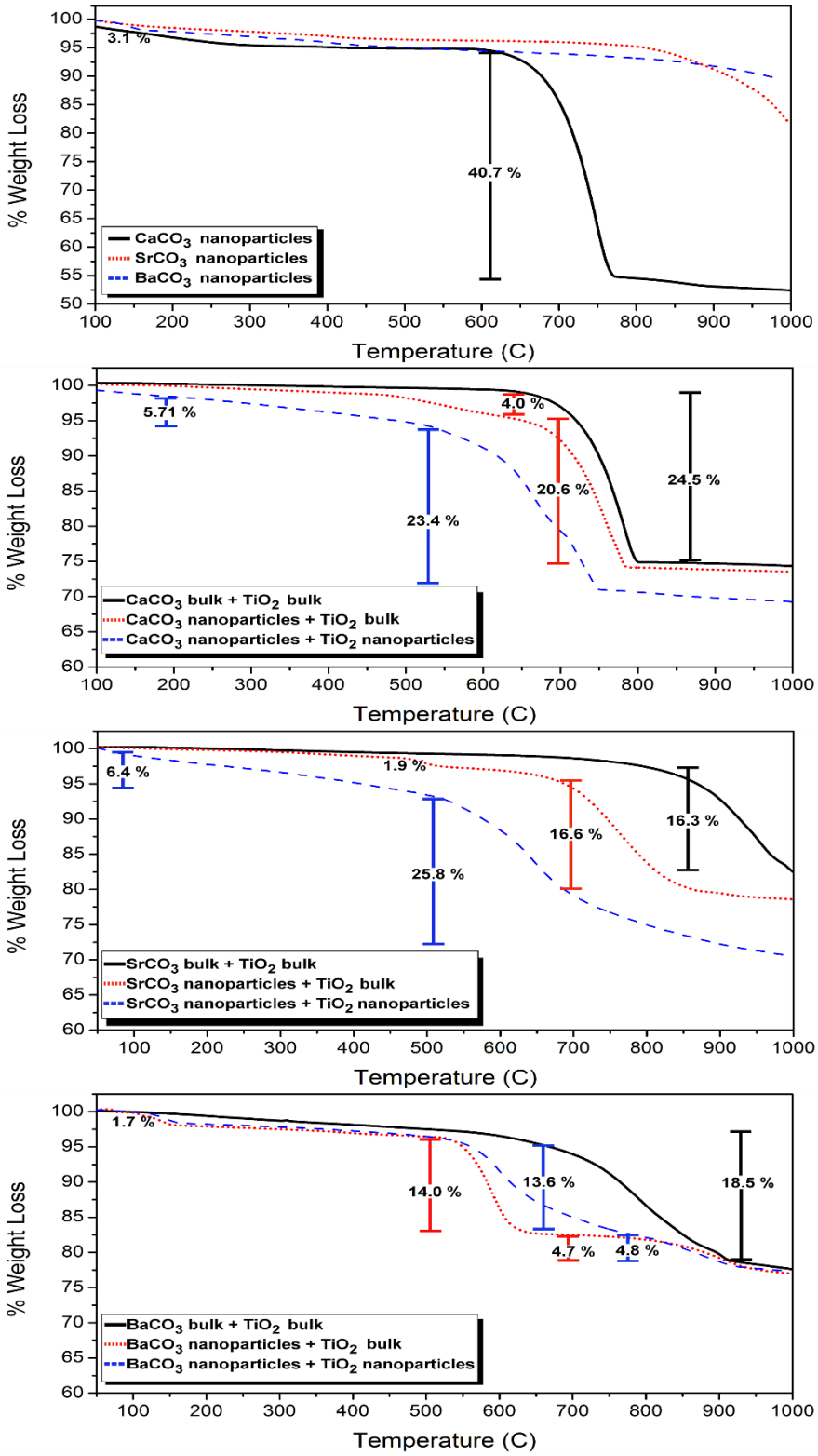

Figure 2.5: TGA analysis of the carbonate decomposition and titanate reactions shows that carbonate nanoparticles lower the temperature of formation for the $ATiO_3$ series. This effect is magnified if both reagents are nanoparticles, except in the case of $BaCO_3$. Mass loss % show at various stages for the different reactions.

data were collected between 30 °C and 1000 °C. These results were compared against bulk carbonate reactions as standards (Figure 2.5).

In all three cases the ACO_3 nanoparticles resulted in reduced onset reaction temperatures when compared to the bulk ACO_3. The onset temperature of the bulk $CaCO_3$ is 750 °C while the nanoparticles lowered the onset to 710 °C. In the $CaTiO_3$ reaction there is a theoretical mass loss of 24% from the loss of a CO_2. Our TGA data shows a mass loss of 24.51% which is a close match. The most significant changes in reaction temperature occur in the $SrCO_3$ and $BaCO_3$ nanoparticles. The bulk $SrCO_3$ has an onset of 846 °C but the nanoparticles of $SrCO_3$ reduce the onset temperature to 695 °C. This is ~150 °C difference in onset temperature. This effect can be increased by using nanoparticles of TiO_2 (<30 nm). The TGA of the all nano reactions show a larger initial decrease most likely due to adsorbed water on the TiO_2. Additionally the nanoparticles reaction of $SrTiO_3$ reached completion during the TGA run. The experimental mass loss of 20.12% matches the expected theoretical mass loss of 19.34%. The onset temperatures for $BaCO_3$ were 697 °C and 553 °C for bulk and nanoparticles respectively. The nanoparticles of $BaCO_3$ showed a dramatic increase in rate indicated by the slope of the weight loss. This continued until a second onset of 828 °C which behaves more like bulk. This possibly indicates a mixture of nanoparticles and larger bulk. Compared to the theoretical mass loss of 15.88%, the Ba reaction showed a larger mass loss of 19.52%.

Conclusions

We developed a simple, one pot synthesis of several group II carbonates. Nanoparticles of $CaCO_3$, $SrCO_3$ and $BaCO_3$ are synthesized from a reaction of the chloride salts and sodium bicarbonate using methanol as a solvent. It proved to be an effective means to make nanoparticles

in a scalable fashion. The nanoparticles formed into clusters of larger size but Scherrer analysis indicated that they were made up of individual particles. Time had little effect on morphology or size but did effect overall reaction completion. Temperature changed the morphology of the $SrCO_3$ above 120 °C and increased the size of the $CaCO_3$ and $BaCO_3$. The nanoparticles were used as a reagent in several solid state reactions and showed a marked decrease in reaction time and formation temperature.

Experimental

Materials

$CaCl_2 \cdot 2H_2O$ (≥99% purity), $SrCl_2 \cdot 6H_2O$ (≥99% purity), and $BaCl_2 \cdot 2H_2O$ (≥99% purity) were purchased from Sigma-Aldrich Corp. and ground freshly before use. $NaHCO_3$ (≥99% purity) from J.T. Baker was used as received. Methanol (99.9%) from Sigma Aldrich was used as received

Preparation of ACO_3 nanoparticles

A 100 mL glass ampoule was charged with 1.20 mmol of $ACl_2 \cdot 2H_2O$, 2.00 mmol of $NaHCO_3$, and 20 mL of methanol. The tube was sealed with a Teflon stopcock and placed in a 60, 90, or 120 °C heating bath with stirring for 15 min, 30 min, 1 h, 2 h, or 4 h. When the reaction was complete, the mixture was centrifuged at 10,000 rpm for 10 min. The supernatant was removed and fresh methanol (20 mL) added to dissolve residual NaCl. The mixture was centrifuged again at 10,000 rpm for 10 min, and the supernatant was discarded again. The solids were dried in a vacuum oven at 50 °C. All products were isolated as white powders ($CaCO_3$ in 62.7% yield; $SrCO_3$ in 64.6% yield; $BaCO_3$ in 59.8% yield, in the 90 °C 4 h reaction).

Characterization

Transmission electron microscopy (TEM) images and selective area electron diffraction (SAED) patterns were collected using a Tecnai 20 electron microscope operated at 200 keV.

Powder X-ray diffraction (XRD) measurements were obtained on a Bruker Advanced D8 diffractometer using Co Kα radiation. Scherrer analysis was run on the most prominent peaks for each sample and then averaged together for particles size (Table S1).

Thermal gravimetric analysis (TGA) was run on a Mettler-Toledo instrument in an alumina crucible without a lid under air. The tests were done from 30 – 1000 °C at a rate of 10 °C per minute.

1. Xu, A. W.; Antonietti, M.; Cölfen, H.; Fang, Y. P., Uniform Hexagonal Plates of Vaterite $CaCO_3$ Mesocrystals Formed by Biomimetic Mineralization. *Advanced Functional Materials* **2006,** *16* (7), 903-908.

2. Hu, Z.; Zen, X.; Gong, J.; Deng, Y., Water resistance improvement of paper by superhydrophobic modification with microsized $CaCO_3$ and fatty acid coating. *Colloids and Surfaces A: Physicochemical and Engineering Aspects* **2009,** *351* (1–3), 65-70.

3. Wei, W.; Ma, G.-H.; Hu, G.; Yu, D.; McLeish, T.; Su, Z.-G.; Shen, Z.-Y., Preparation of Hierarchical Hollow $CaCO_3$ Particles and the Application as Anticancer Drug Carrier. *Journal of the American Chemical Society* **2008,** *130* (47), 15808-15810.

4. Ueno, Y.; Futagawa, H.; Takagi, Y.; Ueno, A.; Mizushima, Y., Drug-incorporating calcium carbonate nanoparticles for a new delivery system. *Journal of Controlled Release* **2005,** *103* (1), 93-98.

5. Gutmann, B.; Chalup, A., Barium Carbonate. *American Ceramic Society Bulletin* **2000,** *79* (8), 63.

6. (a) Sinclair, D. C.; Adams, T. B.; Morrison, F. D.; West, A. R., $CaCu_3Ti_4O_{12}$: One-step internal barrier layer capacitor. *Applied Physics Letters* **2002,** *80* (12), 2153-2155; (b) Adams, T. B.; Sinclair, D. C.; West, A. R., Characterization of grain boundary impedances in fine- and coarse-grained $CaCu_3Ti_4O_{12}$ ceramics. *Phys. Rev. B* **2006,** *73* (9).

7. (a) Mavroides, J. G.; Kafalas, J. A.; Kolesar, D. F., Photoelectrolysis of water in cells with $SrTiO_3$ anodes. *Applied Physics Letters* **1976,** *28* (5), 241-243; (b) Wang, Q.; Hisatomi, T.; Ma, S. S. K.; Li, Y.; Domen, K., Core/Shell Structured La- and Rh-Codoped SrTiO3 as a Hydrogen Evolution Photocatalyst in Z-Scheme Overall Water Splitting under Visible Light Irradiation. *Chem. Mat.* **2014,** *26* (14), 4144-4150.

8. (a) Johnson, C., SOME DIELECTRIC AND ELECTRO-OPTIC PROPERTIES OF $BaTiO_3$ SINGLE CRYSTALS. *Applied Physics Letters* **1965,** *7* (8), 221-223; (b) Danielson, G. C.; Rundle, R. E., STRUCTURE OF FERROELECTRIC $BaTiO_3$. *Physical Review* **1949,** *75* (10), 1630-1630.

9. Rørvik, P. M.; Grande, T.; Einarsrud, M.-A., One-Dimensional Nanostructures of Ferroelectric Perovskites. *Advanced Materials* **2011,** *23* (35), 4007-4034.

10. (a) Bednorz, J. G.; Müller, K. A., Possible highT c superconductivity in the Ba−La−Cu−O system. *Z. Physik B - Condensed Matter* **1986,** *64* (2), 189-193; (b) Lian, Z.; Pingxiang, Z.; Ping, J.; Keguang, W.; Jingrong, W.; Xiaozu, W., The properties of YBCO superconductors prepared by a new approach: the'powder melting process'. *Superconductor Science and Technology* **1990,** *3* (10), 490.

11. (a) Bastús, N. G.; Casals, E.; Ojea, I.; Varon, M.; Puntes, V., *The reactivity of colloidal inorganic nanoparticles*. INTECH Open Access Publisher: 2012; (b) Roduner, E., Size matters: why nanomaterials are different. *Chemical Society Reviews* **2006,** *35* (7), 583-592.

12. Buscaglia, M. T.; Bassoli, M.; Buscaglia, V.; Alessio, R., Solid-State Synthesis of Ultrafine $BaTiO_3$ Powders from Nanocrystalline $BaCO_3$ and TiO_2. *Journal of the American Ceramic Society* **2005,** *88* (9), 2374-2379.

13. Sand, K. K.; Rodriguez-Blanco, J. D.; Makovicky, E.; Benning, L. G.; Stipp, S. L. S., Crystallization of $CaCO_3$ in Water–Alcohol Mixtures: Spherulitic Growth, Polymorph Stabilization, and Morphology Change. *Crystal Growth & Design* **2011,** *12* (2), 842-853.

14. (a) Thongtem, T.; Tipcompor, N.; Phuruangrat, A.; Thongtem, S., Characterization of $SrCO_3$ and $BaCO_3$ nanoparticles synthesized by sonochemical method. *Materials Letters* **2010,** *64* (4), 510-512; (b) Cölfen, H.; Antonietti, M., Crystal Design of Calcium Carbonate Microparticles Using Double-Hydrophilic Block Copolymers. *Langmuir* **1998,** *14* (3), 582-589; (c) Yang, X.; Xu, G.; Chen, Y.; Wang, F.; Mao, H.; Sui, W.; Bai, Y.; Gong, H., $CaCO_3$ crystallization control by poly(ethylene oxide)–poly(propylene oxide)–poly(ethylene oxide) triblock copolymer and O-(hydroxy isopropyl) chitosan. *Journal of Crystal Growth* **2009,** *311* (21), 4558-4569.

15. Bastakoti, B. P.; Guragain, S.; Yokoyama, Y.; Yusa, S.-i.; Nakashima, K., Synthesis of Hollow $CaCO_3$ Nanospheres Templated by Micelles of Poly(styrene-b-acrylic acid-b-ethylene glycol) in Aqueous Solutions. *Langmuir* **2010,** *27* (1), 379-384.

16. (a) Alavi, M. A.; Morsali, A., Syntheses of $BaCO_3$ nanostructures by ultrasonic method. *Ultrasonics sonochemistry* **2008,** *15* (5), 833-8; (b) Huber, M.; Stark, W. J.; Loher, S.;

Maciejewski, M.; Krumeich, F.; Baiker, A., Flame synthesis of calcium carbonate nanoparticles. *Chemical communications* **2005,** (5), 648-650.

17. Capello, C.; Fischer, U.; Hungerbuhler, K., What is a green solvent? A comprehensive framework for the environmental assessment of solvents. *Green Chemistry* **2007,** *9* (9), 927-934.

18. Li, W.; Gao, C., Efficiently Stabilized Spherical Vaterite $CaCO_3$ Crystals by Carbon Nanotubes in Biomimetic Mineralization. *Langmuir* **2007,** *23* (8), 4575-4582.

19. (a) Zhang, Q.; Ren, L.; Sheng, Y.; Ji, Y.; Fu, J., Control of morphologies and polymorphs of $CaCO_3$ via multi-additives system. *Materials Chemistry and Physics* **2010,** *122* (1), 156-163; (b) Zhang, F.; Yang, X.; Tian, F., Calcium carbonate growth in the presence of water soluble cellulose ethers. *Materials Science and Engineering: C* **2009,** *29* (8), 2530-2538.

20. Ahmed, J.; Menaka; Ganguli, A. K., Controlled growth of nanocrystalline rods, hexagonal plates and spherical particles of the vaterite form of calcium carbonate. *CrystEngComm* **2009,** *11* (5), 927.

21. Ma, M.-G.; Zhu, Y.-J.; Cheng, G.-F.; Huang, Y.-H., Fabrication and characterization of $BaCO_3$ nanostructures. *Materials Letters* **2008,** *62* (17–18), 3110-3113.

SUPPORTING INFORMATION

Table 2.S1: Scherrer analysis of ACO_3 nanoparticles.

Sample	FWHM (2Θ)	Miller Indices	Particle Size Calculated (nm)
$CaCO_3$ (Vaterite)	0.78	(1 1 4)	12.5
$CaCO_3$ (Calcite)	0.40	(1 0 4)	24.2
$SrCO_3$ (Strontianite)	1.14	(1 1 1), (0 2 1)	6.7
$BaCO_3$ (Witherite)	0.90	(0 0 2)	10.7

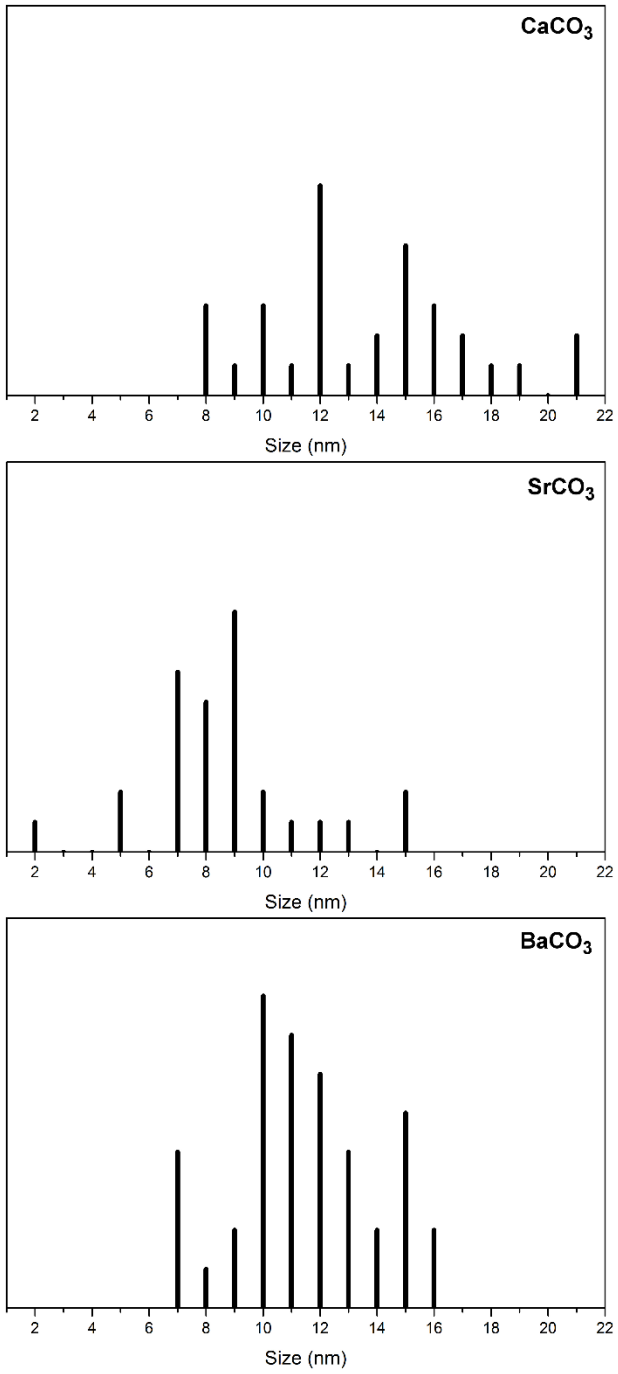

Figure 2.S1: Particle size distributions (n = 40) of ACO_3 nanoparticles analyzed by TEM.

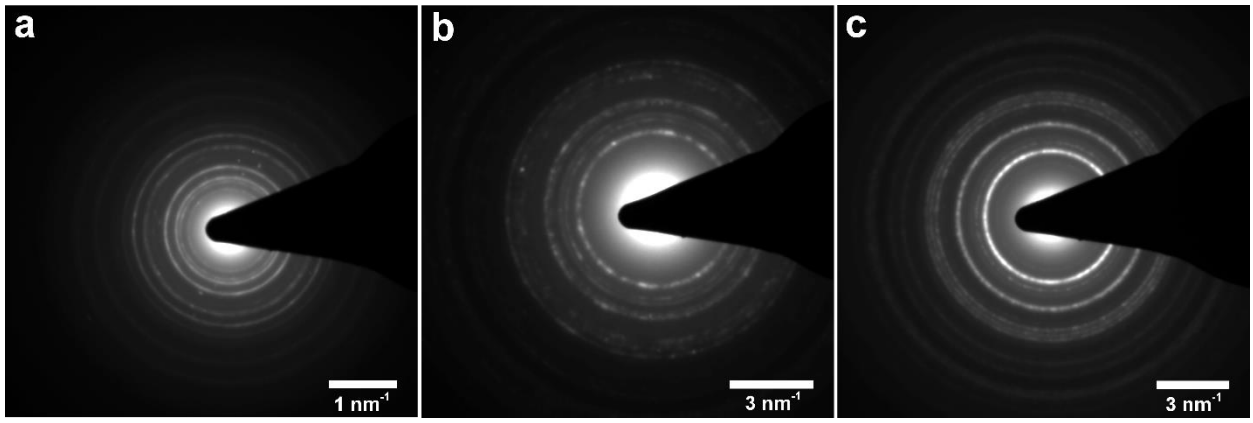

Figure 2.S2: Selected area electron diffraction (SAED) of (a) $CaCO_3$, (b) $SrCO_3$, and (c) $BaCO_3$ nanoparticles.

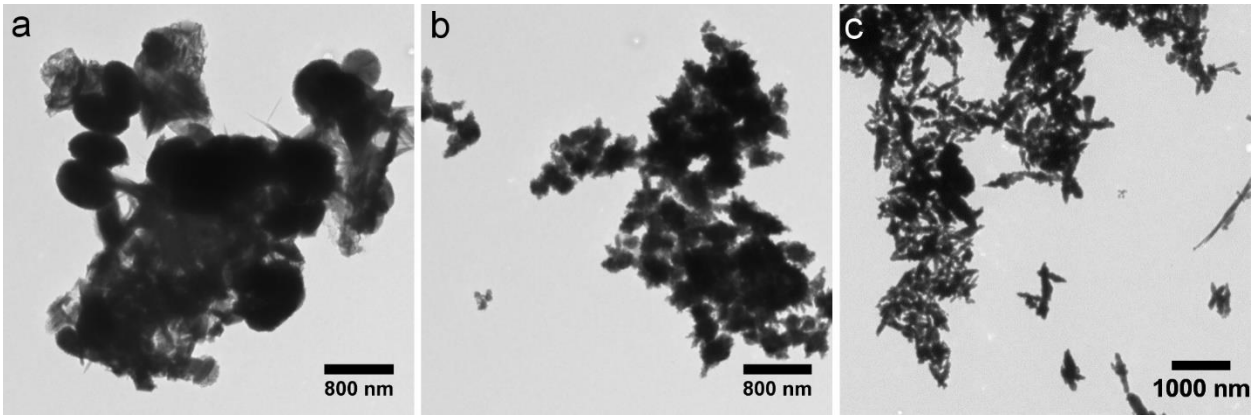

Figure 2.S3: TEM images of products from the reactions of $ACl_2 \cdot XH_2O$ with Na_2CO_3 instead of $NaHCO_3$: (a) $CaCl_2 \cdot 2H_2O$, (b) $SrCl_2 \cdot 6H_2O$, and (c) $BaCl_2 \cdot 2H_2O$.

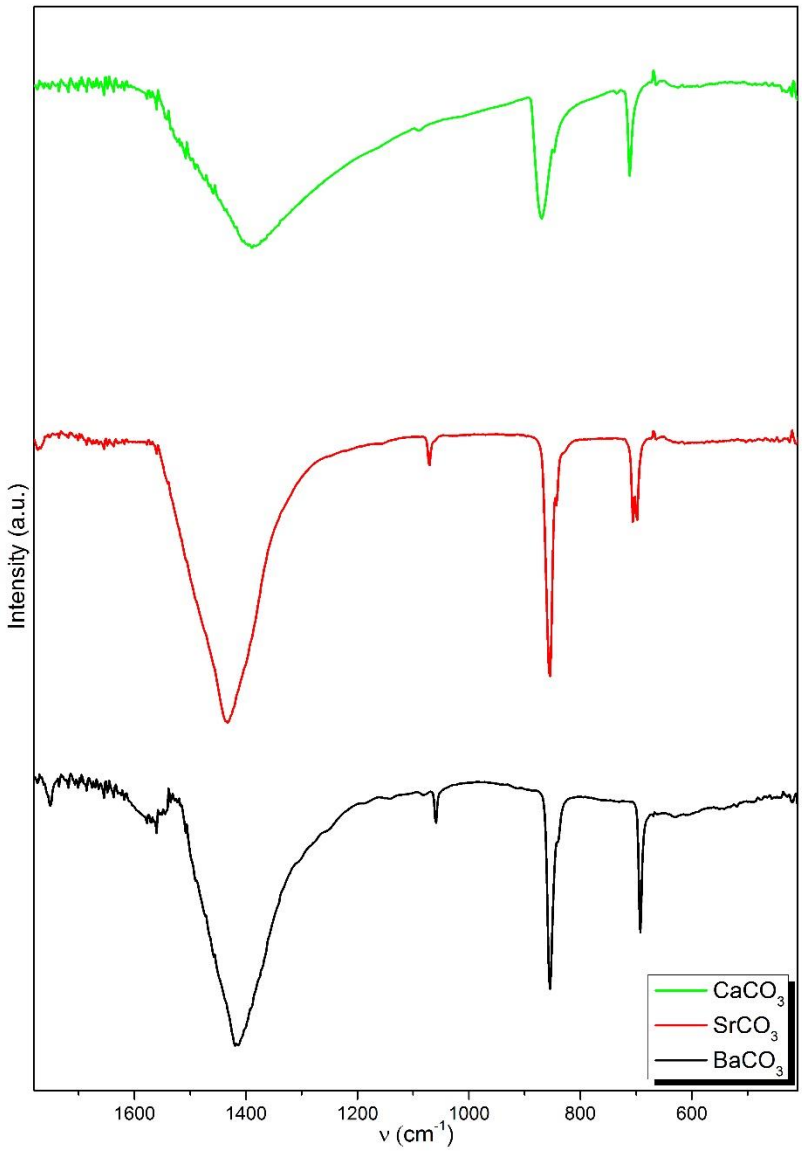

Figure 2.S4: FTIR spectra of ACO_3 nanoparticles.

CHAPTER 3

STABILIZATION OF TRIGONAL STRONTIUM CARBONATE IN A NANOPARTICLE "CRUCIBLE"

Davidson, Matthew. To be submitted to CrystEngComm

Abstract:

Trigonal $SrCO_3$ nanoparticles were produced from an air/water free reaction in methanol. This is the first report of trigonal $SrCO_3$, and in fact the only report of any polymorphism in $SrCO_3$ at low temperature and pressure conditions. TEM analysis of the particles shows polycrystalline clusters of nanoparticles consisting of particles with an average individual size of 15.9 nm. The composition and structure was confirmed with FTIR and Raman, where the characteristic orthorhombic $SrCO_3$ were shifted to energies consistent with trigonal $CaCO_3$. FTIR and Raman show an additional set of peaks associated with a methanol bound-shell around the nanoparticles. SS-NMR shows presence of methanol in both the ^{1}H and ^{13}C spectra as well a new carbon binding environment at 163 ppm. A theoretical trigonal $SrCO_3$ structure was modeled and the generated spectra and diffraction patterns were in good agreement with the experimental FTIR, Raman and PXRD data.

Results and discussion:

$SrCO_3$ synthesis with $NaHCO_3$:

The synthesis of trigonal $SrCO_3$ nanoparticles is done under N_2 in an initially H_2O free environment. This is in contrast to the work shown in chapter 2 where group II metal carbonates are synthesized in air with hydrated chloride salts. The difference in products between the two $SrCO_3$ syntheses is attributed to the reduction in water content. Additionally the reaction was optimized especially just for the $SrCO_3$ reaction and the ideal reaction temperature was adjusted down to 70 °C. This lowers the pressure in the system down to 1.31 Bar.

SEM and TEM analysis of the product shows large polycrystalline spheres with various diameters (150 nm – 300 nm) (Figure 3.1). These spheres are made up of small individual crystallites. SAED of the clusters gives polycrystalline rings (Figure 3.1). Some of the rings are indexed to orthorhombic $SrCO_3$ but there are other rings that cannot be indexed to that structure. This indicates that the product is a mixture of phases. Particle size analysis reveals an fitted diameter of 15.9 nm (Figure 3.2). HRTEM of the particles shows the polycrystalline nature of the particles in greater detail (Figure 3.3). Individual crystal domains are seen in the larger spheres with random orientations.

Orthorhombic $SrCO_3$ has six characteristic peaks in FTIR analysis: 1436 cm^{-1} (E_{g**}), 1070 cm^{-1} ($A_{1u,}$ A_{1g}), 854 cm^{-1} (A_{2g}), 842 cm^{-1} (A_{2u}), 706 cm^{-1} (E_g), and 698 cm^{-1} (E_u). FTIR analysis of the $SrCO_3$ nanoparticles shows significant shifts in the peaks associated with the carbonate (Figure 3.4). When compared against orthorhombic $SrCO_3$ the peaks at 854 and 1070 cm^{-1} red shift to 871 and 1084 cm^{-1} respectively, and the peaks at 1437 and 842 cm^{-1} blue shift to 1392 and 825 cm^{-1} respectively. The two peaks at 706 and 698 cm^{-1} show no significant shift. The new vibrational

energies are similar to trigonal $CaCO_3$, which suggests that the $SrCO_3$ nanoparticles also may be trigonal.

In addition to the carbonate peaks there is another set of peaks in the IR. A possible explanation is that these peaks belong to a MeOH-$SrCO_3$ shell on the particles. During the reaction some of the MeOH binds to the outside of the nanoparticles as they form. This bound

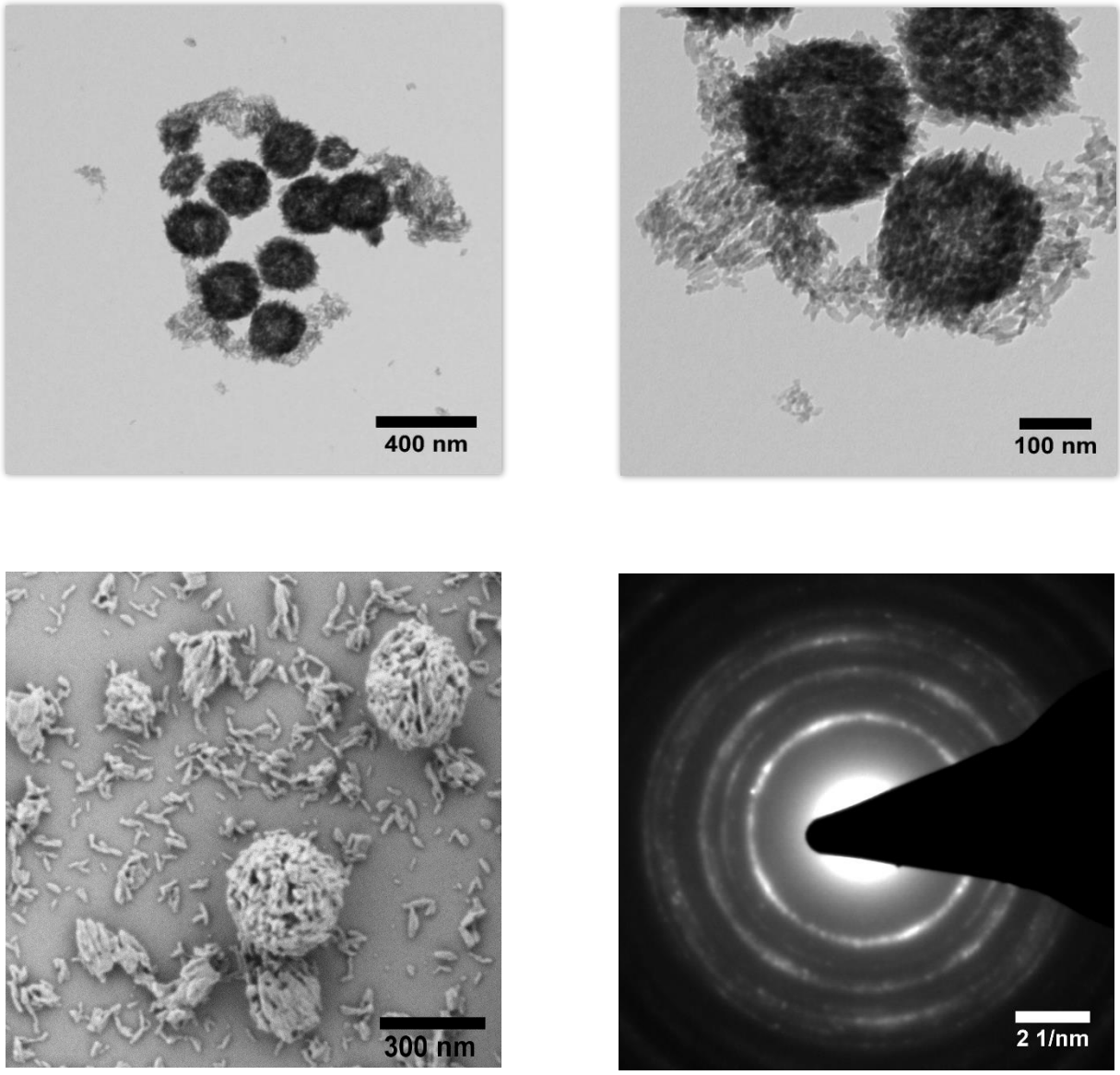

Figure 3.1: a) TEM images showing the large clusters, b) TEM image showing the individual nanoparticles that make up the larger clusters, c) SEM image showing the 3 dimensionality of the spheres, d) SAED showing the polycrystalline rings for the clusters.

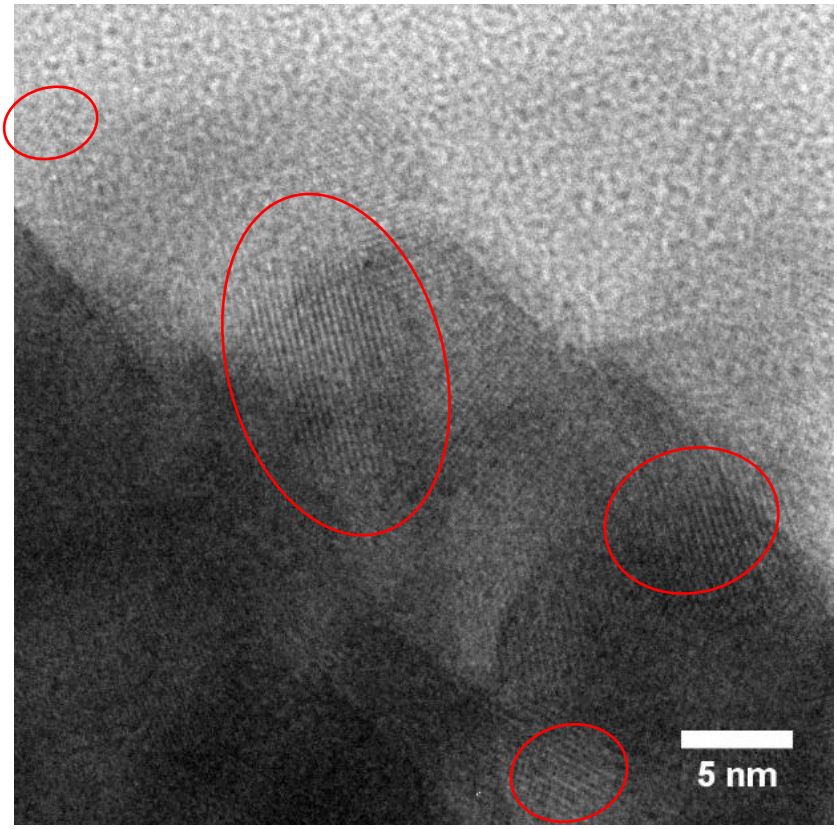

Figure 3.2: HRTEM images showing the individual crystal domains in the spherical clusters. There is no overall orientation, which indicates the polycrystalline nature of the cluster.

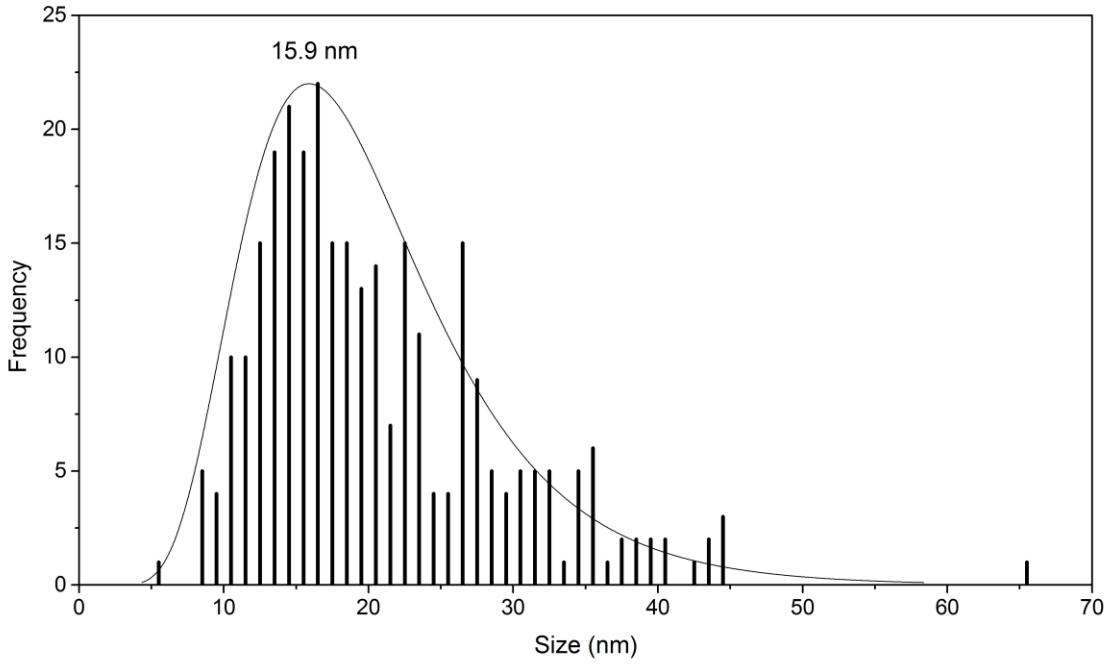

Figure 3.3: TEM particle size distribution with the fit curve shown. n = 300

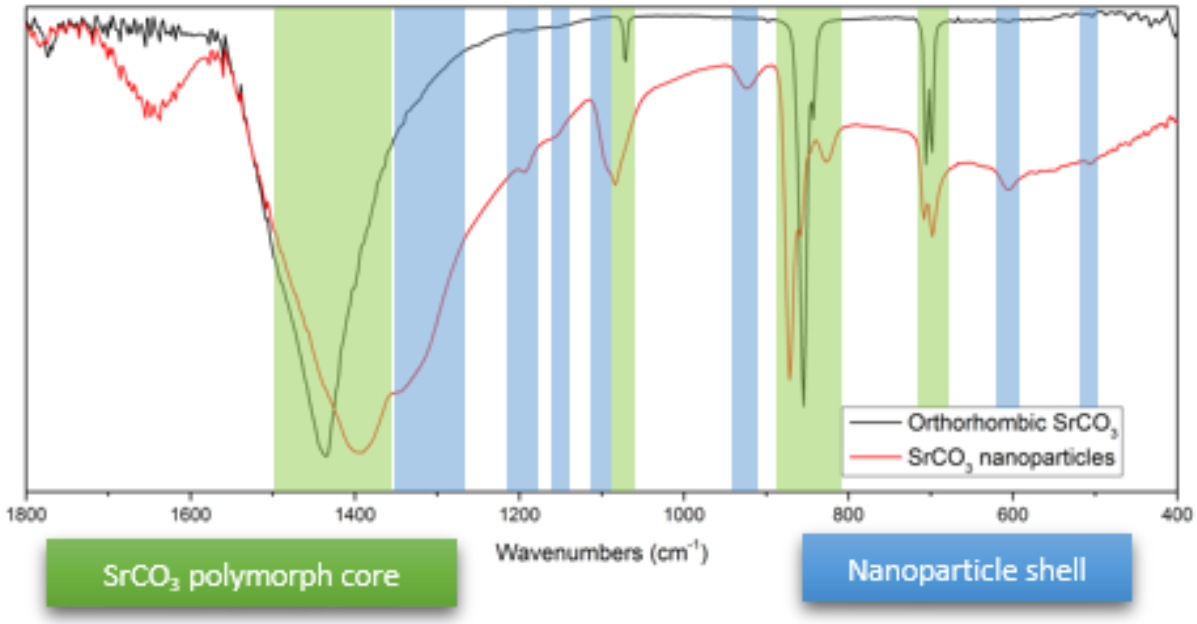

Figure 3.4: FTIR spectra showing the shifts in the orthorhombic $SrCO_3$ peaks in the SrCO3 nanoparticle and the additional set of peaks belonging to the MeOH bound shell.

MeOH surround the particle in a shell. When then the MeOH evaporates off during the drying step the bound shell remains and is seen in the FTIR. This identification was confirmed using isotopic labeling. When $NaH^{13}CO_3$ was used, all of the peaks associated with the $SrCO_3$ shifted their energies and when CD_3OD was used all of the peaks associated with the shell shifted (Table 3.1).

The presence of a $SrCO_3$ polymorph and methanol bound shell was further corroborated with Raman analysis. Orthorhombic $SrCO_3$ has characteristic peaks at 1074 cm^{-1}, 699 cm^{-1}, 176 cm^{-1}, and 143 cm^{-1}. The trigonal $SrCO_3$ nanoparticles have shifted peak positions. The peak at 1074 cm^{-1} is red shifted to 1088 cm^{-1}, 699 cm^{-1} red shifted to 703 cm^{-1}, 176 cm^{-1} blue shifted to 164 cm^{-1}, and 143 cm^{-1} blue shifted to 133 cm^{-1} (Figure 3.5). Just as in the FTIR, there are additional peaks that do not belong to a $SrCO_3$ species. These are the methanol bound shell peaks.

In an effort to elucidate the core-shell interaction, solid state NMR spectra for ^{13}C and ^{1}H nuclei were acquired. The ^{1}H spectrum shows signal from two unique binding environments: one

	t-$SrCO_3$ – $NaHCO_3$ - MeOH	*o*-$SrCO_3$ – $NaHCO_3$ - MeOH	*t*-$SrCO_3$ – $NaHCO_3$ – CD_3OD	*o*-$SrCO_3$ – $NaHCO_3$ - CD_3OD	*t*-$SrCO_3$ – $KH^{13}CO_3$	*o*-$SrCO_3$ – $KH^{13}CO_3$
E_g,E_u	1392 cm^{-1}	-	1398 cm^{-1}		1360 cm^{-1}	
A_{1g}, A_{1u}	1084 cm^{-1}	-	1084 cm^{-1}	1070 cm^{-1}	1082 cm^{-1}	
A_{2g}	872 cm^{-1}	-	872 cm^{-1}	856 cm^{-1}	845 cm^{-1}	
A_{2u}	858 cm^{-1}	847 cm^{-1}	-	847 cm^{-1}	833 cm^{-1}	
E_g	708 cm^{-1}	-	708 cm^{-1}		706 cm^{-1}	
E_u	698 cm^{-1}	-	698 cm^{-1}		694 cm^{-1}	
1	1342 cm^{-1}		1439 cm^{-1}		1319 cm^{-1}	
2	1192 cm^{-1}		-		1192 cm^{-1}	
3	1095 cm^{-1}		1105 cm^{-1}		1093 cm^{-1}	
Free MeOH	-		-		-	
5	922 cm^{-1}		985 cm^{-1}		916 cm^{-1}	
6	827 cm^{-1}		825 cm^{-1}		800 cm^{-1}	
7	607 cm^{-1}		594 cm^{-1}		604 cm^{-1}	

Table 3.1: A list of the major peaks in the FTIR spectra and how these peaks change when ^{13}C and ^{2}H labeling was done. The $SrCO_3$ vibrational modes are labeled with their symmetries while the shell peaks are listed as numbers.

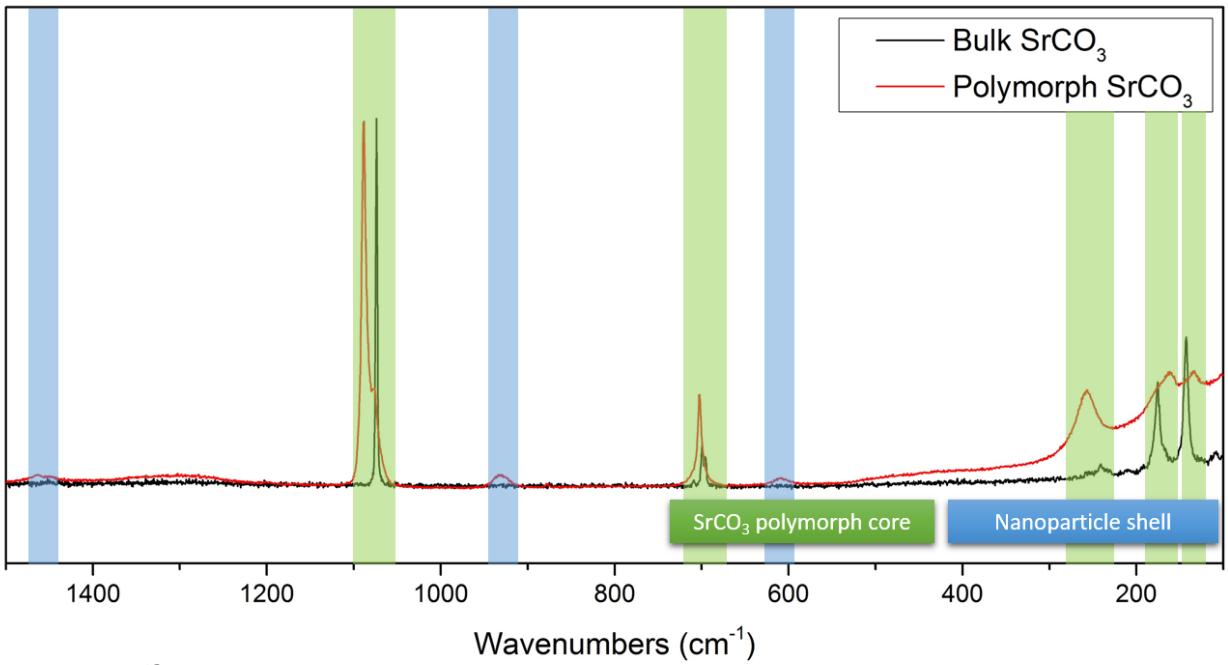

Figure 3.5: ^{13}C SS-NMR spectra of the trigonal $SrCO_3$ nanoparticles excited via direct and cross polarization.

at 3.91 ppm corresponding to the CH_3 protons on the MeOH and another at 5.40 ppm corresponding to the OH proton (Figure 3.6). When the reaction is run with CD_3OD the peak at 3.91 ppm disappears but the peak at 5.40 ppm remains, most likely due to free exchange with hydroxyl from atmospheric water.

For the ^{13}C experiments the samples were enriched with $NaH^{13}CO_3$. The direct polarization spectrum of ^{13}C shows four unique binding environments: 49.5, 125.6, 162.3 and 170.7 ppm (Figure 3.7). The peaks at 49.5 and 170.7 ppm are associated with MeOH and $SrCO_3$, respectively. The peak at 125.6 ppm corresponds to free CO_2. The reaction is conducted under an inert environment so any CO_2 present is released/trapped during the reaction. Finally the peak at 162.3 ppm is associated with the carbonate bound to shell. This peak is close in energy to the $SrCO_3$ peak and most likely comes from a CO_3^{2-}-type carbon. When a cross-polarization experiment is run there is a significant shift in the relative intensities of the two carbonate peaks (Figure 3.7). The peak at 162.3 ppm increases in intensity indicating that this carbon is in close proximity with the protons in the system. It was established earlier that the only protons in the system come from MeOH, which means that the 162.3 ppm peak has a close interaction with the MeOH, further corroborating our core-shell model. Additionally, in the cross-polarization experiment, the peak at 125.6 ppm disappears completely. This is expected because free CO_2 should have no interaction with the protons available in the system.

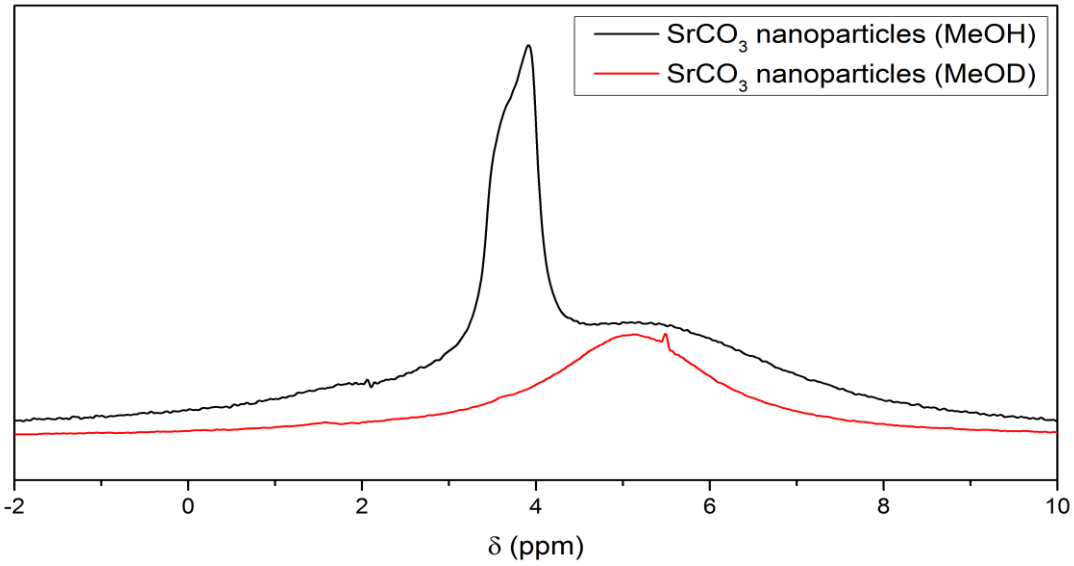

Figure 3.6: ^{1}H SS-NMR spectra of the trigonal $SrCO_3$ nanoparticles and the CD_3OD labeled reaction. Both show a signal associates with methanol.

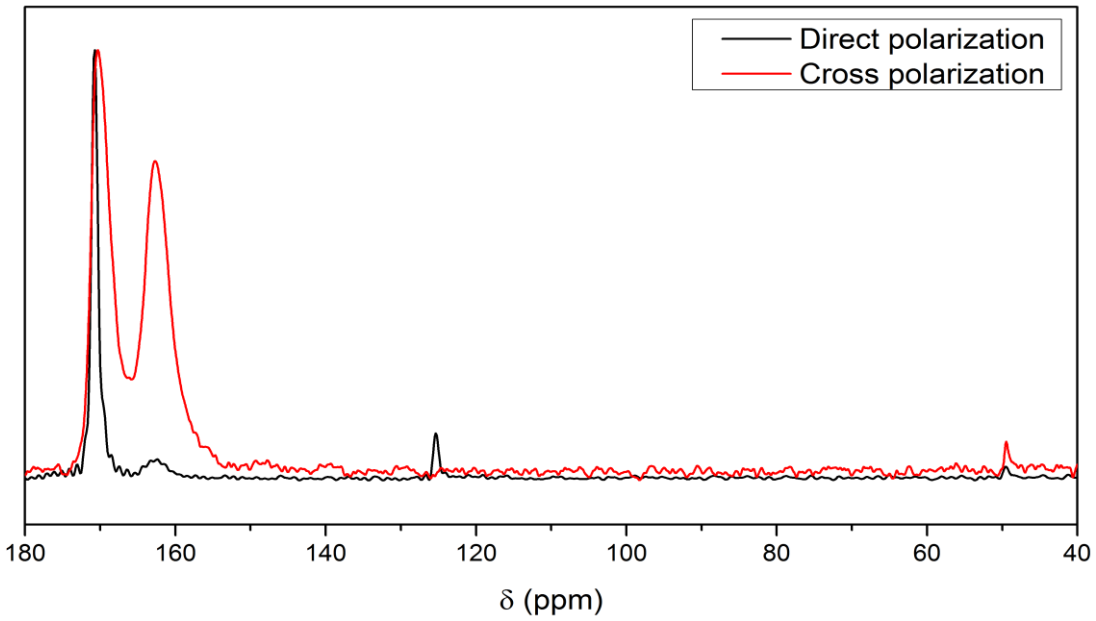

Figure 3.7: ^{13}C SS-NMR spectra of the trigonal $SrCO_3$ nanoparticles excited via direct and cross polarization.

The PXRD data did not match orthorhombic $SrCO_3$ (Figure 3.8). Additionally the broadness of the peaks indicates nanosized particles. Looking at the PXRD it is clear that the sample is a mixture of some orthorhombic $SrCO_3$ and another pattern. This second pattern can be attributed to trigonal $SrCO_3$, consistent with the prior FTIR data.

Trigonal $SrCO_3$ was modeled for comparison against the experimental data. To do this the trigonal $CaCO_3$ structure was used as a template. The calcium is substituted with strontium and the overall lattice adjusted. The results structure has rhombohedral symmetry with a=b=c= 6.53 Å and an angle of 46.09°. Looking at the IR and Raman data there is good agreement with the calculated spectra with respect to peak positions (Figure 3.9). A calculated PXRD pattern was generated from the trigonal structure but it did not accurately account for the peak splitting in the 26° and 33° peaks. The trigonal structure is a high symmetry structure, therefore relatively few

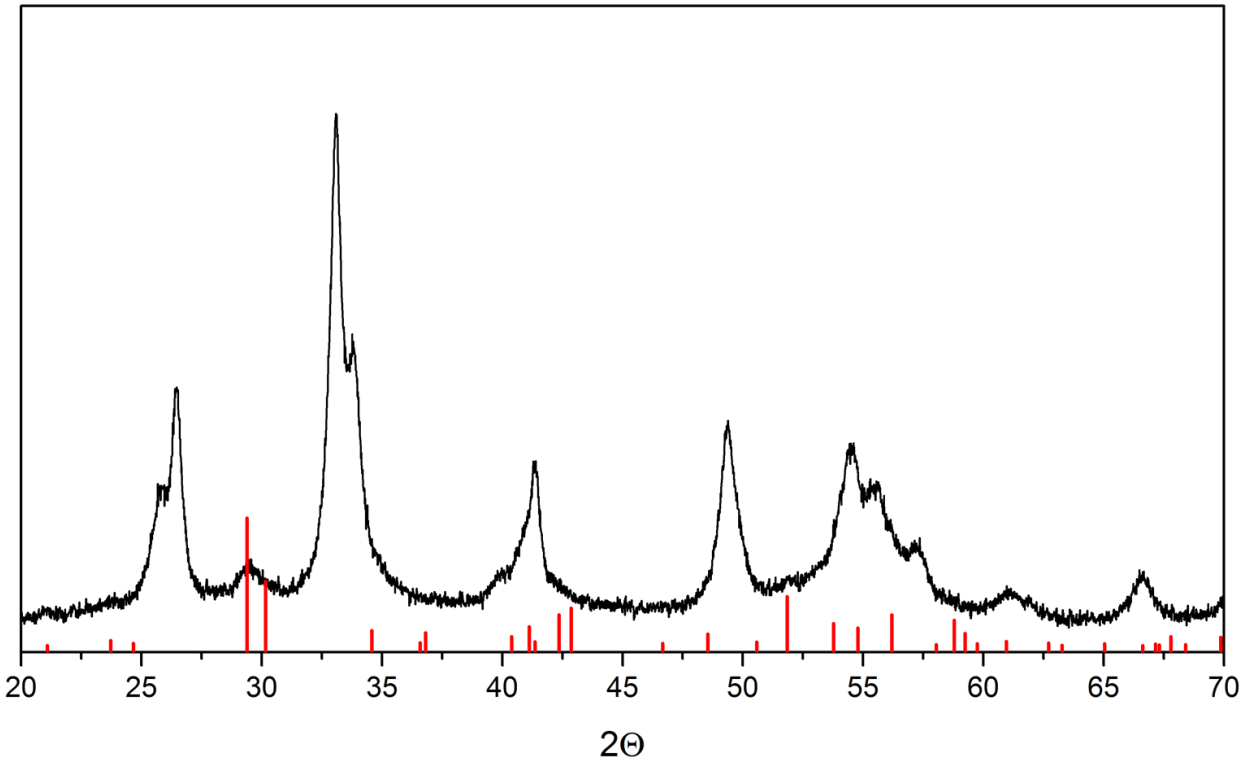

Figure 3.8: PXRD pattern of the $SrCO_3$ nanoparticles with orthorhombic $SrCO_3$ drop lines shown.

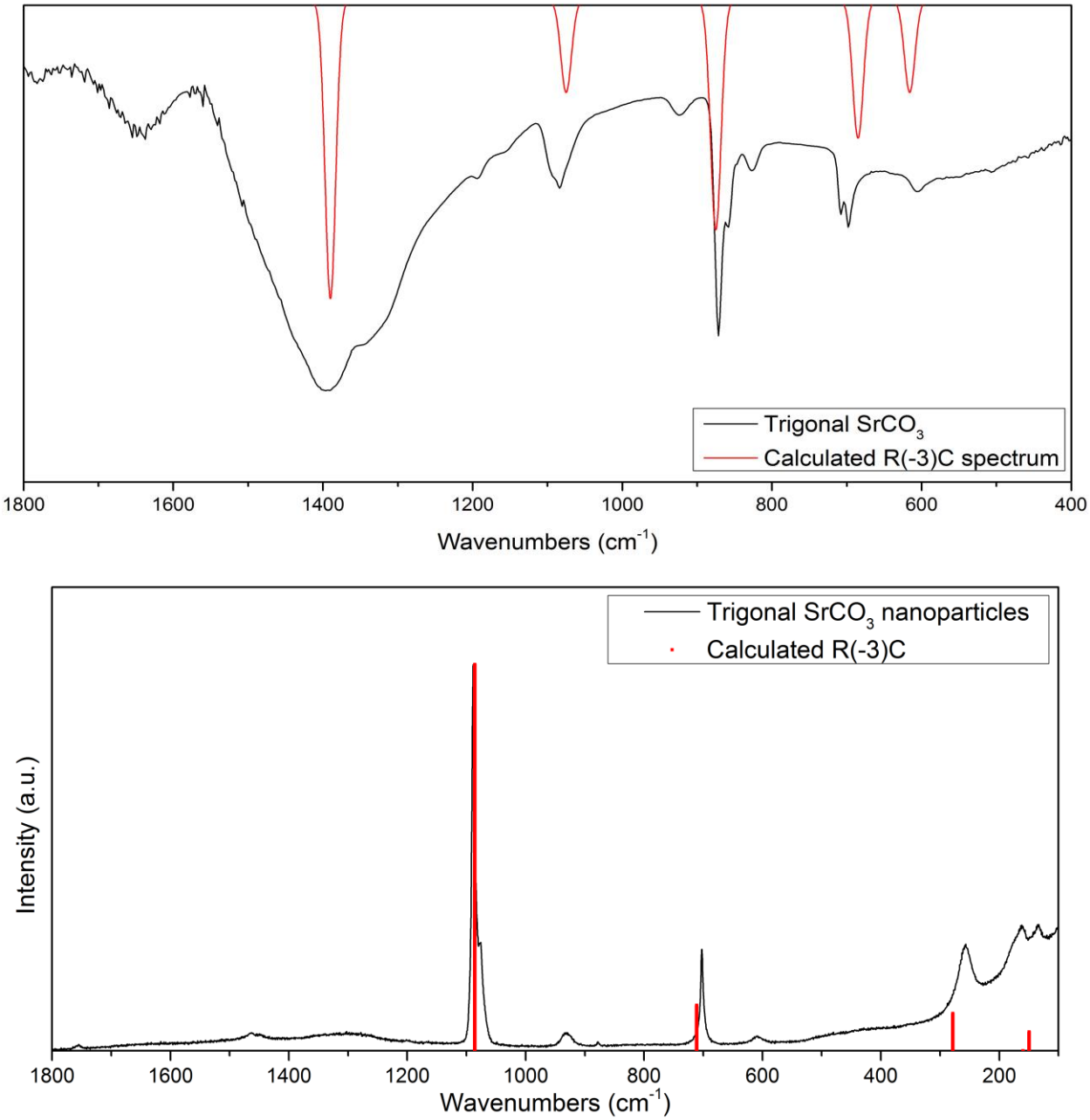

Figure 3.9: Experimental trigonal $SrCO_3$ IR and Raman with the calculated R(-3)C spectra overlaid.

peaks are expected. In our sample the peaks at 26° and 33° are split indicating a two phase trigonal system. This changed was model as two different trigonal species. This is in agreement with the proposed core-shell model where the $SrCO_3$ bound to the shell would be crystallographically

distorted. With this change a more accurate PXRD fit was generated that reproduces the peak splitting (Figure 3.10).

An important point about the new trigonal $SrCO_3$ phase is that it is metastable. Over the course of 8 days the trigonal species transforms into orthorhombic $SrCO_3$. This phase transition is elucidated using DSC. At 330 °C there is an exothermic event associated with the transition from trigonal to orthorhombic (Figure 3.11). This fact is confirmed with FTIR, which shows a loss of all trigonal peaks and the appearance of orthorhombic $SrCO_3$ peaks. This transformation is also accelerated by the loss of the MeOH shell. When the sample is heated about 80 °C there is a loss of the shell peaks, and such a sample convert to pure orthorhombic $SrCO_3$ over the course of 8 hours.

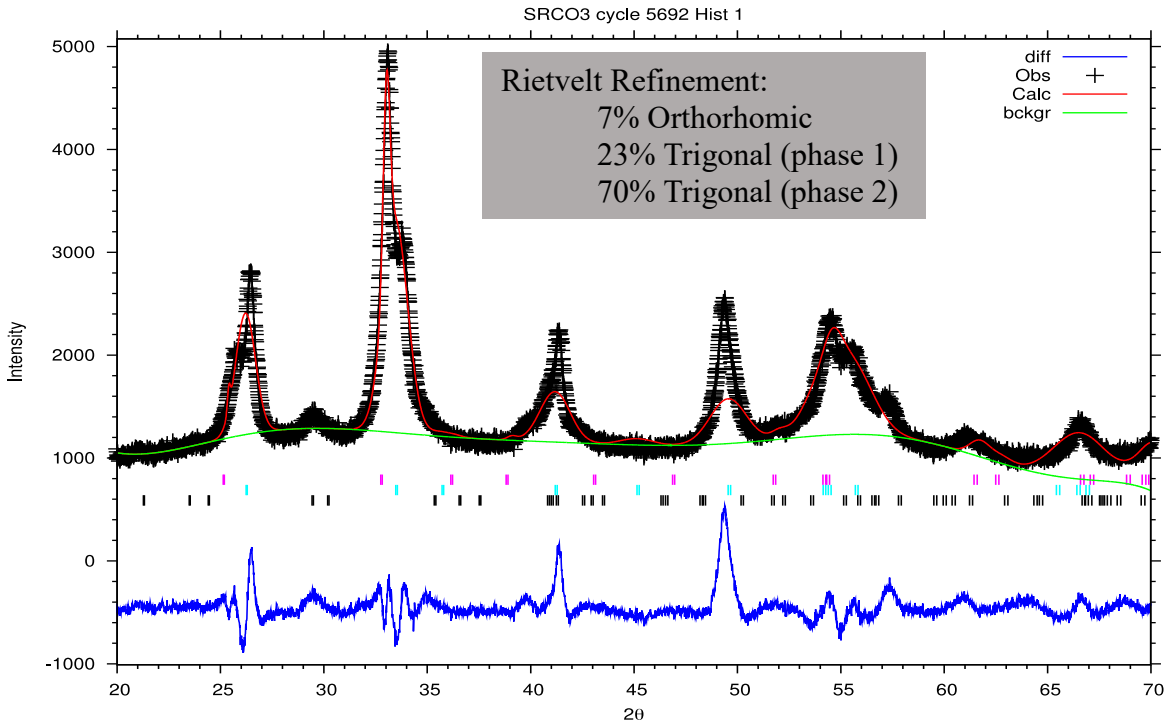

Figure 3.10: The experimental PXRD of $SrCO_3$ nanoparticles with the Riervelt refined calculated pattern shown. It is a three species system with 2 trigonal phases and the orthorhombic phase.

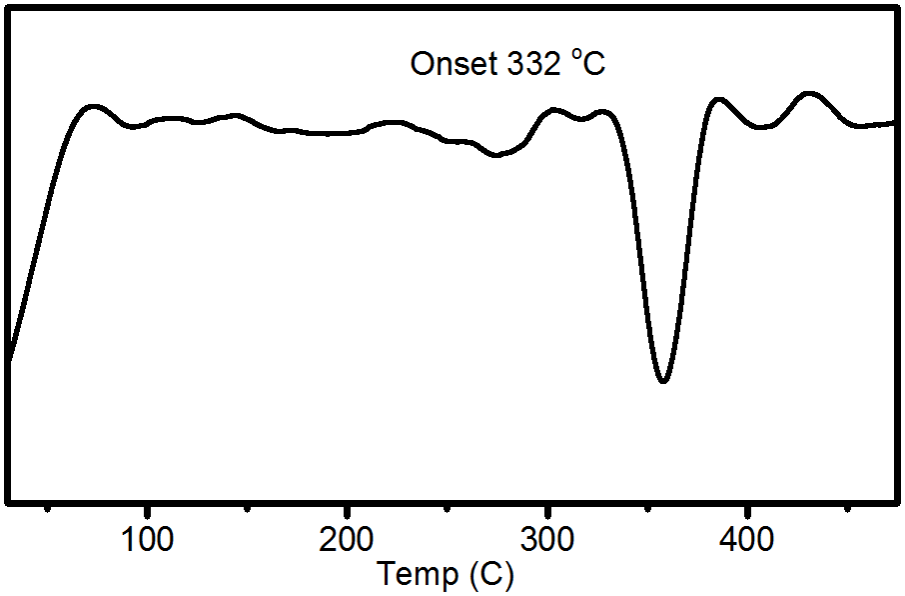

Figure 3.11: DSC of the trigonal $SrCO_3$ nanoparticles that shows an exothermic event with an onset at 332 °C.

$SrCO_3$ synthesis with $KHCO_3$:

Changing the carbonating reagent to $KHCO_3$ has a significant impact on the product produced. Looking at TEM, the large spherical clusters are no longer form. Instead, bow tie / ellipsoidal shaped clusters are produced with smaller lateral dimensions (100 nm – 150 nm) (Figure 3.12). The SAED shows a polycrystalline pattern indicating that these clusters are composed of smaller individual crystallites (Figure 3.12). FTIR of the sample shows a mixture of the trigonal and orthorhombic $SrCO_3$ species (Figure 3.13). The product of the $KHCO_3$ reactions had a noticeably longer retention of MeOH. The peaks associated with the shell had greater intensity than seen with the $NaHCO_3$ reactions. Additionally, the IR showed peaks associated with free MeOH such as the peak at 1000 cm^{-1}, and the increased signal in the C-H region. Isotopic labeling shows similar shifts to those seen in the $NaHCO_3$ reactions (Table 3.1).

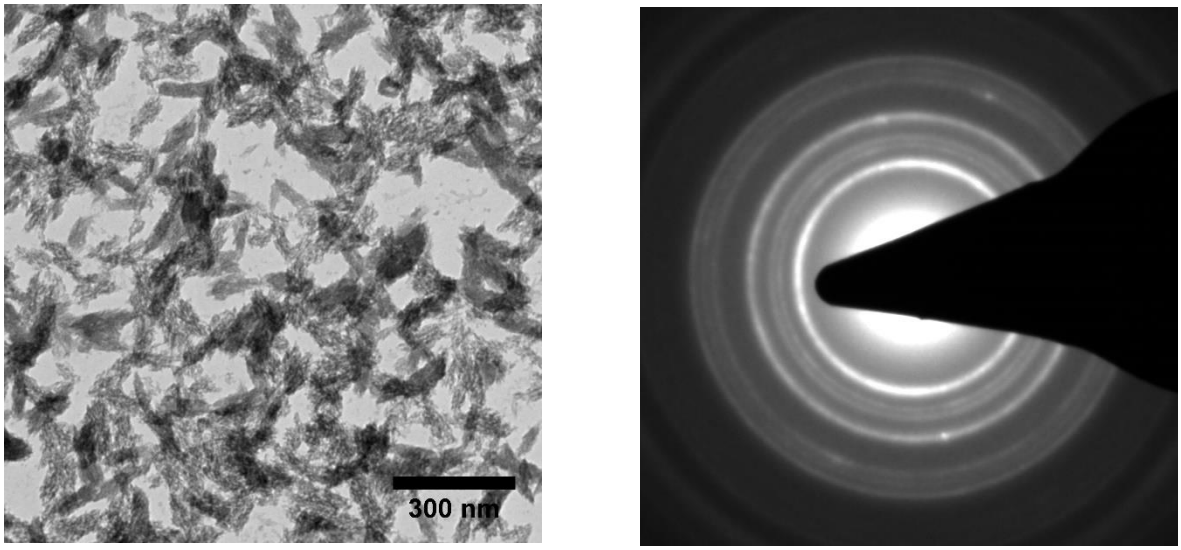

Figure 3.12: a) TEM image of the $SrCO_3$ clusters of nanoparticles produced using $KHCO_3$, b) SAED of the clusters shows a strong orthorhombic pattern.

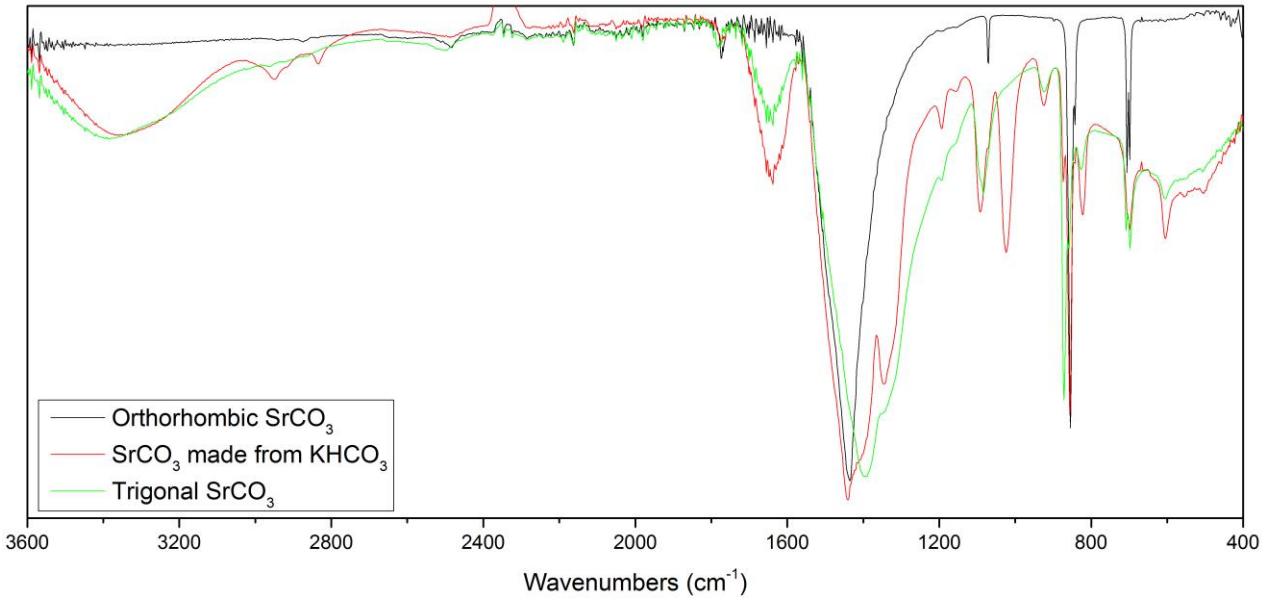

Figure 3.13: FTIR of the $SrCO_3$ nanoparticles produced with $KHCO_3$ showing a mixture of the orthorhombic and trigonal phases as well as a significant MeOH presence.

Conclusions:

Trigonal $SrCO_3$ nanoparticles clusters were synthesized with a methanol reaction in an air and water free environment. The size of these particles was confirmed with TEM and showed an average particle size of 15.9 nm. The clusters seen in TEM were shown to be made of individual crystallites using HRTEM to map the lattice spacings. FTIR and Raman showed significant energy shifts from the typical orthorhombic $SrCO_3$. These shifts were predicted by theoretical calculations modeling a trigonal $SrCO_3$ structure. In addition to the $SrCO_3$ peaks, there were new peaks associated with a methanol-bound shell surrounding the nanoparticles. The correspondence of these peaks with the methanol was shown via a series of isotopic labeling experiments. SS-NMR confirmed the presence of methanol showing signal in both the ^{1}H and ^{13}C spectra. The ^{13}C spectrum also showed a new binding environment at 163 ppm which is associated with the methanol-bound shell layer, and this interaction was demomstrated with a cross polarized experiment. Additionally the peak at 125.5 ppm is free CO_2 which means the particles are trapping CO_2 gas as it forms in the reaction in real time, a phenomenon usually seen in high pressure systems. This combined with the polymorphism indicates that the reaction is behaving as if it is under a high pressure. Rapid nanoparticle formation acts like a high pressure crucible, giving geologic-like conditions. The PXRD pattern could not be matched to orthorhombic $SrCO_3$ and indicated a multiple species sample. Calculated PXRD pattern from the trigonal structure that it is a three phase mixture with two trigonal structures making up 93% of the sample and a small 7% orthorhombic presence. The transition from trigonal to orthorhombic was observed with DSC and the exothermic event seen with an onset at 332 °C. When the carbonation reagent is changed to $KHCO_3$ instead of $NaHCO_3$, similar results are seen but the trigonal phase is a small minority phase.

Experimental

Materials

$SrCl_2$ (≥95% purity, anhydrous) was purchased from Strem Chemicals. $NaHCO_3$ (≥99% purity) from J.T. Baker was used as received. Anhydrous methanol (99.8%) and $KH^{13}CO_3$ from Sigma Aldrich were used as received. $NaH^{13}CO_3$ (97% purity), CD_3OD (99% purity) and $^{13}CH_3OH$ (99% purity) were used as received from Cambridge Isotopes labs.

Synthesis of $SrCO_3$ nanoparticles

A 100 mL glass ampoule was flame dried and charged with 1.20 mmol of $SrCl_2$, 2 mmol of $NaHCO_3$ or $KHCO_3$, and 20 mL of anhydrous methanol under inert atmosphere. The tube was sealed with a Teflon stopcock and placed in a 70 °C heating bath with stirring for 3 h. When the reaction was complete, the mixture was centrifuged at 10,000 rpm for 10 min. The supernatant was removed and fresh methanol (20 mL) added to dissolve residual NaCl. The mixture was centrifuged again at 10,000 rpm for 10 min, and the supernatant was discarded again. The solid was dried in air for 30 min. The product was isolated as a white powder: 0.1102 g (75.5% yield) for $NaHCO_3$ and 0.1091g (71.2 % yield) for $KHCO_3$.

Characterization

NMR was carried out using a Bruker AV3-400 400 MHz and a Bruker DSX300 at 300 MHZ. Transmission electron microscopy (TEM) images and selective area electron diffraction (SAED) patterns were collected using a Tecnai 20 electron microscope operated at 200 keV. Energy dispersive spectroscopy spectra were collected on a Zeiss 1450EP SEM using an equipped Oxford SDD-EDX. Scanning electron microscopy (SEM) images were collected on an FEI Inspect F field emission gun microscope. FTIR spectra were collected on a ThermoNicolet 6700 spectrophotometer running the OMNIC software with ATR diamond

CHAPTER 4

METAL TITANATES INTRODUCTION AND LITERATURE REVIEW:

Origin and grouping:

Perovskites are a group of materials with the general formula ABO_3. They are named after the mineral perovskite, which is $CaTiO_3$. Many perovskites are used for their interesting electronics properties, such as ferroelectricity, piezoelectricity and thermoelectricity.[1] Additionally they are used as photocatalysts and in photovoltaic applications, and new perovskites continually are being developed to further expand their utility.[2] In perovskites the B atom is at the center of an octahedral bound to six face-centered oxygens (Figure 4.1). The A atoms are located at the corners of the unit cell. The position of the B atom inside the octahedral is where many of the electronic properties are derived.

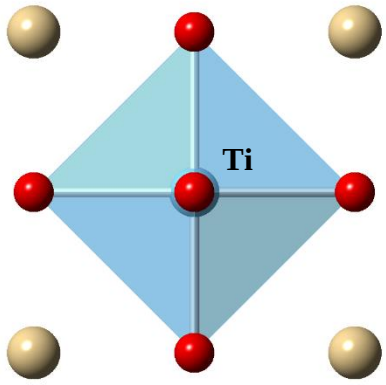

Figure 4.1: Crystal structure of the mineral perovskite ($CaTiO_3$)

The definition of perovskites encompasses many compositions. Possibilities include complex double perovskites like $CaCu_3Ti_4O_{12}$ or non-oxide organometallic halide perovskites, and materials with similar crystal structure are often referred to as perovskite-like.[3]

Dielectrics:

Dielectric materials are insulators that can be polarized under an applied electric field. When the electric field is increased the polarization in the material increases as well. Often dielectrics are made of molecules with an intrinsic dipole moment and these molecules align their dipoles with the direction of the electric field. Dielectrics insulation is measured against that of

pure vacuum, and then assigned a value known as a dielectric constant. The higher value, the better of an insulator it is. Dielectric is an all-encompassing term to which many other types of materials belong and interesting electronic effects are seen in structures that have inherint dipole. Piezeoelectricity, pyroelectricity and ferroelectricity are just a few of the properties that dielectrics can have.

Piezoelectricity:

Piezoelectric is a property used to describe materials the produce electric fields through physical deformation. This is a reversible effect, so when the mechanical stress is released the electric field subsides. Piezoelectric crystals are very useful in applications like balances where the weight of an object can be directly read as a voltage produced by the crystal. In perovskites piezoelectricity is again linked to the position of the B atom (Figure 4.1). The piezoelectric effect is greater in materials with an already present dipole so many ferroelectrics already make good piezoelectrics like $BaTiO_3$ and $PbTiO_3$. Mechanical strain on the crystal changes the position of the B atom which can exaggerate or minimize the dipole moment. This change in spontaneous polarization is measured as a voltage. The more distorted the octahedra are, the greater the piezoelectric response.

Pyroelectricity:

Pyroelectricity is the ability of a material to produce a voltage when heated or cooled. This has a wide arrange of applications for temperature sensing. Pyroelectricity takes advantage of a temperature dependent crystallographic change in the material. Similar to the way the B atom can be shifted with mechanical stress in a piezoelectric, the B atoms position changes based on the

temperature of the crystal. In perovskites higher temperatures stabilize the cubic form. As the B atoms shifts to the symmetric cubic position there is a cooresponding change in the dipole moment of the crystal. This change is measured as a voltage change and is correlated back to a temperature shift.

Ferroelectricity:

Ferroelectric is a property used to describe materials with a spontaneous electric polarization. This would be a structure with an inherent dipole moment. Furthermore ferroelectric material's polarization can be reversed if subjected to an external electric field. This phenomena is very similar to ferromagnetism from which it derived its name. When an electric field is applied to a material, the polarization is a linear response to the strength of the electric field. Ferroelectrics are unique because they are polarized even with no electric field. Additionally when the electric field is reversed to a sufficient degree, ferroelectric materials will reverse their polarization. They then remember that polarization when the electric field is returned to zero. In perovskites this properties is linked to the position of the B atom. Some perovskites have a tetragonal structure but the octahedral is not elongated symmetrically. Instead the B atom is shifted out of the plane of oxygens. This asymmetric shift causes a net dipole moment in the crystal. It is also the spontaneous polarization as well. Some perovskites have a completely cubic structure but a dipole moment can still be induced through an external electric field. These are known as paraelectric materials. The polarization versus electric field curves are shown in figure 6. Ferroelectric materials usually have a Curie temperature associated with them. By analogy to magnetism, the Curie temperature of a ferroelectric material is that above which it loses its ferroelectric properties.

Ferroelectric materials have a wide range of applications the most common one being multi-layer ceramic capacitors (MLCCs). Because of the unique way ferroelectric materials interact with electric fields they tend to have high dielectric constants. They can store more charge with less polarization and when the field is reversed they can discharge very easily. This is why perovskites like $BaTiO_3$ are currently an industrial standard in MLCCs.

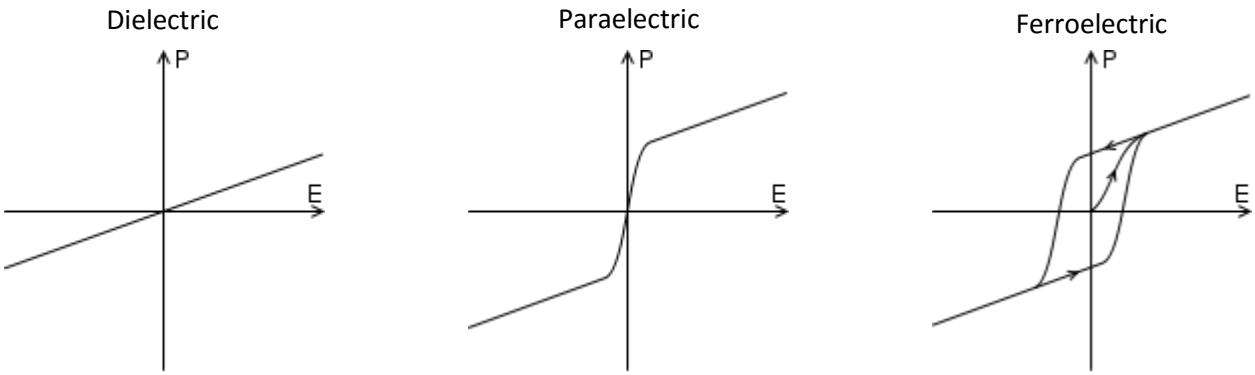

Figure 4.2: Ideal electric field vs. polarization curves that illustrate how the three different materials react to increased field strength.

Barium titanate:

Barium titanate ($BaTiO_3$) is considered the first metal oxide to exhibit ferroelectric behavior. It was discovered during World War II and promptly became the primary material used in the production of capacitors, replacing mica.[4] To this day it is still the dominant active material used in MLCCs.[5] $BaTiO_3$ has a very high dielectric constant > 1200 F/m which is about 10x greater than TiO_2. $BaTiO_3$ has a tetragonal structure with dimensions a,b = 3.999 Å, and c = 4.03265 Å. The titanium atom is out of the plane of the oxygens (Figure 4.3). Titanium bound to the oxygens along the elongated axis is 1.871 Å and 2.162 Å. The small difference in bond length causes the net dipole

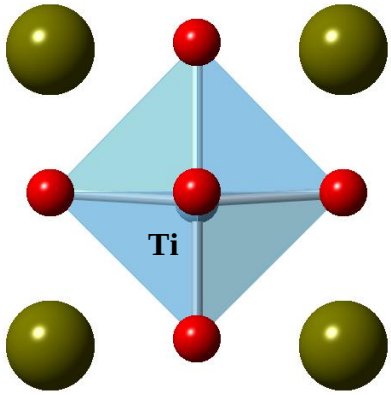

Figure 4.3: Crystal structure of barium titanate that shows the out of plane Ti atom.

in $BaTiO_3$, which is responsible for ferroelectricity in the material. $BaTiO_3$ has a Curie temperature of 120 °C, above which it converts to the cubic structure and ferroelectricity is lost. Additionally the distortions in the crystal structure can be exaggerated with cooling to an orthorhombic and rhombohedral phase.[6]

As mentioned earlier the most common way to produce $BaTiO_3$ is the solid state reaction between TiO_2 and $BaCO_3$.[1a] Unfortunately while solid state reactions tend to give a homogeneous products they fail to provide control over size or morphology. As the electronics industry moves to a smaller and smaller scale, developing alternative synthetic routes is an increasing priority. A promising synthetic approach is hydrothermal reactions, which are those that use aqueous media above the normal boiling point of water. Metal autoclaves are used to contain the pressure. The typical reaction uses anatase (TiO_2) and $Ba(OH)_2 \cdot 8H_2O$ and has a dissolution / nucleation mechanism.[7] The $Ba(OH)_2$ acts as a mineralizer and dissolves the TiO_2 into $Ti(OH)_x^{4-x}$ which readily reacts with the present Ba^{2+} ions to form $BaTiO_3$.[8] Particles grown this way range in size from 50 nm - >1 μm and often have a cube like shape.[8a, 8c, 9] Other mineralizers can be used as well, such as NaOH or KOH. When using TiO_2 as a precursor it is important to use alkali conditions to promote the formation of $Ti(OH)_x$ species. Hydrothermal reactions grant access to a wide variety of control through the addition of different salts and surfactants.[10]

$BaTiO_3$ commonly forms 3D cube like structures. There has been much work looking at 1D structures such as rods and wires. Rod shaped $BaTiO_3$ was obtained using traditional crystal pulling methods as well as molten salt flux reactions as well.[11] Additionally 1D $BaTiO_3$ was synthesized on a $K_2Ti_4O_9$ template. Nanorods of potassium tetratitanate and potassium hexatitanate were used as the template for the synthesis of $BaTiO_3$.

Moving to 2D structures proves to be a more difficult task for perovskite structures. Traditionally $BaTiO_3$ thin films are grown epitaxially on another similar single crystal such as $SrTiO_3$ or $SrRuO_3$.[12] Epitaxial growth uses techniques like molecular beam, laser ablation or chemical vapor deposition (CVD) to assemble thin films anchored to a substrate. Depending on the control of the system, a few layers to hundreds of layers can be grown. The methods require gaseous reagents such as titanium isopropoxide and barium diketonate flowing inside the chamber. Interesting enough the films still show a ferroelectric response down to 9 nm in thickness.[13] This is in contrast to nanoparticles of $BaTiO_3$ where the ferroelectric response is lost as size is reduced below 30 nm. Additionally strained epitaxial growth of $BaTiO_3$ actually can increase the ferroelectric response and stabilize it to much higher temperatures.[14]

Aside from thin films of $BaTiO_3$ there is also interest in 2D platelets. These platelets are free standing, independent of any substrate. Synthesis of 2D morphology $BaTiO_3$ is achieved using template effects. Layered structures like $BaBi_4Ti_4O_{15}$ can be converted via a topotactic reaction to $BaTiO_3$.[15] Evidence of templating effects are seen in cases where different structured titanium sources are used. When a layered titanate like $H_{1.07}Ti_{1.73}O_4$ is used the resulting $BaTiO_3$ formed is also a layered platelet structure.[16] It is important to note that these are not considered in the nanoregime of size. The platelets often have lateral dimensions > 5 μm and thickness in the hundreds of nanometers.

Lead Titanate:

Lead titanate ($PbTiO_3$) is one of the best piezoelectrics available today. It was surpassed recently by a derivative lead zirconium titanate ($PbZr_xTi_{1-x}O_3$). Like $BaTiO_3$, $PbTiO_3$ has a tetragonal structure with a,b = 3.8991 Å and c = 4.1536 Å. Titanium bound to the oxygens along the elongated axis is 1.670 Å and 2.482 Å, a difference of 0.812 Å. The elongation along the c axis is significantly more pronounced than $BaTiO_3$. The titanium atom is even further displaced out of the center of the octahedral (Figure 4.4). This leads to the very large piezoelectric response in $PbTiO_3$ compared against $BaTiO_3$. The Curie temperature of $PbTiO_3$ is 720 °C.

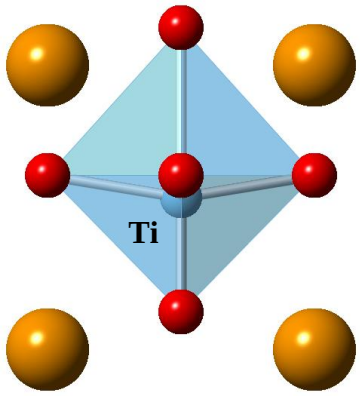

Figure 4.4: Crystal structure of lead titanate that shows the greater out of plane distortion.

Many of the reactions that produce $BaTiO_3$ can be adapted to synthesize $PbTiO_3$ as well. The solid state reaction between $PbCO_3$ and TiO_2 will produce $PbTiO_3$ when sintered above 900 °C.[17] Alternatively PbO can be used directly as a precursor because it is quite stable. Hydrothermal reactions to produce $PbTiO_3$ function along the same dissolution / nucleation mechanism.[18] Unlike $BaTiO_3$ there is no stable $Pb(OH)_2$ analog to use as an alkali source and mineralizer. Thus with hydrothermal $PbTiO_3$ reactions mineralizers like NaOH, KOH and NH_4OH are relied upon.[19]

Applications have increasingly required a degree of morphology control for their materials. With $PbTiO_3$ there is interest in both 1D and 2D morphologies. Nanorods of $PbTiO_3$ are grown hydrothermally in the [001] using sodium dodecylsulfate as a surfactant.[20] These rods are phase pure and have a piezoelectric response with a width < 40 nm.[20] Other 1D structures like nanotubes are synthesized using a templating method where TiO_2 nanotubes are converted to $PbTiO_3$.[21] A consistent method for making $PbTiO_3$ nanorods uses nanochannel alumina pores. Nanochannel

alumina provides a rigid structure for the $PbTiO_3$ to grow within and then the alumina is etched away leaving nanorod array of $PbTiO_3$.[22]

Thin films of $PbTiO_3$ can be epitaxially grown. A $SrTiO_3$ single crystal is added to the autoclave. The $SrTiO_3$ provides the substrate for the $PbTiO_3$ to grow onto during the reaction which leads to the deposition of a thin film.

Nanosheets:

Nanosheets are a class of material that has large lateral dimensions with thicknesses in the nanoregime. They are 2D nanomaterials that are free standing and form suspensions. Nanosheets gained wide spread attention with the discovery of graphene in 2003 by Geim and Novoselov and later notoriety with the Nobel Prize in 2010.[23] Nanosheets show remarkable physical stability and strength at the limit of thickness, one monolayer.[24] Graphene grabs attention and headlines but it is not the only nanosheet material. Other materials like metal oxides and metal dichalcoganides are isolable as nanosheets. Structures like graphene and dichalgonides are layered materials where the layers are held together with van der Waals forces.[25] This weak force is easily overcome and leads to a myriad of exfoliation techniques like; scotch tape, ultrasonication and even blenders.[26] With metal oxides like titanium oxide a different approach is required. The tradition polymorphs of TiO_2, anatase, rutile and brookite are not inherently layered structures. To overcome this challenge Sasaki developed a method that involves the exfoliation of akali metal titanates.[27] $Na_2Ti_3O_7$, $K_2Ti_4O_9$ and $Cs_2Ti_5O_{11}$ have layered crystal structures, with alternating layers of Ti-O octahedral and akali ions. Through chemical leeching and exfoliation Sasaki obtained large nanosheets of $Ti_xO_{2x+1}^{2-}$.[28] These sheets behaved very similarly to a synthetic structure of TiO_2 known as TiO_2 (B). The Sasaki process is shown in figure 4.5:

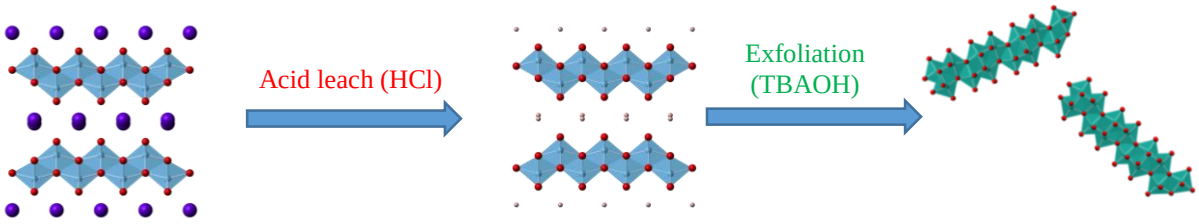

Figure 4.5: Schematic illustrates the exfoliation of layered titanates using soft-chemical exfoliation.

Research goals:

The goal of this research is to use TiO_2 nanosheets as a template to synthesize perovskite nanosheets. Moving down into the nano regime has proved difficult for $BaTiO_3$. As the grain size decreases the Curie temperature also begins to fall. Nanoparticles < 100 nm of $BaTiO_3$ have a cubic structure. This is problematic when the ferroelectric properties are derived from the tetragonal asymmetry. The goal of the work outlined in this dissertation is to combat the falling Curie temperature by synthesizing 2D nano morphologies. Nanosheets can have lateral dimensions in the microns while maintaining a less than 10 nm thickness.

1. (a) Danielson, G. C.; Rundle, R. E., STRUCTURE OF FERROELECTRIC BATIO3. *Physical Review* **1949,** *75* (10), 1630-1630; (b) Kleemann, W., Discovery of ferroelectricity. *Phys. Rev* **1920,** *15*, 537.

2. (a) Adams, T. B.; Sinclair, D. C.; West, A. R., Characterization of grain boundary impedances in fine- and coarse-grained $CaCu_3Ti_4O_{12}$ ceramics. *Phys. Rev. B* **2006,** *73* (9); (b) Fedulov, S. A., DETERMINATION OF CURIE TEMPERATURE FOR BIFEO3 FERROELECTRIC. *Doklady Akademii Nauk Sssr* **1961,** *139* (6), 1345-&.

3. (a) Zhu, F.; Men, L.; Guo, Y.; Zhu, Q.; Bhattacharjee, U.; Goodwin, P. M.; Petrich, J. W.; Smith, E. A.; Vela, J., Shape Evolution and Single Particle Luminescence of Organometal Halide Perovskite Nanocrystals. *ACS nano* **2015,** *9* (3), 2948-2959; (b) Chiodelli, G.; Massarotti, V.; Capsoni, D.; Bini, M.; Azzoni, C. B.; Mozzati, M. C.; Lupotto, P., Electric and dielectric properties of pure and doped $CaCu_3Ti_4O_{12}$ perovskite materials. *Solid State Communications* **2004,** *132* (3-4), 241-246; (c) Blasse, G., New compounds with perovskite-like structures. *Journal of Inorganic and Nuclear Chemistry* **1965,** *27* (5), 993-1003.

4. Randall, C.; Newnham, R.; Cross, L., History of the First Ferroelectric Oxide, $BaTiO_3$. *The Electronics Division, http://209.115* **2004,** *31*.

5. (a) Masuda, A., Multi layer ceramic capacitor. Google Patents: 2001; (b) Yokotani, Y.; Kagata, H.; Niwa, H.; Kato, J.; Mihara, T., Multi-layer ceramic capacitor. Google Patents: 1989.

6. (a) Kinoshita, K.; Yamaji, A., Grain-size effects on dielectric properties in barium titanate ceramics. *J. Appl. Phys.* **1976,** *47* (1), 371-373; (b) Bell, A.; Moulson, A.; Cross, L., The effect of grain size on the permittivity of $BaTiO_3$. *Ferroelectrics* **1984,** *54* (1), 147-150; (c) Avrahami, Y.; Tuller, H., Improved electromechanical response in rhombohedral $BaTiO_3$. *Journal of electroceramics* **2004,** *13* (1-3), 463-469; (d) Wada, S.; Suzuki, S.; Noma, T.; Suzuki, T.; Osada, M.; Kakihana, M.; Park, S.-E.; Cross, L. E.; Shrout, T. R., Enhanced piezoelectric property of barium titanate single crystals with engineered domain configurations. *Japanese journal of applied physics* **1999,** *38* (9S), 5505.

7. Dutta, P. K.; Gregg, J. R., Hydrothermal synthesis of tetragonal barium titanate ($BaTiO_3$). *Chem. Mat.* **1992,** *4* (4), 843-846.

8. (a) Eckert, J. O.; Hung-Houston, C. C.; Gersten, B. L.; Lencka, M. M.; Riman, R. E., Kinetics and Mechanisms of Hydrothermal Synthesis of Barium Titanate. *Journal of the*

American Ceramic Society **1996,** *79* (11), 2929-2939; (b) Pinceloup, P.; Courtois, C.; Vicens, J.; Leriche, A.; Thierry, B., Evidence of a dissolution–precipitation mechanism in hydrothermal synthesis of barium titanate powders. *Journal of the European Ceramic Society* **1999,** *19* (6), 973-977; (c) Xu, H.; Gao, L., New evidence of a dissolution–precipitation mechanism in hydrothermal synthesis of barium titanate powders. *Materials Letters* **2002,** *57* (2), 490-494.

9. (a) Shi, E. W.; Xia, C. T.; Zhong, W. Z.; Wang, B. G.; Feng, C. D., Crystallographic properties of hydrothermal barium titanate crystallites. *Journal of the American Ceramic Society* **1997,** *80* (6), 1567-1572; (b) Xu, H.; Gao, L.; Guo, J., Preparation and characterizations of tetragonal barium titanate powders by hydrothermal method. *Journal of the European Ceramic Society* **2002,** *22* (7), 1163-1170.

10. Yang, J.; Zhang, J.; Liang, C.; Wang, M.; Zhao, P.; Liu, M.; Liu, J.; Che, R., Ultrathin $BaTiO_3$ Nanowires with High Aspect Ratio: A Simple One-Step Hydrothermal Synthesis and Their Strong Microwave Absorption. *ACS Applied Materials & Interfaces* **2013,** *5* (15), 7146-7151.

11. (a) Hayashi, Y.; Kimura, T.; Yamaguchi, T., Preparation of rod-shaped BaTiO3 powder. *Journal of materials science* **1986,** *21* (3), 757-762; (b) Saifi, M.; Dubois, B.; Vogel, E.; Thiel, F., Growth of tetragonal $BaTiO_3$ single crystal fibers. *Journal of Materials Research* **1986,** *1* (03), 452-456.

12. (a) Pertsev, N. A.; Petraru, A.; Kohlstedt, H.; Waser, R.; Bdikin, I. K.; Kiselev, D.; Kholkin, A. L., Dynamics of ferroelectric nanodomains in $BaTiO_3$ epitaxial thin films via piezoresponse force microscopy. *Nanotechnology* **2008,** *19* (37), 375703; (b) Zhu, J.; Zheng, L.; Luo, W. B.; Li, Y. R.; Zhang, Y., Microstructural and electrical properties of $BaTiO_3$ epitaxial

films on $SrTiO_3$ substructures with a $LaNiO_3$ conductive layer as a template. *Journal of Physics D: Applied Physics* **2006,** *39* (11), 2438.

13. (a) Yanase, N.; Abe, K.; Fukushima, N.; Kawakubo, T., Thickness dependence of ferroelectricity in heteroepitaxial $BaTiO_3$ thin film capacitors. *Japanese journal of applied physics* **1999,** *38* (9S), 5305; (b) Kim, Y.; Kim, D.; Kim, J.; Chang, Y.; Noh, T.; Kong, J.; Char, K.; Park, Y.; Bu, S.; Yoon, J., Critical thickness of ultrathin ferroelectric $BaTiO_3$ films. *Applied Physics Letters* **2005,** *86* (10), 102907-103100.

14. Ahn, S. H.; Jung, W. W.; Choi, S. K., Size dependence of initial polarization direction in nanosized epitaxial $PbTiO_3$ islands fabricated by hydrothermal epitaxy below Curie temperature. *Applied Physics Letters* **2005,** *86* (17), 172901.

15. Liu, D.; Yan, Y.; Zhou, H., Synthesis of Micron-Scale Platelet BaTiO3. *Journal of the American Ceramic Society* **2007,** *90* (4), 1323-1326.

16. (a) Feng, Q.; Hirasawa, M.; Kajiyoshi, K.; Yanagisawa, K., Hydrothermal soft chemical synthesis and particle morphology control of $BaTiO_3$ in surfactant solutions. *Journal of the American Ceramic Society* **2005,** *88* (6), 1415-1420; (b) Feng, Q.; Hirasawa, M.; Yanagisawa, K., Synthesis of crystal-axis-oriented $BaTiO_3$ and anatase platelike particles by a hydrothermal soft chemical process. *Chem. Mat.* **2001,** *13* (2), 290-296.

17. Yamamoto, T.; Makino, Y., Pressure dependence of ferroelectric properties in $PbZrO_3$-$PbTiO_3$ solid state system under hydrostatic stress. *Japanese journal of applied physics* **1996,** *35* (5S), 3214.

18. Kaneko, S.; Imoto, F., Reactions between PbO and TiO_2 under Hydrothermal Conditions. *Bulletin of the Chemical Society of Japan* **1978,** *51* (6), 1739-1742.

19. Cheng, H.; Ma, J.; Zhao, Z., Hydrothermal Synthesis of PbO-TiO_2 Solid Solution. *Chem. Mat.* **1994,** *6* (7), 1033-1040.

20. Sæterli, R.; Rørvik, P. M.; You, C. C.; Holmestad, R.; Tybell, T.; Grande, T.; van Helvoort, A. T. J.; Einarsrud, M.-A., Polarization control in ferroelectric $PbTiO_3$ nanorods. *J. Appl. Phys.* **2010,** *108* (12), 124320.

21. Yang, Y.; Wang, X.; Zhong, C.; Sun, C.; Li, L., Ferroelectric $PbTiO_3$ nanotube arrays synthesized by hydrothermal method. *Applied Physics Letters* **2008,** *92* (12), 122907.

22. Zhang, X.; Zhao, X.; Lai, C.; Wang, J.; Tang, X.; Dai, J., Synthesis and piezoresponse of highly ordered Pb ($Zr_{0.53}Ti_{0.47}$) O_3 nanowire arrays. *Applied physics letters* **2004,** *85* (18), 4190-4192.

23. Novoselov, K. S.; Geim, A. K.; Morozov, S.; Jiang, D.; Zhang, Y.; Dubonos, S. a.; Grigorieva, I.; Firsov, A., Electric field effect in atomically thin carbon films. *science* **2004,** *306* (5696), 666-669.

24. Jiang, J.-W.; Wang, J.-S.; Li, B., Young's modulus of graphene: a molecular dynamics study. *Phys. Rev. B* **2009,** *80* (11), 113405.

25. Hernandez, Y.; Nicolosi, V.; Lotya, M.; Blighe, F. M.; Sun, Z.; De, S.; McGovern, I.; Holland, B.; Byrne, M.; Gun'Ko, Y. K., High-yield production of graphene by liquid-phase exfoliation of graphite. *Nature nanotechnology* **2008,** *3* (9), 563-568.

26. Varrla, E.; Paton, K. R.; Backes, C.; Harvey, A.; Smith, R. J.; McCauley, J.; Coleman, J. N., Turbulence-assisted shear exfoliation of graphene using household detergent and a kitchen blender. *Nanoscale* **2014,** *6* (20), 11810-11819.

27. (a) Sasaki, T.; Yu, K. M.; Fujiki, Y., PROTONATED PENTATITANATE - PREPARATION, CHARACTERIZATIONS, AND CATION INTERCALATION. *Chem. Mat.*

1992, *4* (4), 894-899; (b) Sasaki, T.; Watanabe, M., Osmotic swelling to exfoliation. Exceptionally high degrees of hydration of a layered titanate. *Journal of the American Chemical Society* **1998,** *120* (19), 4682-4689.

28. Tanaka, T.; Ebina, Y.; Takada, K.; Kurashima, K.; Sasaki, T., Oversized titania nanosheet crystallites derived from flux-grown layered titanate single crystals. *Chem. Mat.* **2003,** *15* (18), 3564-3568.

CHAPTER 5

BARIUM TITANATE SYNTHESIS USING NANOSHEET TITANIA PRECURSORS

Davidson, Matthew. To be submitted to CrystEngComm

Abstract:

Nanoparticles of barium titanate (BTO) were successfully synthesized using nanosheets of $(TBA)_{1.07}Ti_{1.73}O_4$ and $(TBA)_2Ti_4O_9$ as the TiO_2 source. The hydrothermal reactions were done without the addition of strong mineralizers like KOH or NaOH. The size of the particles varied with reaction time and temperature, with an average particle size of 100 nm. Reactions with a melt-flux of $Ba(OH)_2 \cdot 8H_2O$ yielded much smaller BTO particle clusters as well as a significant $BaCO_3$ impurity. Adding $BaCO_3$ directly into the melt-flux mixture surprisingly had an effect on the morphology, with the 1:5 $Ba(OH)_2$: $BaCO_3$ ratio yielding large rectangular shapes. Nanosheets precursors of titania proved to be more reactive than crystalline anatase powders and reacted $Ba(OH)_2$ at much lower temperatures.

Results and Discussion:

Preparation of Ba-TiO gels:

The first step is to remove TBA from $Ti_4O_9^{-2}$ nanosheets using Ba^{2+} treatment; as a result the large sheets crumple into more compact clusters. Looking at the differences by TEM, TBA coated sheets form a film across the whole grid whereas the Ba-TiO gel is more grouped together bunches (Figure 5.1).

The gel is also less ordered than the original sheets. As seen by powder XRD, the precursor sheets

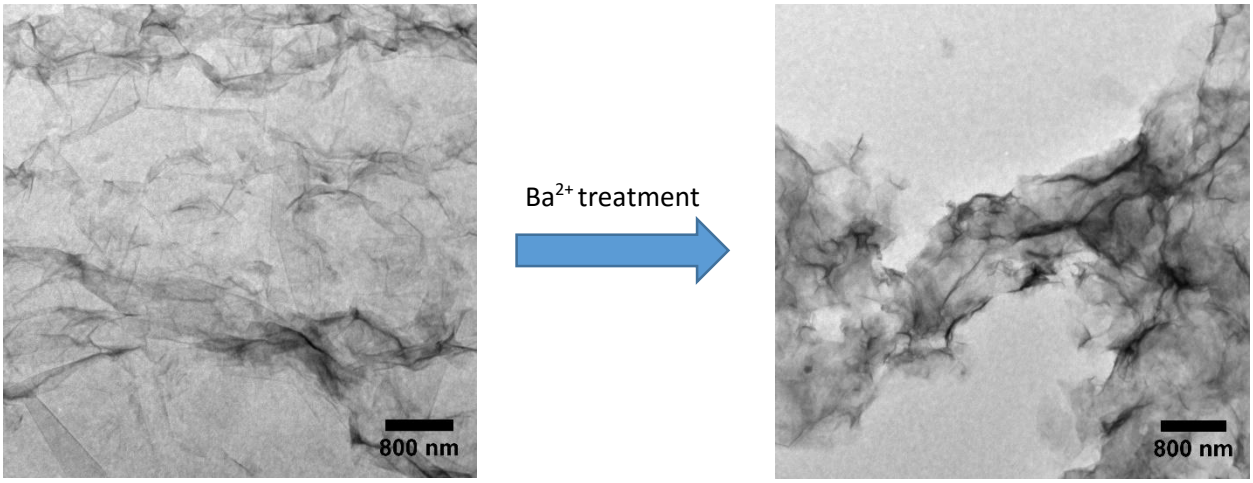

Figure 5.1: TEM images of untreated nanosheets (left) and Ba^{2+} treated nanosheets (right)

show a distinctive (0 0 ℓ) pattern, but after treatment only 1 peak remains along with a large amorphous contribution. This indicates that the long range ordering of the structure is disrupted due to the fact that the crumbled sheets no longer assemble neatly (Figure 5.2). There is also a large decrease in the overall crystallinity as well as a shift to smaller d-spacing. There was no observable difference between different Ba^{2+} salts, with $Ba(OH)_2$ and $Ba(OAc)_2$ giving the same results.

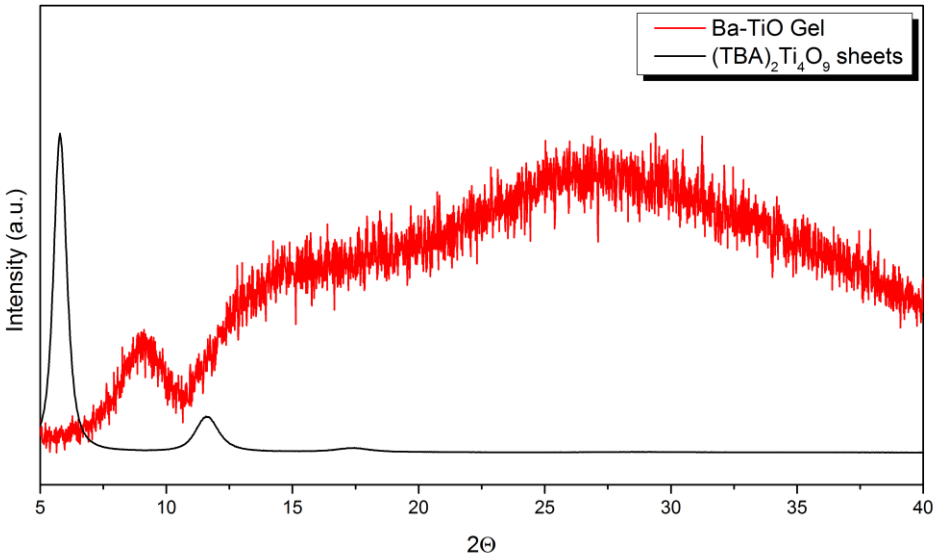

Figure 5.2: PXRD comparison of untreated nanosheets and Ba^{2+} treated nanosheets

Hydrothermal growth of $BaTiO_3$:

$Ba(OH)_2$: TiO_2 ratio	Temperature	Time	Mineralizers	Products
3 : 1	180 °C	3 h	-	Large BTO nanoparticles
3 : 1	120 °C	3 h	-	BTO nanoparticles
3 : 1	100 °C	1 h	-	Ba-TiO gel and BTO growth on the edges
3 : 1	100 °C	3 h	-	Less Ba-TiO gel and more BTO growth
3 : 1	100 °C	6 h	-	Complete conversion to BTO nanoparticles
3 : 1	70 °C	8 h	-	BTO nanoparticles
3 ($Ba(OAc)_2$) : 1	180 °C	3 h	-	Ba-TiO gel, no BTO
3 : 1	180 °C	3 h	NaOH	$Na_2Ti_3O_7$ nanoscrolls
3 : 1	180 °C	3h	KOH	$K_2Ti_6O_{13}$ nanowires/scrolls

The hydrothermal growth of BTO is a well-studied and understood reaction. The major difference here is the choice of precursors. Many other research groups use crystalline anatase

(TiO_2) as the Ti source due to its abundance and pricing. Anatase is a very stable polymorph found in nature. In order to facilitate the reaction between it and Ba, more mineralizer and higher temperatures are required. Hydrothermal reactions reported in literature use higher temperatures (≥ 200 °C) and higher mineralizer molarities (>10 M). While we also take our system up to temperatures as high as 180 °C, we never use mineralizer molarities as high as those seen in typical hydrothermal reactions. This difference is due to the reactivity of the Ba-TiO gel. It has reactivity very similar to reactive Ti precursors like titanium isopropoxide, but is not water sensitive.

The hydrothermal reactions all successfully produced $BaTiO_3$ particles. The exception to this is when no mineralizer was present in the acid digestion vessel but this was only seen in the all $Ba(OAc)_2$ reaction. The reaction proceeded along a dissolution / nucleation mechanism which was previously seen in $BaTiO_3$ reactions. The OH^- ions attack the TiO_2 sheets and form a $Ti(OH)_x^-$ species that is soluble. The titanium hydroxide species is highly reactive with the Ba^{2+} present to form $BaTiO_3$. Any source of OH^- acted like a mineralizer in these hydrothermal reactions including the $Ba(OH)_2$. One of the interesting trends in these reactions was the correlation between temperature, time and mineralizer. The reaction does not appear to be temperature limited and will go at very low temperatures (<70 °C) but more time is needed. As temperature is increased the time required for complete reaction is decreased. This allowed for snapshots of various stages of the reaction to show the growing $BaTiO_3$ morphology and elucidate the role of Ba-TiO. Furthermore the mineralizer enables the reaction, allowing for lower temperature and shorter times.

Using TEM, imaging the growth of $BaTiO_3$ particles can be seen on the surface of the Ba-TiO clusters after 1 h at 100 °C. It is important to note that these particles are not free standing but only exist anchored to the larger Ba-TiO clusters (Figure 5.3). The BTO particles range in size

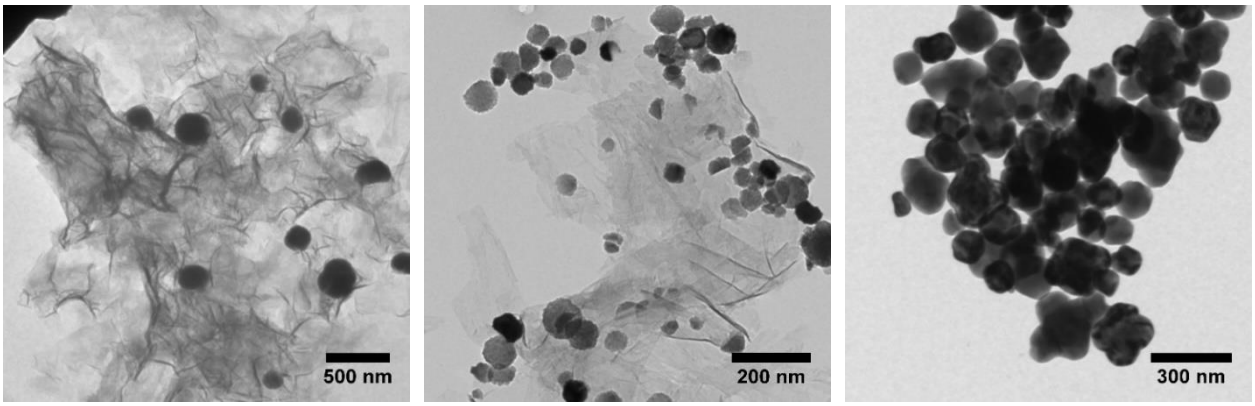

Figure 5.3: TEM as the hydrothermal $BaTiO_3$ reaction progresses.

from 100 – 300 nm and are spherical in morphology. As the reaction progresses, the particles grow in size and begin to square off morphology-wise. They also separate from the clusters to become free standing. Finally, when the reaction moves to completion, the Ba-TiO clusters are completely used up and only BTO particles remain. This pathway was virtually identical for all variable reactions that underwent the hydrothermal reaction. Exceptions were when extreme amounts of KOH or NaOH were used. In these cases the vast abundance of Na^+ and K^+ favors the formation of $Na_2Ti_3O_7$ scrolls and $K_2Ti_6O_{13}$ wires (Figure 5.4).

Unfortunately the morphology of the nanosheet precursor does not seem to influence the morphology of the product. There appears to be no templating effect in these hydrothermal reactions. When the sheets are treated with Ba^{2+} the TBA is displaced and the sheets lose their long range ordering and crumple. The TiO_2 then dissolves and reacts with the available Ba^{2+} to form BTO. Even though the BTO begins growth on the surface of the Ba-TiO, it does not template. The particles continue to develop until the Ba-TiO is used up.

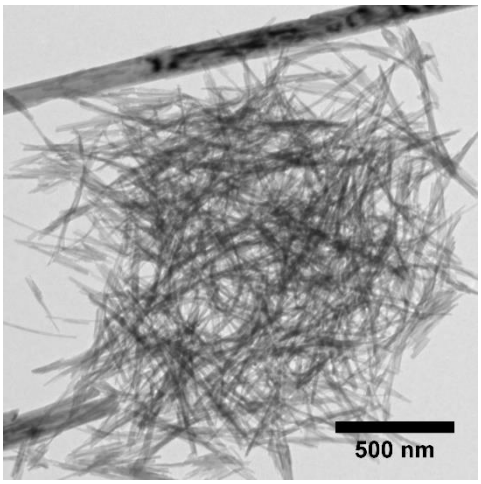

Figure 5.4: TEM of $K_2Ti_6O_{13}$ nanowires/scrolls

Melt-flux growth of $BaTiO_3$:

Ba-TiO_2 : $BaCO_3$ ratio	Temp 1	Time 1	Temp 2	Time 2	Products
-	100 °C	2 h	180 °C	1 h	BTO platelets
-	100 °C	3 h	180 °C	3 h	BTO nanoparticles
1 : 0.5	100 °C	3 h	180 °C	1 h	BTO nanoparticles
1 : 1	100 °C	3 h	180 °C	1 h	BTO nanoparticles
1 : 2	100 °C	3 h	180 °C	1 h	BTO nanoparticles with a 2D morphology
1 : 5	100 °C	3 h	180 °C	1 h	BTO nanoparticles that are rectangular with right angle edges

The melt-flux reaction relies on the low melting salt $Ba(OH)_2 \cdot 8H_2O$. (mp 78 °C). The overall goal of the melt-flux synthesis is to eliminate the use of water as a solvent and therefore eliminate the dissolution / nucleation mechanism. The reactions are still carried out inside acid-digestion vessels in order to maintain hydration of the salt. Without a pressurized vessel the salt loses hydration and undergoes carbonation into $BaCO_3$.

The melt-flux system successfully produces BTO but similar to the hydrothermal reactions, it produced BTO nanoparticles. However, the size and morphology of the particles were different from those produced hydrothermally. The melt-flux reaction has a two stage heat cycle. The first stage sits at 100 °C for three hours. This ensures the entire stock of $Ba(OH)_2$ is molten and also allows for the dry Ba-TiO to disperse within the flux. The vessel is then moved to 180 °C for 1 hour to drive the reaction forward. Similar to the hydrothermal results, extended durations at lower

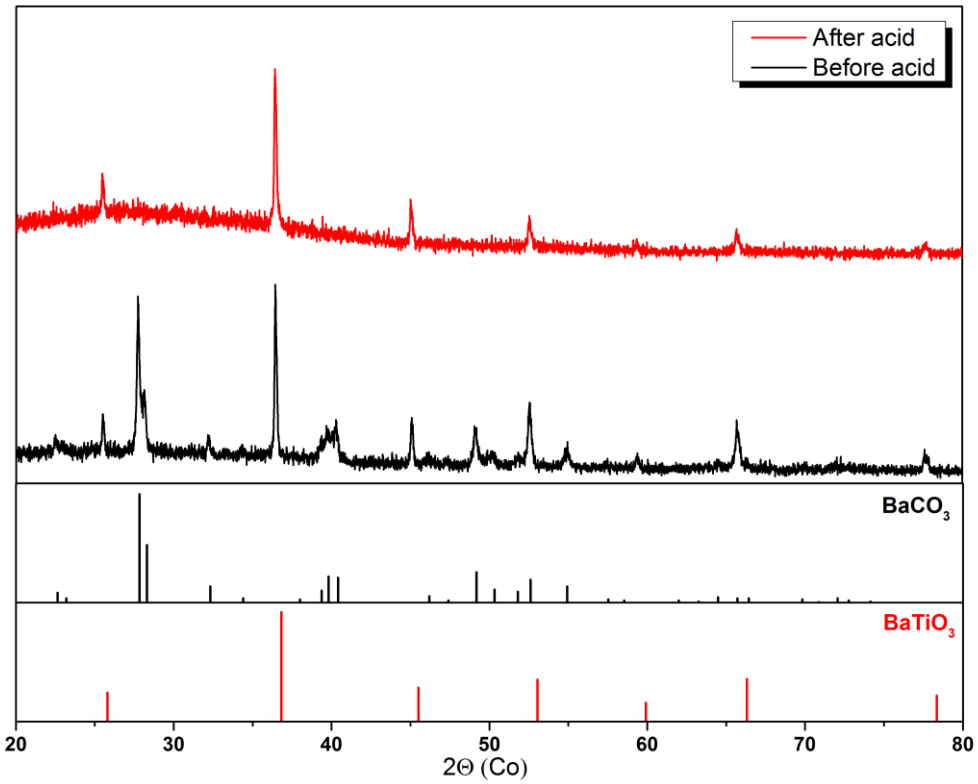

Figure 5.5: PXRD of the product after the melt-flux reaction (bottom) and that same product after acid-washing (top). The drop lines show the expected patterns for $BaCO_3$ and $BaTiO_3$

temperatures will also yield BTO but a minimum temperature of 100 °C is required to ensure complete molten flux. The $Ba(OH)_2$ salt forms a layer of $BaCO_3$ on its surface when it is exposed to air. When the salt becomes molten, it absorbs more CO_2 and forms $BaCO_3$ faster. This is evidenced by the fact that the melt-flux will carbonize completely without a sealed vessel. The melt-flux reactions require a stronger acid treatment to completely remove all the $BaCO_3$. The difference between acid treated and untreated samples is seen via XRD (Figure 5.5).

The end products of the melt-flux synthesis are BTO particles. The particles are grown on the surface of the 2D sheets but unlike the hydrothermal synthesis these particles are not well separated. The outmost layers of the Ba-TiO are converting to BTO but they are still anchored to an unreacted core (Figure 5.6a). These platelets look polycrystalline but actually give a distorted single crystal SAED(Figure 5.6b). This pattern is indexed to $BaTiO_3$ down the c-axis indicating

that there is a templating effect in this reaction. These platelet/particles are diverse in size ranging from 500 nm to 2 µm in length and width. At longer reaction times the platelets are completely destroyed leaving behind only clusters of particles (Figure 5.6c). These give a characteristic polycrystalline SAED pattern that is indexed to BTO (Figure 5.6d). These particles are smaller than the platelets with lateral dimensions < 100 nm.

The melt-flux reaction produces a significant amount of $BaCO_3$ impurity. Some of this is happening in-situ while some of the carbonate is form during sample extraction. The $BaCO_3$ formed could have an effect on the morphology of the end product. To test this idea, different

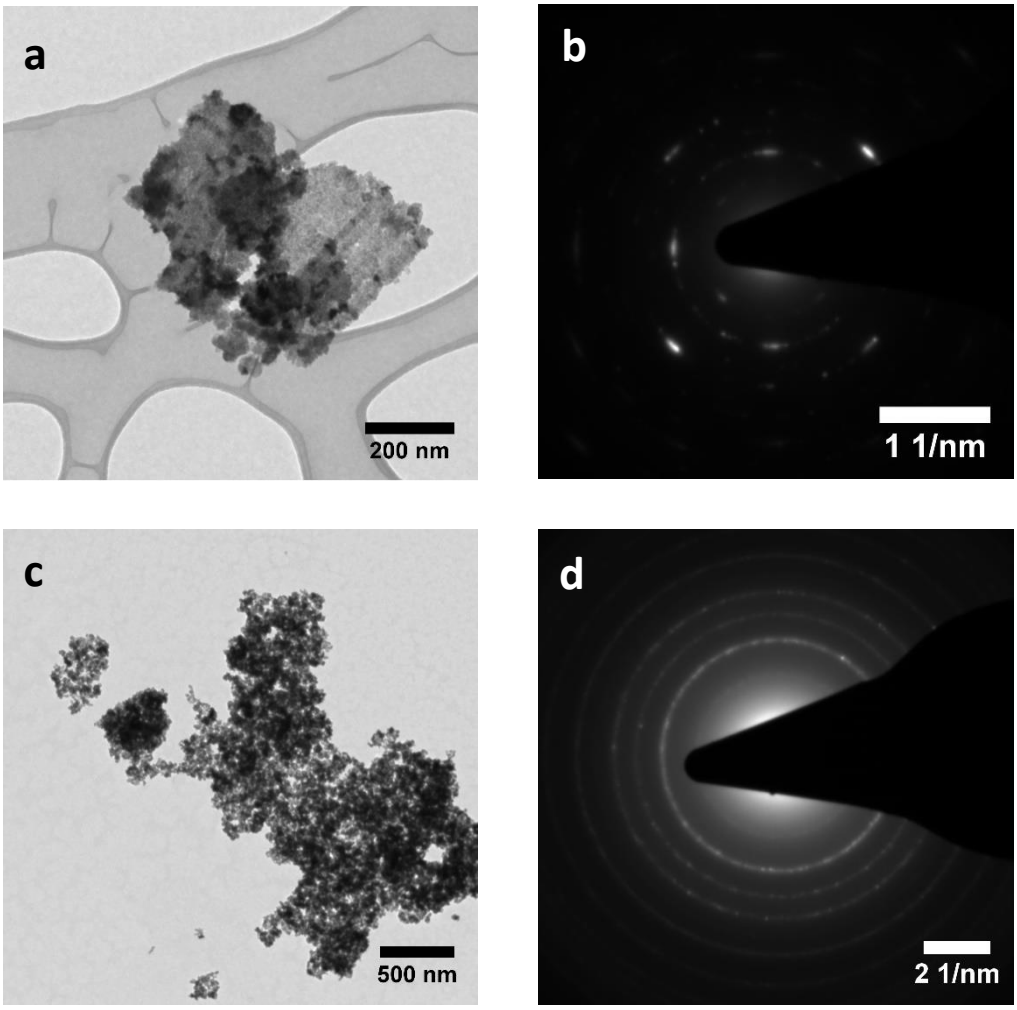

Figure 5.6: a) TEM images of the reacted Ba-TiO gel showing the damaged edges, **b)** SAED of the platelets showing a pseudo single crystal pattern, **c)** TEM of clusters of BTO particles, **d)** SAED of the clusters showing a polycrystalline pattern.

molar quantities of nano $BaCO_3$ were added to the Ba-TiO / $Ba(OH)_2$ mixture. This addition elicits a change in morphology of the particles produced. 1:0.5 Ba-TiO-$BaCO_3$ shows very little change but as the $BaCO_3$ is increased to 1:1 and then 1:2 a noticeable change is seen. The smaller particles become larger as the $BaCO_3$ is increased (Figure 5.7a-c). At 1:5 the product undergoes a radical morphology shift. The small particles are replaced by larger rods that can be several hundreds of nanometers long. The rods are rectangular in shape with rounded corners (Figure 5.7d).

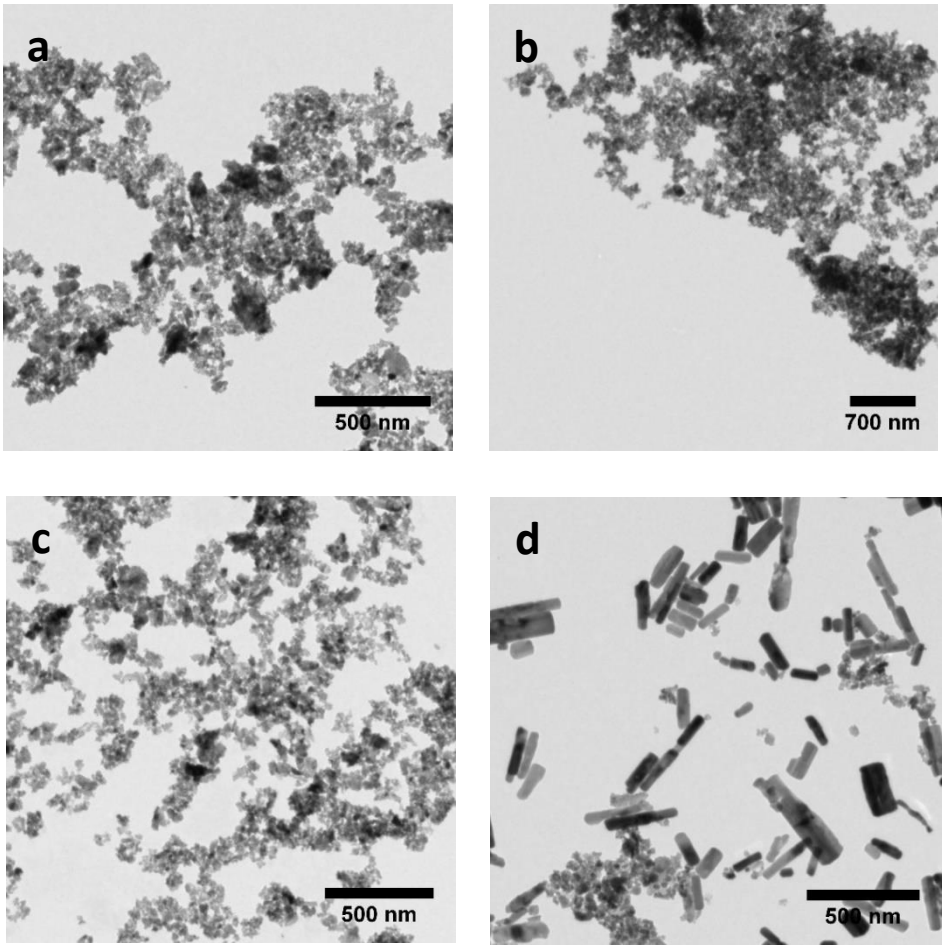

Figure 5.7: TEM images of BTO melt-flux reactions with increasing amounts of $BaCO_3$ added **a)** 1:0.5, **b)** 1:1, **c)** 1:2 **d)** 1:5

Conclusions:

Using $(TBA)_{1.07}Ti_{1.73}O_4$ and $(TBA)_2Ti_4O_9$ nanosheets did not have a significant effect on the morphology of the final BTO product. However, the nanosheets are a more reactive precursor than commercially available anatase powders, bulk or nano. The dissolution / nucleation mechanism is the primary pathway to the formation of BTO in both the hydrothermal and melt-flux reactions. The stability of $BaCO_3$ causes it to be a constant by-product of the reactions that requires an additional acid cleaning step. With the melf-flux reaction, the addition of $BaCO_3$ alters the morphology of the results BTO drastically. At high molar ratios the addition of $BaCO_3$ forms large rectangular BTO platelets instead of nanoparticle clusters.

Experimental:

Preparation of $Ti_{1.73}O_4$ nanosheets:

The synthesis of these nanosheets is based off previously reported literature.[1] TiO_2 (anatase), K_2CO_3, Li_2CO_3 and MoO_3 are ground together in a 1.73:1.67:0.13:1.27 respective molar ratio. The typical scale of this reaction used 5 g of TiO_2 which produces a total mixture of 20 g. The powders are ground together for 15 minutes to ensure complete homogeneity. The powder is placed into a Pt crucible and ramped up to 1200 °C at 10 °C/min and held there for 10 h. It is cooled slowly at 4 °C/h down to 900 °C and then is allowed to cool down to room temperature. The large $K_{0.8}Ti_{1.73}Li_{0.27}O_4$ crystals are separated from the K_2MoO_4 flux using excess hot water.

The $K_{0.8}Ti_{1.73}Li_{0.27}O_4$ crystals are shaken in 500 mL of 1M HCl for 5 days. The mixture is filtered and a fresh 500 mL of 1M HCl is added each day. The now protonated crystals ($H_{1.07}Ti_{1.73}O_4$) are shaken in 500 mL of 0.5 M tetrabutylammonium hydroxide (TBAOH) for 7

days. The mixture is centrifuged at 10,000 RPM and the supernatant discarded. The precipitate is suspended into 1 L of water.

Preparation of $Ti_4O_9^{2-}$ nanosheets:

The synthesis of these nanosheets is based off previously reported literature.[2] TiO_2 (anatase) and K_2CO_3 are ground together in a 1:3 molar ratio respectively. The typical scale of the reaction was 5 g of TiO_2. The mixture is placed in a Pt crucible and reacted at 950 °C for 10 h. The mixture was shaken in 500 mL of 1 M HCl for 5 days. The mixture is filtered and a fresh 500 mL of 1M HCl is added each day. The now protonated crystals ($H_2Ti_4O_9$) are shaken in 500 mL of 0.5 M tetrabutylammonium hydroxide (TBAOH) for 7 days. The mixture is centrifuged at 10,000 RPM and the supernatant discarded. The precipitate is suspended into 1 L of water.

Preparation of Ba-TiO gels:

$(TBA)_{1.07}Ti_{1.73}O_4$ nanosheets and $(TBA)_2Ti_4O_9$ nanosheets were prepared by already established methods.[1-2] The suspensions of nanosheets are mixed with excess $Ba(OH)_2$ or $Ba(OAc)_2$ and centrifuged at 10,000 RPM to remove the TBA. The resulting gel-like substance is then used as the precursor is a series of hydrothermal and melt-flux reactions.

Hydrothermal formation of $BaTiO_3$:

The Ba-TiO gel is suspended in 20 mL of water. Various amounts of $Ba(OH)_2$, NaOH or KOH are added and the mixture is sealed inside a 45 mL acid digestion vessel. The reactions are heated to 100 °C, 120 °C or 180 °C for 1 h, 2 h or 3h. The vessel is allowed to cool and its contents poured out and centrifuged at 10,000 RPM. The supernatant is discarded and the precipitate is

suspended in 20 mL again. 1 mL glacial acetic acid is mixed with the precipitate to remove $BaCO_3$ impurities and the suspension is filtered through a 100 µm membrane filter.

Melt-flux synthesis of $BaTiO_3$:

The Ba-TiO gels are vacuum dried and ground into a powder. 100 mg of dried Ba-TiO is mixed with 2 g $Ba(OH)_2 \cdot 8H_2O$ and ground together for 15 minutes. To these mixed powder various amounts of $BaCO_3$ (>100 nm $BaCO_3$ nanorods, Solvays) are added. 0 – 1 g of $BaCO_3$ are added and the powder is ground again for 15 minutes. The mixed powder is sealed in an acid digestion vessel and reacted at 100 °C for 3 h and then moved up to 180 °C for 1 h. The acid digestion vessel is allowed to cool and the product is extracted using 30 mL of hot water. The resulting suspension is centrifuged at 10,000 RPM and the supernatant discarded. The product is suspended in 20 mL of water and 1 mL of glacial acetic acid is added to remove $BaCO_3$. The mixture is filtered through a 100 µm membrane filter.

1. Tanaka, T.; Ebina, Y.; Takada, K.; Kurashima, K.; Sasaki, T., Oversized titania nanosheet crystallites derived from flux-grown layered titanate single crystals. *Chem. Mat.* **2003,** *15* (18), 3564-3568.

2. Allen, M. R.; Thibert, A.; Sabio, E. M.; Browning, N. D.; Larsen, D. S.; Osterloh, F. E., Evolution of Physical and Photocatalytic Properties in the Layered Titanates $A_2Ti_4O_9$(A = K, H) and in Nanosheets Derived by Chemical Exfoliation†. *Chem. Mat.* **2010,** *22* (3), 1220-1228.

CHAPTER 6

LEAD TITANATE SYNTHESIS USING NANOSHEET TITANIA PRECURSORS

Davidson, Matthew. To be submitted to CrystEngComm

Abstract:

Nanoplatelets of $PbTiO_3$ were synthesized with a hydrothermal reaction using a 2D nano precursor. $(TBA)_{1.07}Ti_{1.73}O_4$ nanosheets and $(TBA)_2Ti_4O_9$ nanosheets have a templating effect on the $PbTiO_3$ produced in the reaction through a dissolution / nucleation mechanism. Large platelets of $PbTi_{0.8}O_{2.6}$ are an intermediate in the reaction on which the $PbTiO_3$ platelets form. The reactions are accomplished without the need for harsh mineralizers. Solvothermal reactions using ethylene glycol as a solvent produced layered hexagons of $Pb_5O(CO_3)_3(OH)_2$. The layered hexagons then convert to a layered cross morphology that is a Pb-TiO-CO_3 species. These crosses then undergoes a dissolution / nucleation into $PbTiO_3$. Again, with the solvothermal reactions, a templating effect was seen with the use of nanosheets of TiO_2.

Results and discussion:

Hydrothermal reactions of Pb-TiO:

The formation of the "Pb-TiO" gels are similar to the formation of the "Ba-TiO" gels. The addition of Pb^{2+} ions causes the colloidal suspension of TiO_2 sheets to flocculate and precipitate out. One major difference is that there is no soluble $Ba(OH)_2$ analog in the lead system. Lead hydroxide is not a stable compound and readily converts to lead carbonate basic or lead oxide. Despite its relatively poor solubility (0.017 g/L) PbO is able to flocculate TBA coated TiO_2 nanosheets. Whether this is through the release of Pb^{2+} ions or the attractions of the negative TiO_2 to the leads is not completely understood. PbO is an orange powder and when used to form the "Pb-TiO" gels the resulting gels are also orange. If left in solution for extended periods of time the orange color will slowly fade into white indicating some chemical reaction occurring.

Below is a table summary of the hydrothermal work done on the "Pb-TiO" gels. There is no major difference between the use of $(TBA)_{1.07}Ti_{1.73}O_4$ nanosheets and $(TBA)_2Ti_4O_9$ nanosheets so they are not included as a variable.

PbO : TiO_2 ratio	Temperature	Time	Additives	Products
2.5 : 1	180 °C	3 h	-	Rectangles of $PbTi_{0.8}O_{2.6}$ with platelets of $PbTiO_3$ on edges
2.5 : 1	220 °C	3 h	-	Nanoplatelets of $PbTiO_3$
2.5 : 1	105 °C	18 h	-	Rectangles of $PbTi_{0.8}O_{2.6}$
2.5 : 1	180 °C	8 h	-	Nanoplatelets of $PbTiO_3$
0.8 : 1	180 °C	3 h	-	Hexagons of $Pb_5O(CO_3)_3(OH)_2$ and unreacted Pb-TiO gel
2.5 : 1	180 °C	3 h	0.5 M KOH	Rectangles of $PbTi_{0.8}O_{2.6}$ with cubes of $PbTiO_3$ on edges
2.5 : 1	180 °C	18 h	Excess KOH	$K_2Ti_6O_{13}$ nanowires
2.5 : 1	180 °C	3 h	0.5 M NH_4OH	Nanoplatelets of $PbTiO_3$ and unreacted Pb-TiO
2.5 : 1	180 °C	18 h	0.5 M NH_4OH	Nanoplatelets of $PbTiO_3$

Looking back at the hydrothermal barium work, all the reactions produced BTO in some quantity. In the lead system this is not the case. Many of the lead reactions produced a mixture of $PbTi_{0.8}O_{2.6}$ and $PbTiO_3$ (PTO) and required extended time or increased heat to produce only PTO. Without the addition of mineralizer the reaction did not proceed to completion in 3 h at 180 °C. PbO does not release OH^-, and does not readily form the $Ti(OH)_x$ necessary for the dissolution / nucleation mechanism. Therefore, lower temperature and shorter reactions did not form $PbTiO_3$ and were left with unreacted PbO. This is not to say that the $Ti(OH)_x$ species will never form without mineralizers present, but it requires significantly longer reaction times to achieve similar results to those with mineralizers. Extended reaction times (18 h) at lower temperatures (105 °C) produced $PbTi_{0.8}O_{2.6}$ shown in PXRD (Figure 6.1). This is a lead rich structure, and alternatively can be expressed as $PbO{\cdot}(PbTiO_3)_4$. It is a known intermediate in the hydrothermal growth of $PbTiO_3$.[1] In the experimental data the peaks at 21.09° and 43.26° are larger than expected looking at the known pattern. These peaks are the (001) and (002) respectively. This indicates that the $PbTi_{0.8}O_{2.6}$ that is being produced has larger layered planes and some two-dimensionality. $PbTi_{0.8}O_{2.6}$ has the crystal parameters a,b = 3.911 Å and c = 4.831 Å. These are similar to $PbTiO_3$ (a,b = 3.899 Å c = 4.1532 Å) but the lead rich structure has a significantly increased c axis.[1]

At 180 °C the reaction produces $PbTiO_3$. At 3 h, large platelets with rectangular morphology have grown. Interesting there is additional growth on the edge of the larger platelets. These particles have rectangular morphology and are templated on the larger platelets (Figure 6.2). Interesting, the center of the thinner platelets is being dissolved as the new particles grow on the

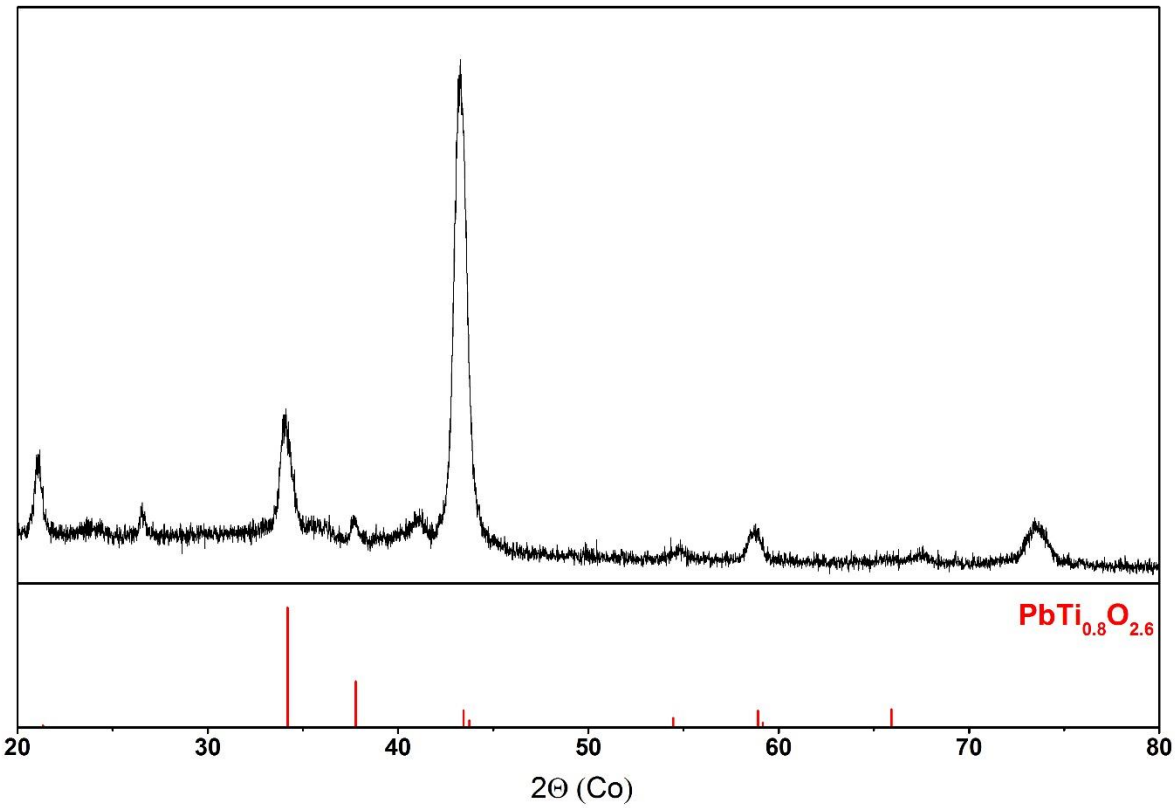

Figure 6.2: PXRD of $PbTi_{0.8}O_{2.6}$ produced from hydrothermal reaction at 105 °C for 18 h

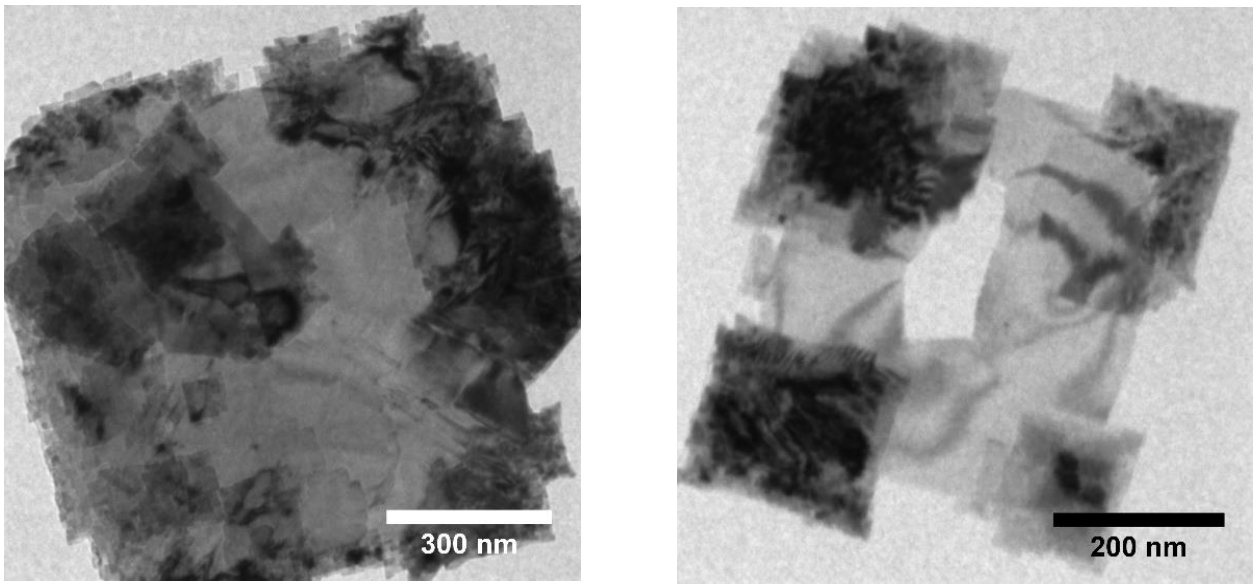

Figure 6.1: TEM of the thick platelets with secondary growth on their edges

corners. A similar dissolution / nucleation mechanism has been seen before in the growth of $PbTiO_3$ particles hydrothermally.[2] At 180 °C the dissolution / nucleation proceeds to completion and only the $PbTiO_3$ particles are left (Figure 6.3). These particles take on the 2D morphology of the $PbTi_{0.8}O_{2.6}$ platelets. This is seen in the PXRD that shows several asymmetric peaks such as the (0 0 1) at 24.85°. This is a different outcome from that seen in the bulk reaction, i.e., instead of a polycrystalline ring of $PbTiO_3$ we are left with smaller platelets. Hydrothermal reactions of PTO typically produce three-dimensional cube structures with micron dimensions.[3] The difference between these results indicates that there are templating effects caused by 2D nanomaterial precursors.

All of these reactions used an excess of PbO (0.0600 g, 2.5:1 $PbO:TiO_2$). When the PbO amount is lowered to 0.0250 g the $PbTi_{0.8}O_{2.6}$ never forms and large hexagonal structures are seen (Figure 6.4a). These hexagons are large 2D structures that are over 8 μm in lateral dimensions. SAED revealed a crystalline structure that matches a lead carbonate basic called plumbonacrite [$Pb_5O(CO_3)_3(OH)$] (Figure 6.4b).

The addition of mineralizer changes the morphology of the products. Adding 100 μL of 10 M KOH causes the $PbTiO_3$ to ripen and lose the platelet structure. They grow thicker on the edges of the rectangular platelets (Figure 6.5a). The mineralizer has the expected behavior of accelerating the dissolution / nucleation mechanism. It reduces the templating effect and produces cubes of PTO instead of platelets. As the amount of KOH is increased, the cubes becomes the dominant morphology and the rectangular platelets are no longer seen. There is an upper limit of useful KOH concentration because the formation of $K_2Ti_6O_{13}$ wires is a problem at higher concentrations. NH_4OH was used to increase the pH without providing a secondary reaction by-product, and it

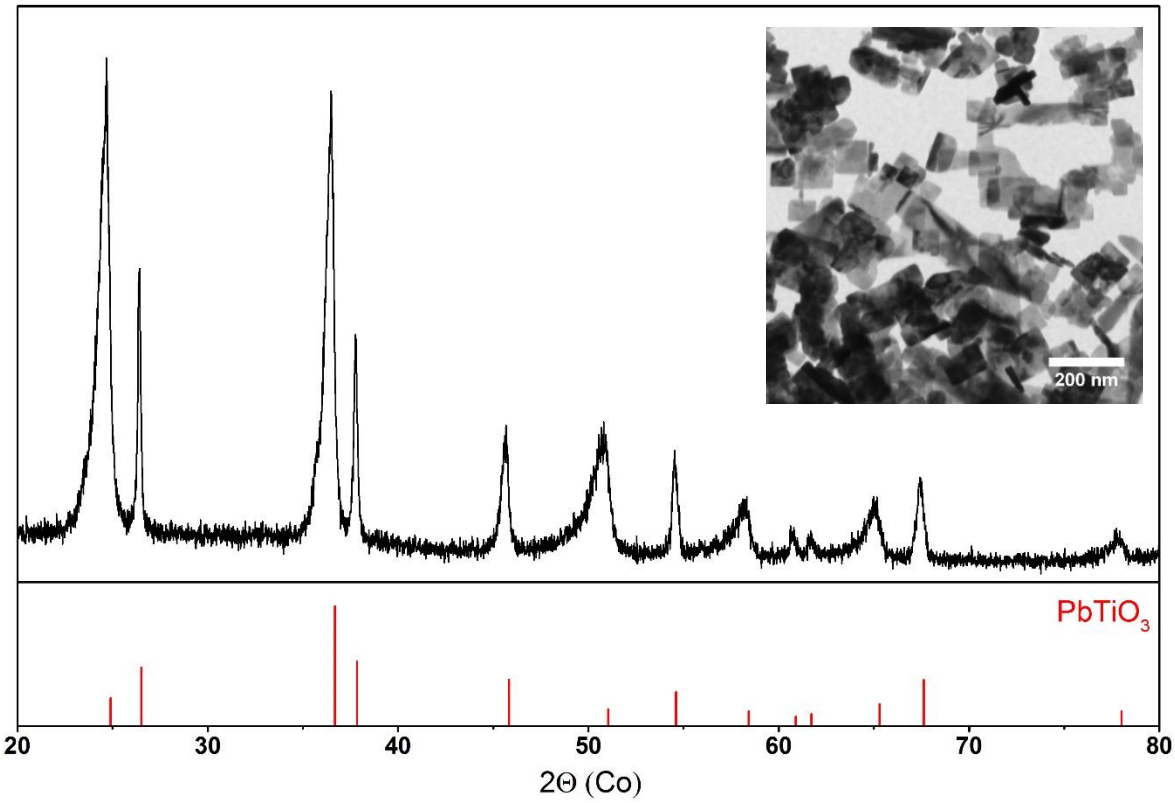

Figure 6.4: PXRD of the PTO platelets shows peak asymmetry and increased intensity of the (001) and (002) peaks. Inset shows TEM of the PTO platelets produced from extended 180 °C

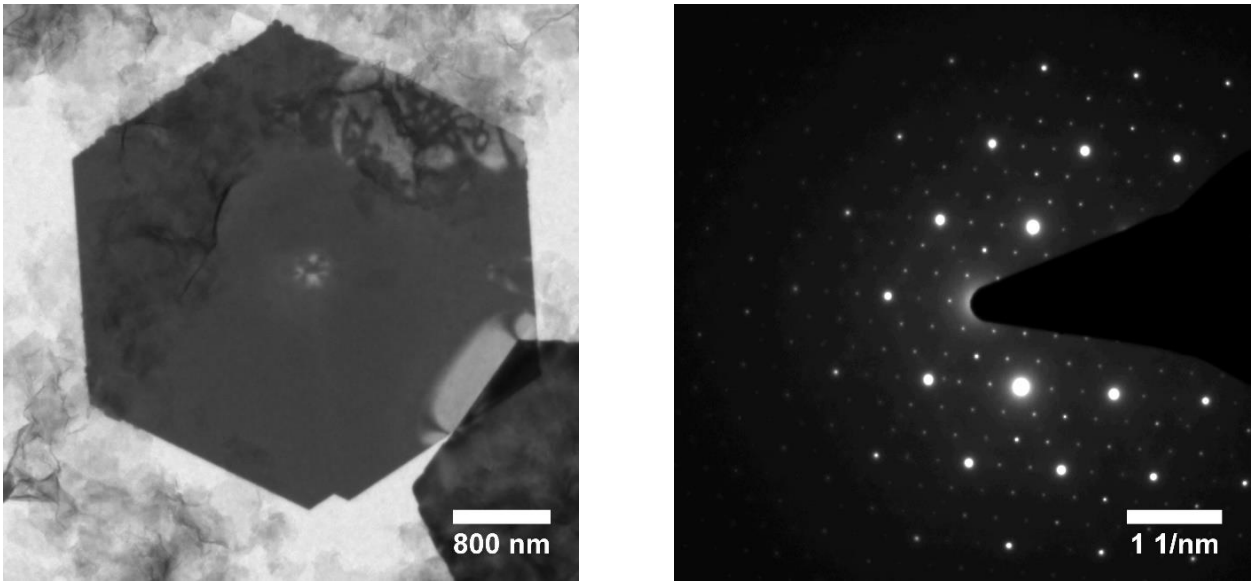

Figure 6.3: a) TEM of the plumbonacrite hexagons with "Pb-TiO" gel in the background b) SAED of the hexagons indexed to plumbonacrite.

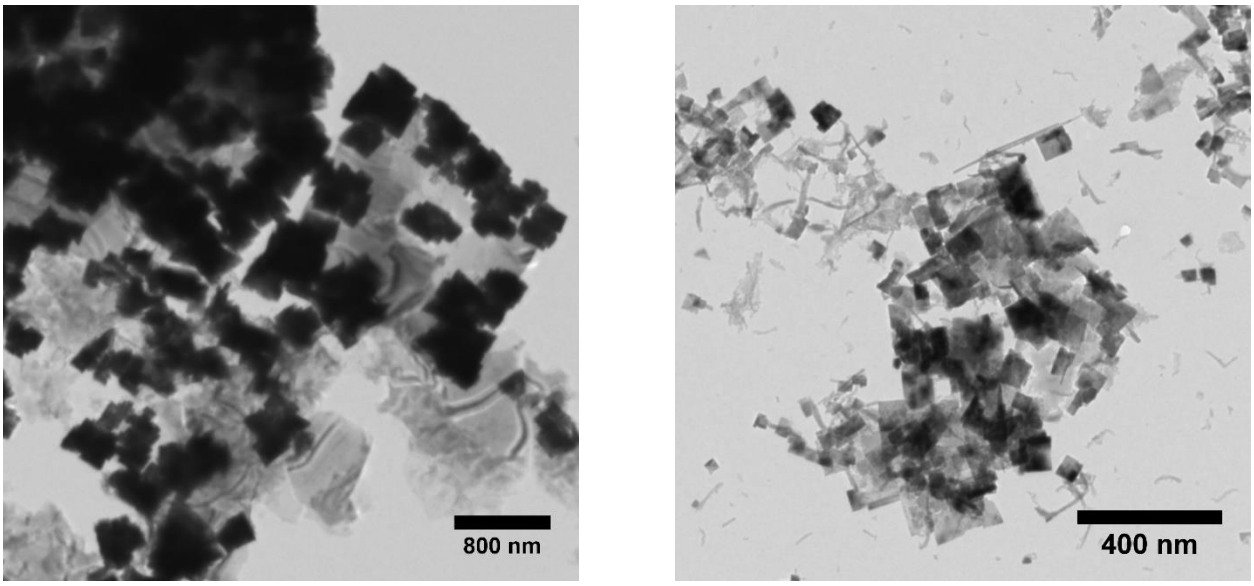

Figure 6.5: a) TEM showing the cubic growth of PTO on the edges of the $PbTi_{0.8}O_{2.6}$ b) TEM of the PTO platelets formed from the dissolution / nucleation reaction with NH_4OH.

also is not as strong of a mineralizer because it is a weak base. The addition of NH_4OH again favored the dissolution / nucleation mechanism, and formed small $PbTiO_3$ platelets (Figure 6.5b).

Solvothermal reactions of Pb-TiO:

Ethylene glycol has a boiling point of 197.3 °C, so in these reactions pressure is not a factor in the product formation. Also, due to the reduced polarity of the solvent the mineralizer effect is reduced as well. However, there is additional concern over the stability of the ethylene glycol as a solvent. At 180 °C the ethylene glycol goes from clear to brown, showing significant solvent

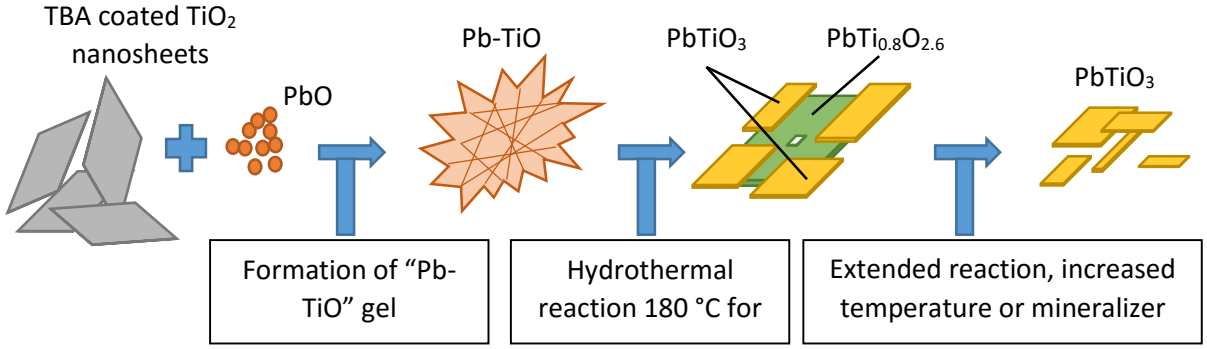

Figure 6.6: Schematic of how the hydrothermal growth mechanism in the system with TiO_2 nanosheets.

PbO : TiO_2 ratio	Temperature	Time	Products
2.5 : 1	180 °C	3 h	Stacked crosses, large hexagons, and unreacted Pb-TiO gel
2.5 : 1	60 °C	3 h	Pb-TiO gel with irregular growths on edges
2.5 : 1	105 °C	3 h	Hexagons of plumbonacrite with Pb-TiO gel
2.5 : 1	120 °C	8 h	Stacked crosses start forming with hexagons and Pb-TiO gel
2.5 ($Pb(NO_3)_2$) : 1	180 ° C	3 h	Pb-TiO gel and single crystal needles

degradation. This is likely due to an oxidation reaction between the ethylene glycol and the reagents.

The solvothermal reactions gave a different product from the hydrothermal reactions. There were three major morphologies seen in the 180 °C for 3 h reaction: stacked crosses, large hexagons, and randomly shaped small particles (Figure 6.7a,b). The hexagons were seen in the low PbO hydrothermal reactions before and confirmed by SAED to also be $Pb_5O(CO_3)_3(OH)_2$. This indicates that enough CO_2 is present in the vessel to form the carbonate either from the atmosphere or from the degradation of the solvent. The stacked crosses are a new morphology and have a series of 90° angles. They have large lateral dimensions over 1 µm in width and the individual pieces of the cross can be 500 nm wide. The other interesting feature of the cross is the apparent stacking of different cross layers. Multiple crosses are seen in TEM that indicates that it is a layered structure but the layers are not the same size creating a mismatch. The center of the cross is lined up between the layers but the arms of the cross vary is width and length. This variance creates a stepped morphology in many of the stacked crosses.

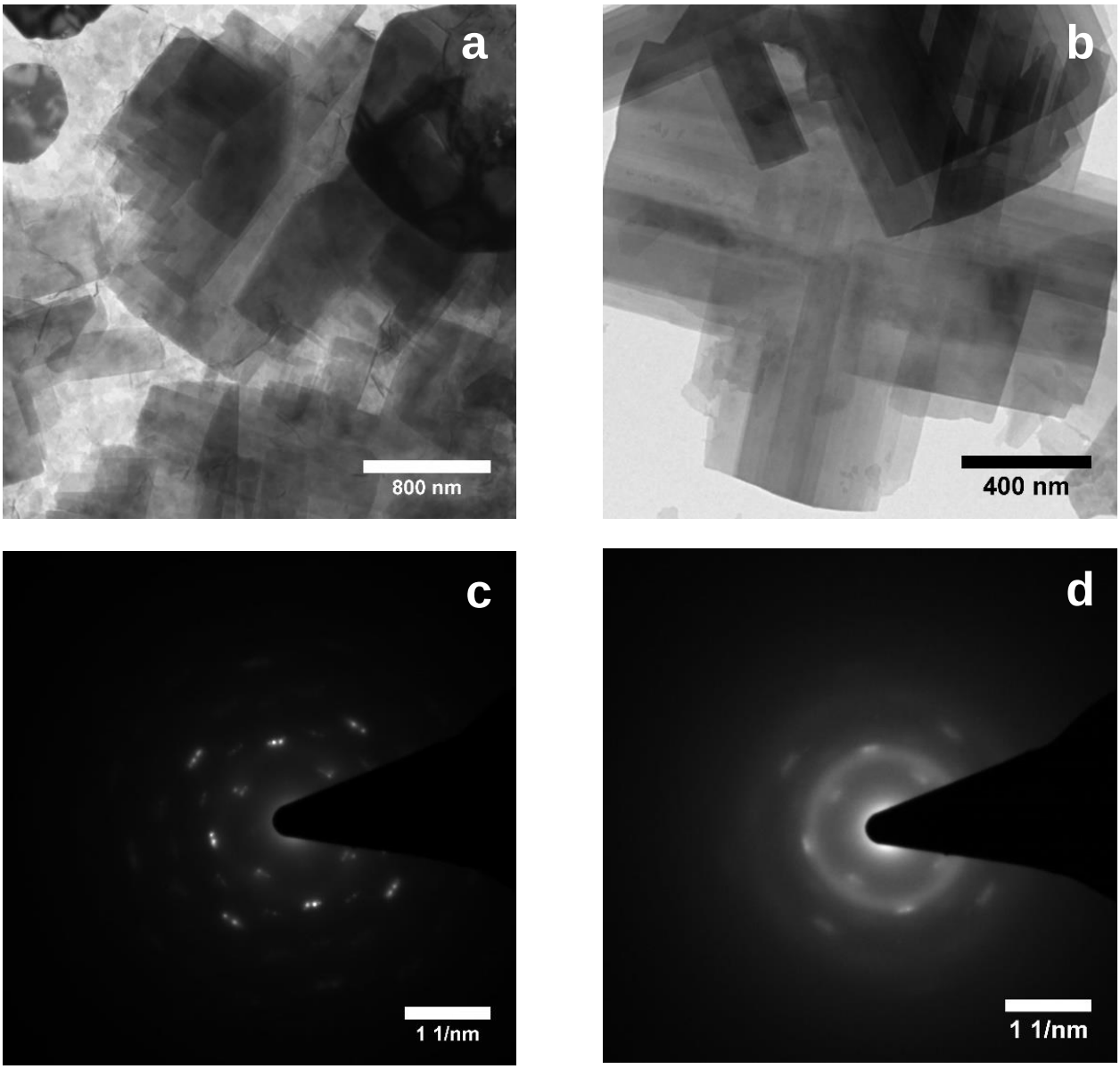

Figure 6.7: a) TEM image showing the heterogeneous product consisting of hexagons, layered crosses and Pb-TiO gel b) TEM images showing off the layeres in the cross structure c) SAED showing a perovskite-like pattern d) SAED showing the beam sensitivity with the loss of the clear pattern.

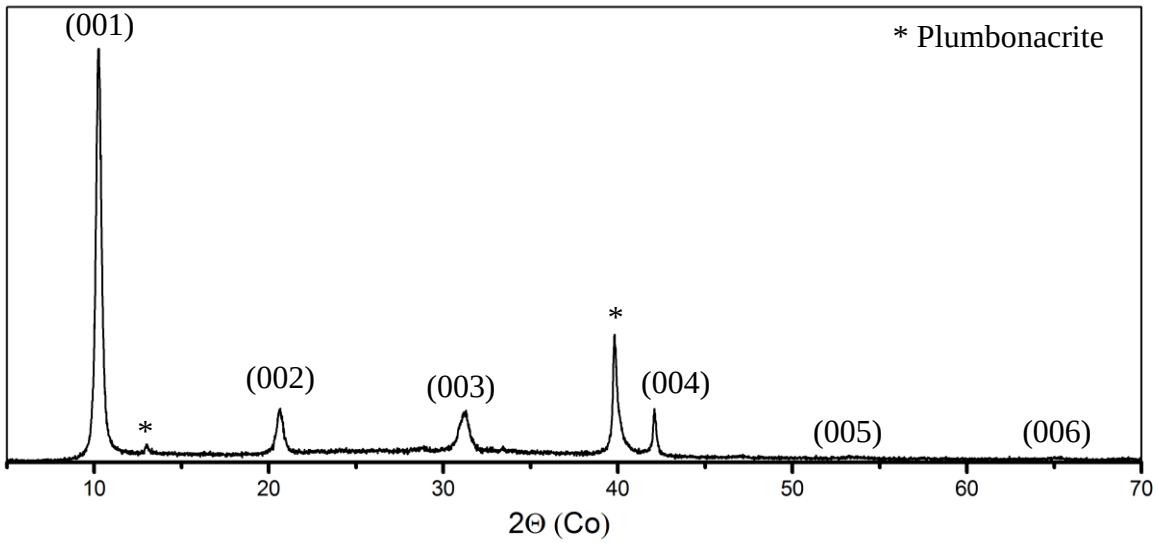

Figure 6.8: PXRD of the stacked crosses shows a layered pattern seen up to (006) as well as peaks associated with plumbonacrite.

The SAED of the crosses shows a perovskite-like pattern but could not be indexed to either $PbTiO_3$ or $PbTi_{0.8}O_{2.6}$. When the diffraction beam was left focused on an area, there was a marked decreased in crystallinity of the sample (Fig 6.7c,d). When the sample was dropcast for PXRD it gave a layered pattern. A clear (0 0 *l*) pattern is seen up to (0 0 6) (Figure 6.8). There is a second species in the PXRD with peaks at 13°, 40° and 42° which is attributed to the plumbonacrite. Centrifuging the sample at 500 RPM for 5 min and a PXRD of the supernatant causes those peaks to disappear.

When the reaction is extended to 18 h there is another shift in the morphology of the products. The stacked crosses develop holes in their centers and also begin to disorder from one layer to the next (Figure 6.9). The inside out dissolution mechanism was seen before in $PbTiO_3$ hydrothermal growth.[2] There is a noticeable softening of the edges of the crosses. Additionally there are no hexagons present in the sample and the irregular small particles have been converted into irregular $PbTiO_3$ particles.

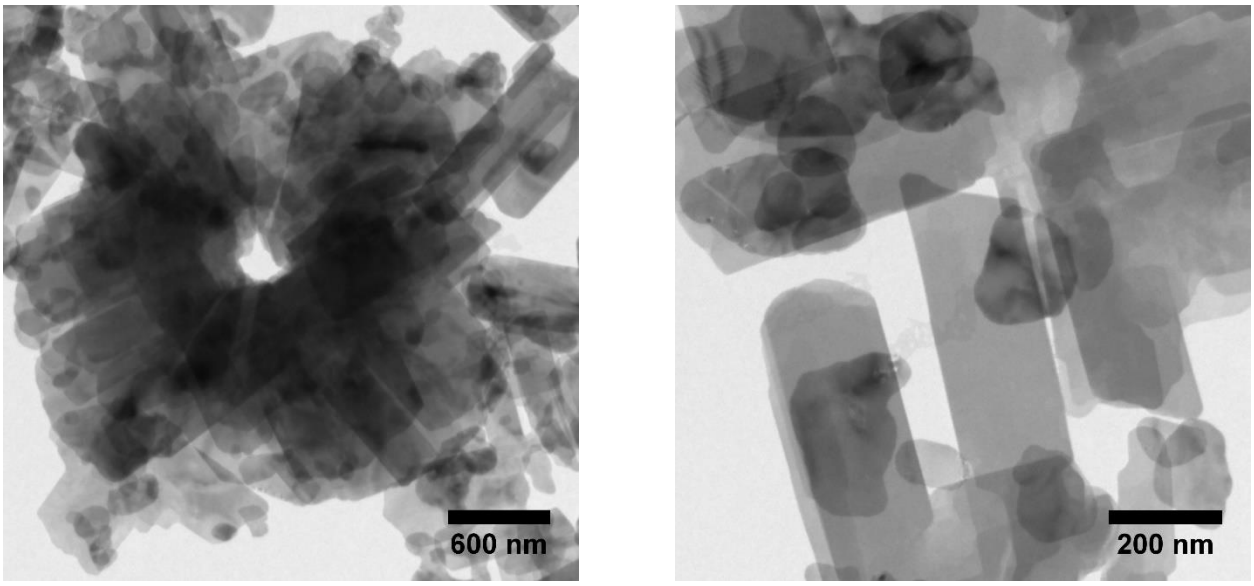

Figure 6.9: TEM showing the stacked crosses dissolution with the vacancy at the center of the structure (left). TEM showing the rounded edges of the crosses (right).

The original stacked crosses displayed beam sensitivity when probed via SAED. This property was explored further with HRTEM. When the sample was analyzed with electron energy loss spectroscopy (EELS) it showed a significant carbon presence (Figure 6.10). HRTEM on the stacked crosses proved to be an insurmountable challenge because as the beam focuses on a region that spot vaporized (Figure 6.11a). Looking at the stacked crosses with dark field imaging showed an erratic distribution of lead in the sample as noted with the bright lines (Figure 6.11b). The reactivity of the stacked crosses is further explored by acid treatment. The sample is exposed to 0.1 M acetic acid and the stacked crosses are completely destroyed. This leaves behind a net-like morphology where the crosses used to be (Figure 6.11c). This makes sense when compared to the distribution of lead in the darkfield image. The regions with lead do not dissolve with acid but the rest does. Combine this with the carbon seen by EELS it leads to the conclusion that the stacked crosses are a lead carbonate / lead titanate hydrid.

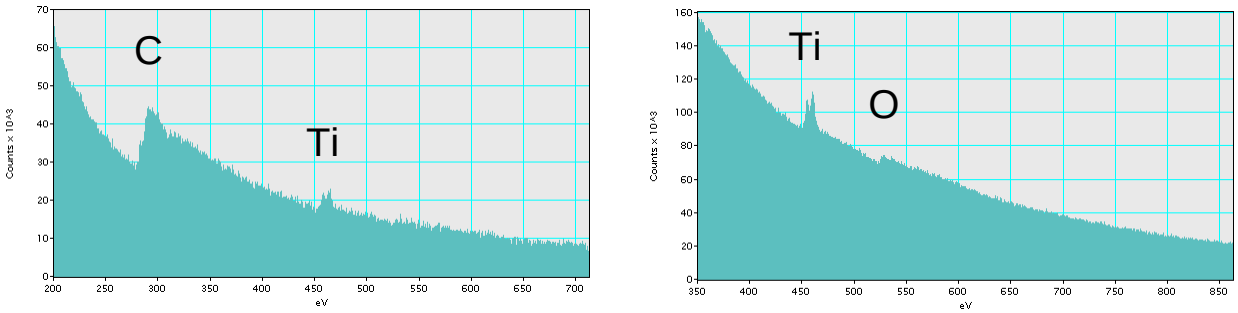

Figure 6.11: EELS of the stacked crosses structures shows C, Ti and O.

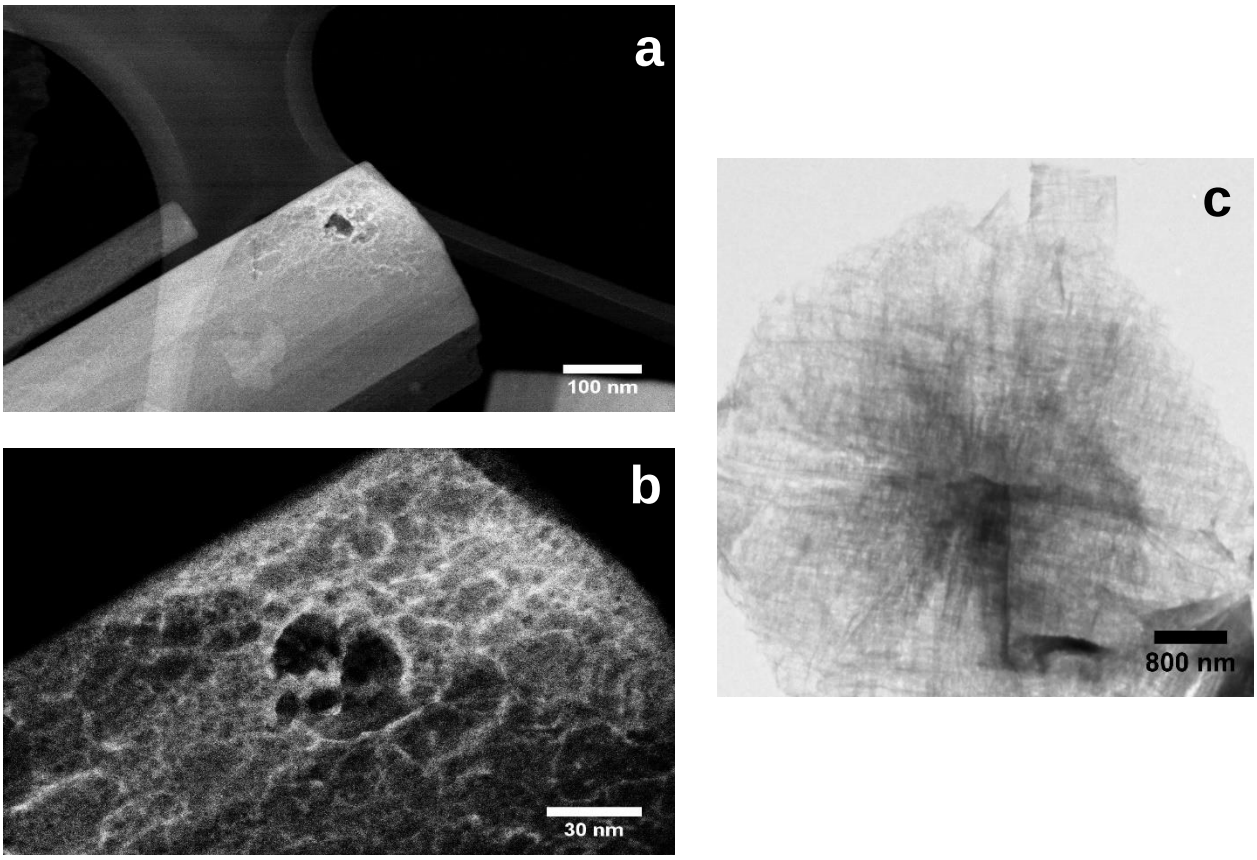

Figure 6.10: a) HRTEM of stacked crosses shows beam sensitivity when focuses on. b) Darkfield image of the stacked crosses shows an eratic distribution of lead. c) TEM of the stacked crosses after they are acid treated showing the net-like structure.

A temperature study was conducted to help elucidate the mechanism in the solvothermal system. At 60 °C the Pb-TiO gel is still present and there is irregular growth on the clusters (Figure 12 a). Raising the temperature to 105 °C produces hexagonal plumbonacrite and the Pb-TiO is still present. The hexagons produced this have the same offset layering seen in the stacked crosses, and a darker shared center point (Figure 6.12b). Raising the temperature further to 120 °C starts formation of the stack crosses. The cross are not separate entities but are merged with nearby Pb-TiO gel clusters (Figure 6.12c). Layered hexagons are also seen with larger lateral dimensions (> 4 μm).

An interesting product was produced when $Pb(NO_3)_2$ was used as the lead source instead of PbO. The solvothermal reaction produced single crystals needles millimeters in length. The needles are analyzed using single crystal XRD. The needles are $PbTiC_2H_3O_2$ with a unit cell a= 11.77 Å, b=8.32 Å and c=7.49 Å. The crystal is modeled showing a layered structure in the a direction and channels are present in the c direction (Figure 6.13). The needles have both Pb and Ti atoms present indicating a dissolution occuring during the solvothermal reaction. Currently there is no known lead-titanium structure with this formula.

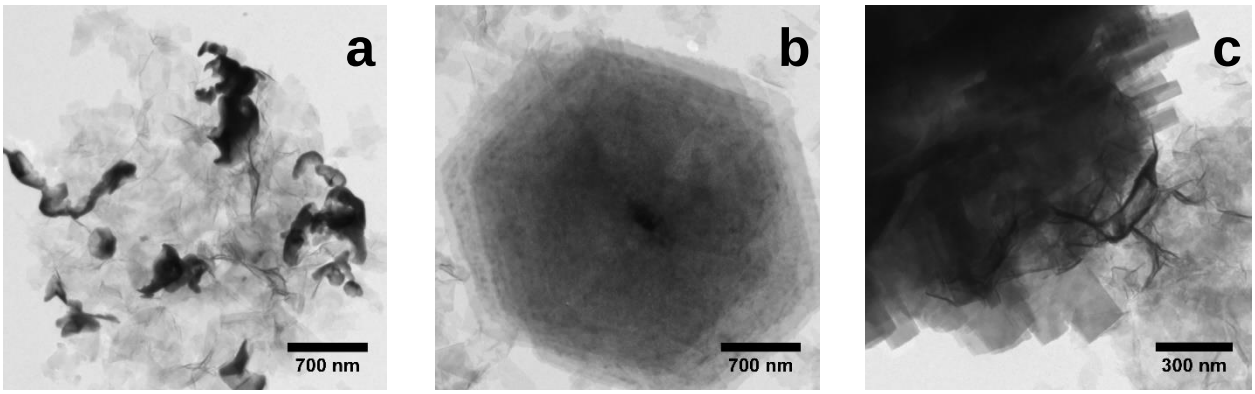

Figure 6.12: TEM of a) irregular growth on the surface of the Pb-TiO gel seen at 60 °C, b) Large stacked hexagons of plumbonacrite with Pb-TiO gel in the background at 105 °C, c) Formation of the stacked crosses at 120 °C.

PTO hydrothermal reactions that use bulk reagents function along a similar mechanism but typically produce micron sized cubes or large donut particles.[1-2] Using 2D nanoscale titania precursors with no mineralizers has an effect on the morphology of the products. However, when mineralizers are used the benefits of nanoscale precursors are lost and large particles growth is noted like other hydrothermal reactions.[4] When an organic base such as tetra methyl ammonium hydroxide (TMAOH) are used hydrothermally as the mineralizer, large micron sized cubes are obtained again.[5]

Based on the total observations of the solvothermal reactions we theorize a mechanism for how the system works. In the ethylene glycol the PbO reacts with CO_2 to form plumbonacrite 2D hexagons. The Pb-TiO gel plays an important role in the 2D morphology of the plumbonacrite. In a control reaction without Pb-TiO, the plumbonacrite formed was bulk crystals and not individual micron-sized hexagons. The mechanism for this controlled growth is not yet understood. After the hexagons form there is dissolution of Ti from the Pb-TiO and the Ti ions react with the hexagons. The morphology shifts from hexagons to crosses but the off-set layered structure is preserved. After 3 h at 180 °C the layered crosses are clearly formed but their structure is not well defined. They are somewhere between $PbTi_{0.8}O_{2.6}$ and $Pb_5O(CO_3)_3(OH)_2$ and the overall structure is not

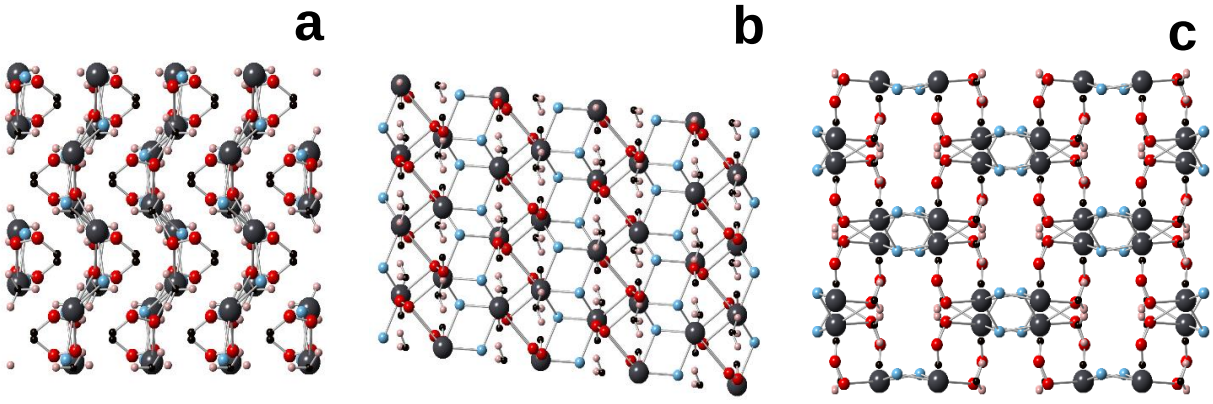

Figure 13: Modeled single crystal data showing the structure of the $PbTiC_2H_3O_2$ needles in the a, b, and c directions.

stable. With a concentrated electron beam or acid treatment the structure falls apart. Extended reaction times cause the stacked crosses to undergo another dissolution / nucleation into a more stable $PbTiO_3$ structure. This is seen in the 18 h reaction where the centers of the stacked crosses is clearly dissolved away.

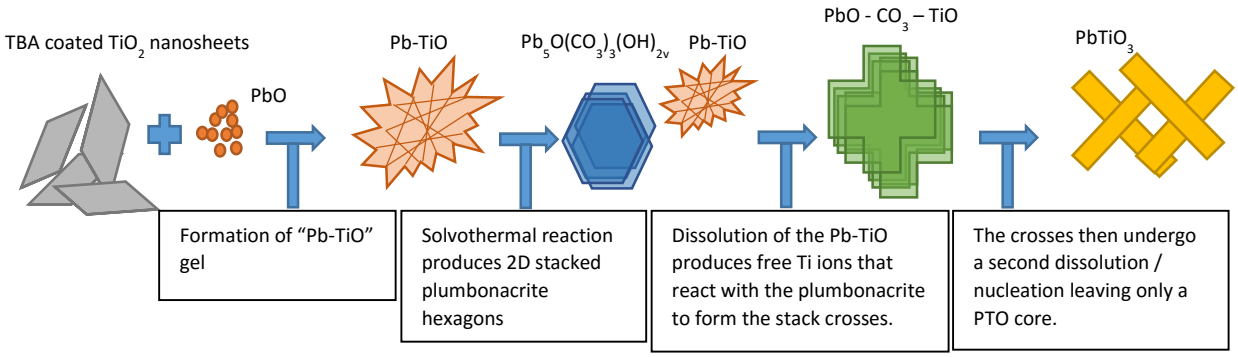

Figure 6.14: The proposed mechanism for the solvothermal reactions.

Conclusions:

$PbTiO_3$ nanoplatelets were synthesized using $(TBA)_{1.07}Ti_{1.73}O_4$ and $(TBA)_2Ti_4O_9$ nanosheets. The reactions were done hydrothermally and without the addition of any mineralizers. The product produced is much different from other hydrothermal syntheses found in literature. Instead of 3D cubes, our reaction produced 2D nanoplatelets. This indicates that the use of a 2D starting material has an effect on the product formed. The reaction proceeded through a known dissolution / nucleation pathway as shown by the formation of the intermediate $PbTi_{0.8}O_{2.6}$. The resulting nanoplatelets showed a relative intensity shift of peak in PXRD and had increased (001) and (002) peaks. These results are made possible by the increased reactivity of the Pb-TiO gel compared to anatase powders. Using mineralizers promotes the formation of 3D cubes.

The solvothermal reactions produced significantly different results than the hydrothermal reactions. A lead carbonate basic, plumbonacrite, intermediate is produced in situ and then reacted.

The plumbonacrite produced this way has large lateral dimensions and is a layered structure. This morphology is a result of the Pb-TiO gel because in control reactions plumbonacrite produced is thick with no clear layering. The plumbonacrite reacts with the Pb-TiO gel and forms a Pb-TiO-CO_3 stacked crosses intermediate that is not a stable structure. This is shown with the sample's beam sensitivity and EELS shows a strong C signal. Finally the crosses undergo dissolution / nucleation to $PbTiO_3$.

Experimental:

Preparation of "Pb-TiO" gels:

$(TBA)_{1.07}Ti_{1.73}O_4$ nanosheets and $(TBA)_2Ti_4O_9$ nanosheets were prepared by already established methods and outlined earlier in this disseration.[6] The suspensions of nanosheets are mixed with excess $Pb(NO_3)_2$, $Pb(OAc)_2$, or PbO and centrifuged at 10,000 RPM; then decanting the supernatant removes the TBA. The resulting gel-like "Pb-TiO" substance is used as the precursor is a series of hydrothermal and melt-flux reactions.

Hydrothermal reactions of "Pb-TiO":

The "Pb-TiO" gel is suspended in 20 mL of water. Various amounts of PbO, $Pb(NO_3)_2$, NaOH or KOH are added and the mixtures are sealed inside 45 mL acid digestion vessels. The reactions are heated to 100 - 200 °C for 1 - 16 h. The vessels are allowed cooled and the contents poured out and centrifuged at 10,000 RPM. The supernatant is discarded and the precipitate is suspended in 20 mL of H_2O again. At this point the products are sampled for TEM and PXRD analysis. The products are then acid washed using 100 µL -1 mL of glacial acetic acid and filtered through a 100 µm membrane filter.

Solvothermal reactions of "Pb-TiO":

The "Pb-TiO" gel is suspended in 20 mL of ethylene glycol. Various amounts of PbO, $Pb(NO_3)_2$, NaOH or KOH are added and the mixtures are sealed inside 45 mL acid digestion vessels. The reactions are heated to 100 °C, 120 °C or 180 °C for 1 h, 2 h or 3h. The vessels are allowed to cool and the contents poured out and centrifuged at 10,000 RPM. The supernatant is discarded and the precipitate is suspended in 20 mL H_2O. At this point the products are sampled for PXRD and TEM analysis. The products are then acid washed using 100µL - 1 mL of glacial acetic acid and filtered through a 100 µm membrane filter.

1. Cheng, H.; Ma, J.; Zhao, Z., Hydrothermal Synthesis of PbO-TiO_2 Solid Solution. *Chem. Mat.* **1994,** *6* (7), 1033-1040.

2. Liu, Y.-f.; Lu, Y.-n.; Dai, S.-h.; Shi, S.-z., Synthesis and growth mechanism of donut-like lead titanate particles by hydrothermal method. *Powder Technology* **2010,** *198* (1), 1-5.

3. (a) Moon, J.; Li, T.; Randall, C. A.; Adair, J. H., Low temperature synthesis of lead titanate by a hydrothermal method. *Journal of Materials Research* **1997,** *12* (01), 189-197; (b) Chien, A. T.; Sachleben, J.; Kim, J. H.; Speck, J. S.; Lange, F. F., Synthesis and characterization of $PbTiO_3$ powders and heteroepitaxial thin films by hydrothermal synthesis. *Journal of Materials Research* **1999,** *14* (08), 3303-3311.

4. Sandler, S. I., Models for thermodynamic and phase equilibria calculations. **1995**.

5. Cho, S.-B.; Noh, J.-S.; Lencka, M. M.; Riman, R. E., Low temperature hydrothermal synthesis and formation mechanisms of lead titanate ($PbTiO_3$) particles using tetramethylammonium hydroxide: thermodynamic modelling and experimental verification. *Journal of the European Ceramic Society* **2003,** *23* (13), 2323-2335.

6. (a) Tanaka, T.; Ebina, Y.; Takada, K.; Kurashima, K.; Sasaki, T., Oversized titania nanosheet crystallites derived from flux-grown layered titanate single crystals. *Chem. Mat.* **2003,** *15* (18), 3564-3568; (b) Allen, M. R.; Thibert, A.; Sabio, E. M.; Browning, N. D.; Larsen, D. S.; Osterloh, F. E., Evolution of Physical and Photocatalytic Properties in the Layered Titanates $A_2Ti_4O_9$(A = K, H) and in Nanosheets Derived by Chemical Exfoliation†. *Chem. Mat.* **2010,** *22* (3), 1220-1228.